Multimodal bioimaging of viral replication organelles and inclusion bodies

Emily Lacey



Reuben College

MSc(Res) Clinical Medicine

Nuffield Department of Clinical Medicine

Division of Structural Biology

University of Oxford

Hilary 2026

Word Count: 17,047*

*Excluding abstract and references

Classification: Confidential - Personal Data

Dedication

I would like to dedicate this work to **Dr Karen Davies** – a scientist of deep rigour and rare generosity, whose mentorship shaped a generation of structural biologists. She enabled the work behind this thesis – and hundreds like it – and her impact lives on in all of us who learned under her. Her mentorship nurtured my own journey in ways I will always carry with me. This is one of many echoes of her legacy.

I also wish to acknowledge every scientist who became a key worker during the COVID-19 pandemic. From lab techs to PIs, their tireless efforts kept research moving and communities safe. To all in support staff roles – the unsung hands that kept experiments running, reagents stocked, and labs safe – whose dedication carried science through its most urgent hour.

I am profoundly grateful to my supervisors: **Dr James Gilchrist**, **Dr Dalan Bailey**, **Dr Toby Tuthill**, **Professor Pippa Hawes**, **Dr Liz Fry**, **Dr Dan Clare**, and **Professor Sir Dave Stuart** – for their unwavering guidance, encouragement, and the opportunities they provided throughout this project. Their expertise and collaboration shaped not only the direction of this thesis but also my growth as a scientist. I would also like to thank **Dr Fatoumatta Jobe**, **Joanna Wells**, and **Dr Pranav Shah** for their invaluable support, training, and mentorship.

This work was made possible by the support of the University of Oxford's Doctoral Training Centre, the Electron Bio-Imaging Centre (eBIC) at Diamond Light Source, The Pirbright Institute, and the Department of Structural Biology (STRUBI) at the University of Oxford. This research project was fully funded by the UKRI-BBSRC iCASE Studentship.

Finally, to my family and my friends – thank you for your patience, cheer-leading, and belief in me.

Table of Contents

Glossary **4**

1. Abstract **6**

2. Introduction **8**

2.1 Global Significance of the Viruses **8**
2.1.1 Aphthoviruses 8
2.1.2 Pneumoviruses 9

2.2 Comparative Overview of Viral Replication Strategies **10**

2.3 Key Concepts in Viral Replication Organelles and Inclusion Bodies **13**
2.3.1 Formation and Structural Characteristics 13
2.3.2 Broader Comparative Insights 14

2.4 Overview of bRSV Replication **14**
2.4.1 Viral Entry and Uncoating 14
2.4.2 Transcription and mRNA Synthesis 15
2.4.3 Viral Translation and M2-1 15
2.4.4 Genome Replication 16
2.4.5 Nucleocapsid Assembly 16
2.4.6 Virion Assembly and Release 17

2.5 Overview of FMDV Replication **18**
2.5.1 Viral Entry and Uncoating 18
2.5.2 Translation of Viral Proteins 18
2.5.3 Formation of Replication Organelles 19
2.5.4 Negative- and Positive-Strand RNA Synthesis 19
2.5.5 Encapsidation 20
2.5.6 Virion Assembly and Maturation 21
2.5.7 Virion Release 22
2.5.8 Comparative Note on ERAV 22

2.6 Relevance of Phase Separation and Membraneless Organelles **24**
2.6.1 Mechanisms of LLPS in Viral Inclusion Bodies 24
2.6.2 Functional Role of LLPS in Viral Replication 24
2.6.3 Comparative Insights: LLPS in Other Viruses 25
2.6.4 Implications for Therapeutic Development 27

2.7 The Role of Advanced Bioimaging in Virology **28**
2.7.1 Advances in Cryo-ET 29
2.7.2 Integration of FIB-SEM in Multimodal Imaging 29

2.8 Research Questions and Objectives **31**

Key Research Questions **31**

3. Materials and Methods **33**

3.1 Sample Preparation for Bioimaging **35**
3.1.1 PRIMO Micropatterning 35
3.1.2 Cell Seeding on EM Grids 35
3.1.3 bRSV Infection and Transfection Protocols 36
3.1.4 ERAV Infection Protocols 36
3.1.5 Sample Vitrification: Vitrobot Plunge Freezing 37
3.1.6 Room Temperature TEM Imaging 37

3.2 Correlative Fluorescence Imaging **39**
3.2.1 Pre-Vitrification Imaging: Widefield and Live Confocal 39

3.2.2 Post-Vitrification Imaging 39
3.3 Cryo-TEM Screening of EM Grids 40
3.4 Correlative FIB-Milling Sample Lamellae 40
3.4.1 Sample Preparation and Workflow 40
3.4.2 FIB-Milling Applications in Virology 41
3.5 Cryo-Electron Tomography 41
3.6 Computational Processing 40
3.6.1 Motion Correction and CTF Estimation in Warp 40
3.6.2 Tomogram Reconstruction and Subtomogram Averaging 40
3.6.3 Quantification of Replication Organelles 41
4. Results 44
4.1 Technical Optimisation for Cryo-EM Imaging 44
4.1.1 Enhancing Sample Reproducibility through PRIMO Micropatterning 44
4.1.2 Optimisation of FIB-Milling for Lamella Preparation 47
4.1.3 Comparative Performance of Microscopy Techniques for Structural Analysis 51
4.2 Bovine RSV Inclusion Bodies 52
4.2.1 Low-Resolution Segmentation of bRSV IBs: A General Overview 52
4.2.2 Measurement of IB Dimensions Using CLEM 53
4.2.3 Comparative Imaging of GFP-bRSV-Infected and Co-Transfected pseudo-IB Cells, 24 hpi 57
4.2.4 Room-Temperature TEM and 3D Segmentation of RSV IB Morphology 63
4.2.5 TEM Imaging of a Bovine RSV Inclusion Body in Vero Cells 65
4.2.6 Cryo-ET Analysis of Potential LLPS-Driven IBs in bRSV-Infected Vero Cells 67
4.2.7 Cryo-ET Image and Segmentation Model of a Proposed IB in bRSV-Infected Cells 70
4.3 Equine Rhinitis A Virus Replication Organelles 72
4.3.1 Lipid Distribution and Nuclear Localisation in ERAV-Infected Vero Cells 72
4.3.2 Ferrous Ion BioTracker Staining in Mock and ERAV-Infected Cells 74
4.3.3 Visualisation and Segmentation of ERAV Replication Organelles 76
4.3.4 Distribution of SMV Volumes During ERAV Infection 79
4.3.5 Cryo-ET Imaging of ERAV Virions and Their Association with SMVs 81
4.3.6 Quantitative Analysis of SMV Properties During ERAV Infection 84
5. Discussion 86
5.1 Evaluation of Imaging-Based Approaches 86
5.1.1 Contrast Limitations in RSV Inclusion Body Imaging 86
5.1.2 Replication Organelle Classification and Quantification Challenges 87
5.1.3 Tethering Structures: Potential for Functional Significance? 89
5.1.4 Future Imaging Considerations 91
5.2 Biological Implications and Model Refinements 92
5.2.1 RSV IBs: Strengths and Limitations as Viral Replication Sites 92
5.2.2 ERAV ROs: Structural Stability and Metabolic Dependency 97
5.3 Future Directions and Open Questions 100
5.3.1 Investigating IBAG Formation and Function 100
5.3.2 Resolving the Role of Tethering Structures in ROs 101
5.3.3 Targeting Viral Replication Compartments as Therapeutic Strategies 102
6. Conclusion 104
7. References 106

Glossary

bRSV	Bovine Respiratory Syncytial Virus
CLEM	Correlative Light Electron Microscopy
Cryo-EM	Cryogenic Electron Microscopy
Cryo-ET	Cryogenic Electron Tomography
Cryo-SXT	Cryogenic Soft X-ray Tomography
CTF	Contrast Transfer Function
DMEM	Dulbecco's Modified Eagle Medium
DMV	Double-Membrane Vesicle
ER	Endoplasmic Reticulum
ERAV	Equine Rhinitis A Virus
FBS	Fetal Bovine Serum
FIB-SEM	Focused Ion Beam Scanning Electron Microscopy
FLIM	Fluorescence Lifetime Imaging Microscopy
FMDV	Foot-and-Mouth Disease Virus
GFP	Green Fluorescent Protein
GIS	Gas Injection System
hpi	Hours Post-Infection
IB	Inclusion Body
IBAG	Inclusion Body-Associated Granule
IDR	Intrinsically Disordered Regions
LLPS	Liquid-Liquid Phase Separation
MAVS	Mitochondrial Antiviral Signalling Protein
MDA5	Melanoma Differentiation-Associated protein 5
MOI	Multiplicity Of Infection
N	Nucleoprotein
NF-κB	Nuclear Factor Kappa B
P	Phosphoprotein
PBS	Phosphate-Buffered Saline

pIB	Pseudo Inclusion Body
PLL-g-PEG	Poly(L-Lysine)-graft-Poly(Ethylene Glycol)
RIG-I	Retinoic acid-Inducible Gene I
RO	Replication Organelle
SMV	Single-Membrane Vesicles
STA	Subtomogram Averaging
UV	Ultraviolet

1. Abstract

This thesis applies bioimaging techniques to compare the structural and functional adaptations of replication compartments in two RNA viruses: bovine respiratory syncytial virus (bRSV) and equine rhinitis A virus (ERAV). These serve as surrogate models for human respiratory syncytial virus (RSV) and foot-and-mouth disease virus (FMDV), allowing structural studies under reduced biosafety constraints. Cryo-electron tomography (cryo-ET), correlative light and electron microscopy (CLEM), and fluorescence microscopy are applied to resolve the architecture and function of bRSV inclusion bodies (IBs) and ERAV replication organelles (ROs).

bRSV IBs are highly dynamic, membraneless condensates formed via liquid-liquid phase separation (LLPS). IB-associated granules (IBAGs) colocalise viral RNA, ribosomes, and translation factors, suggesting a coordinated role in viral transcription and translation. In contrast, ERAV ROs, predominantly comprising single-membrane vesicles (SMVs), undergo a 2.6-fold size increase ($p < 0.001$) between 8 and 11 hpi, while maintaining a stable 3D volume ratio (0.72) - a shape-based metric comparing mesh-rendered to manually contoured volume - indicating preserved structural integrity during expansion.

bRSV IBs exhibit dynamic reorganisation but are environmentally unstable, whereas ERAV ROs provide structural stability and immune concealment, relying on host lipid metabolism. Experimental challenges in visualising both IBs and ROs, including segmentation limitations, low particle numbers, and imaging artefacts, are discussed,

alongside workflow optimisations that highlight potential antiviral strategies, such as destabilising LLPS to impair bRSV IBs or inhibiting vesicle biogenesis to disrupt ERAV replication.

By leveraging bRSV and ERAV as model systems, this study unpacks viral replication in biosafety-restricted pathogens, offering insights into immune evasion and the evolution of replication compartments, with potential applications in antiviral development and diagnostics.

2. Introduction

2.1 Global Significance of the Viruses

2.1.1 Aphthoviruses

Picornaviruses are non-enveloped, icosahedral viruses ~30 nm in diameter, with a positive-sense single-stranded RNA (ssRNA) genome (ICTV, 2021). They cause a range of human and animal diseases, including polio, hand-foot-and-mouth disease, hepatitis A, the common cold, equine rhinitis, and foot-and-mouth disease (FMD). Equine rhinitis A virus (ERAV) and FMDV, are both members of the *Aphthovirus* genus, are genetically related and share key replication strategies, making ERAV a valuable surrogate for studying FMDV under lower biosafety conditions.

ERAV, a widespread respiratory virus in horses, typically causes mild disease, with most animals recovering fully. As a BSL-2 pathogen, it poses a significantly lower biosecurity risk than FMDV, which is designated a SAPO Group 4 pathogen in the United Kingdom. This classification mandates BSL-3 or BSL-3+ containment due to the virus's high transmissibility, potential for large-scale outbreaks, and severe economic consequences (UKBRCN, 2025; WOAH, 2025).

FMDV is one of the most contagious viruses affecting cloven-hoofed livestock, spreading via direct contact, aerosols, and fomites (Ali *et al*., 2024). In non-endemic countries, vaccination is avoided due to trade restrictions and diagnostic challenges. Outbreaks cause severe economic losses, exemplified by the UK's 2001 outbreak, which resulted in over £8 billion in losses due to mass culling, trade restrictions, and

recovery efforts (World Organization for Animal Health, 2023). In low- and middle-income endemic countries, where livestock is essential for food and income, FMDV exacerbates financial instability and outbreak control measures, such as culling and trade bans disproportionately affect small-scale farmers. These countries rely on targeted vaccination campaigns; however, current vaccines are imperfect providing at best short-lived protection requiring frequent vaccinations, vaccine supplies are limited (Paton *et al*., 2009) and outbreaks frequent since local wildlife act as reservoirs for the virus.

ERAV serves as a practical surrogate for FMDV research, as both viruses share core replication mechanisms, but ERAV can be handled under BSL-2 conditions, facilitating high-throughput imaging studies.

2.1.2 Pneumoviruses

bRSV, a member of the *Pneumoviridae* family, is an enveloped, pleomorphic, negative-sense ssRNA virus (ICTV, 2021). It causes severe respiratory disease in calves, leading to economic losses due to reduced growth rates, secondary infections, and increased veterinary costs (Rincheval *et al*., 2017). Human RSV is a major global pathogen, responsible for 33 million acute respiratory infections annually, with 99% of deaths occurring in low-income countries (Nair, *et al*., 2010; Shi, *et al*., 2017). RSV hospitalisation rates are also rising in elderly populations (Falsey, *et al*., 2005; Shi, *et al*., 2020).

Control of bRSV remains a challenge due to the lack of a commercially available livestock vaccine. While vaccine development is ongoing, high costs and limited accessibility hinder implementation, particularly in resource-limited regions (World Health Organization, 2024; Jha *et al*., 2016). Additionally, RSV impairs long-term immunity, leading to frequent reinfections with the same strain (Jha *et al*., 2016).

2.2 Comparative Overview of Viral Replication Strategies

Both FMDV and RSV evade host immunity by forming replication compartments that shield viral RNA from detection. FMDV creates membrane-bound ROs, which protect viral RNA from immune sensors such as retinoic acid-inducible gene I (RIG-I) and melanoma differentiation-associated protein 5 (MDA5) (Monaghan, *et al*., 2004; Berryman, *et al*., 2012). Similar strategies are seen in coronaviruses and SARS-CoV-2 (Maier *et al*., 2016; Klein, *et al*., 2021). In contrast, RSV forms cytoplasmic IBs via liquid-liquid phase separation (LLPS), which spatially organise replication and modulate immune responses by sequestering host signalling molecules (Rincheval *et al*., 2017; Jobe *et al*., 2020).

RSV has a ~15.2 kb genome encoding 11 proteins, including nucleoprotein (N) and phosphoprotein (P), which drive IB formation through liquid-liquid phase separation (Galloux *et al*., 2020; Rincheval *et al*., 2017), enabling IBs to dynamically compartmentalise replication and transcription, potentially shielding these processes from host immune surveillance. Within IBs, IBAGs concentrate viral mRNA and translation pre-initiation complexes, suggesting a role in facilitating localised protein

synthesis (Rincheval *et al.*, 2017; Jobe *et al.*, 2020). Unlike membrane-bound compartments, IBs are highly adaptable, transitioning between liquid-like and gel-like states in response to cellular stress or antiviral pressures. This flexibility allows RSV to modulate replication conditions dynamically, supporting viral persistence in host tissues (Tollervey *et al.*, 2022). However, the absence of a membrane leaves IBs susceptible to host-induced disruptions, such as changes in osmotic pressure and immune signalling (Galloux *et al.*, 2020).

FMDV, with its smaller 8.5 kb genome, encodes a single polyprotein that is cleaved into functional units, including non-structural proteins involved in RO formation (Curry, *et al.*, 1997). Unlike RSV, FMDV relies on membrane-bound ROs, which are thought to derive primarily from extensive remodelling of host endoplasmic reticulum (ER) membranes, with potential contributions from the Golgi apparatus, based on similarities with other picornaviruses (Belov and van Kuppeveld, 2012; Lanke *et al.*, 2009). These vesicular compartments create a structured environment for RNA synthesis, polyprotein translation, and encapsidation, shielding viral intermediates from host immune detection (Monaghan *et al.*, 2004; Berryman *et al.*, 2016).

Although direct evidence for FMDV RO biogenesis remains limited, studies on enteroviruses and other positive-sense RNA viruses suggest that viral non-structural proteins play a central role in reshaping cellular membranes for replication (Belov, G.A. *et al.*, 2012). Enteroviruses and flaviviruses recruit host lipid-modifying enzymes, such as phosphatidylinositol-4-kinase (PI4K), to generate replication vesicles enriched in phosphatidylinositol-4-phosphate (PI4P); however, FMDV does not follow this strategy

(Berryman *et al*., 2016). Instead, picornaviruses like FMDV rely on non-structural proteins 2B, 2C, and 3A to induce membrane curvature, vesicle formation, and trafficking, ensuring the efficient compartmentalisation of replication (Lv *et al*., 2024; O'Donnell *et al*., 2011).

The contrasting replication strategies of RSV and FMDV reflect trade-offs between flexibility and stability. RSV's LLPS-driven IBs prioritise rapid adaptation, allowing the virus to modulate replication efficiency under varying cellular conditions. In contrast, FMDV's vesicular ROs provide a structurally stable environment optimised for high replication efficiency but require extensive host membrane remodelling to form (Roingeard *et al*., 2022). These differences align with their respective genome architectures and replication constraints.

As a positive-sense RNA virus, FMDV translates its genome directly, driving rapid polyprotein synthesis and cleavage (Pelletier and Sonenberg, 1988). In contrast, RSV, a negative-sense RNA virus, requires transcription into mRNA before translation can occur, requiring a highly organised replication environment within IBs (Rincheval *et al*., 2017).

Both replication compartments also share similarities with host stress granules and P-bodies, highlighting parallels between viral and cellular condensates. While RSV IBs resemble biomolecular condensates involved in RNA metabolism, FMDV ROs share features with vesicular replication structures observed in hepatitis C virus and coronaviruses (Klein *et al*., 2021). By studying these contrasting replication strategies,

this thesis provides insights into how viral replication compartments evolve to optimise efficiency, evade immunity, and adapt to host environments. This knowledge may inform future antiviral strategies targeting biomolecular condensates or membrane-associated replication factories.

2.3 Key Concepts in Viral Replication Organelles and Inclusion Bodies

Viral replication compartments are essential for optimising genome replication while evading host immune defences. These structures function as biochemical hubs, concentrating viral components, shielding replication intermediates from immune recognition, and facilitating efficient RNA synthesis.

2.3.1 Formation and Structural Characteristics

Positive-sense RNA viruses such as FMDV remodel host membranes to generate ROs, primarily derived from the ER with possible contributions from the Golgi (Belov, *et al.*, 2012; Berryman *et al.*, 2016). These structures typically include single- and double-membrane vesicles, shaped by viral non-structural proteins such as 2B, 2C, and 3A (O'Donnell *et al.*, 2011; Lv *et al.*, 2024).

By contrast, RSV, a negative-sense RNA virus, forms cytoplasmic IBs through LLPS, driven by interactions between N, P, and viral RNA (Galloux *et al.*, 2020; Rincheval *et al.*, 2017). These membraneless condensates dynamically concentrate replication machinery and exhibit IBAG subdomains that partition viral mRNA (Jobe *et al.*, 2020).

2.3.2 Broader Comparative Insights

Although their architectures differ, membrane-bound ROs versus phase-separated IBs, both systems are examples of how viruses create specialised compartments to support genome replication while reducing immune recognition. This dichotomy highlights two major paradigms of viral replication organisation: membrane remodelling in positive-sense RNA viruses and biomolecular condensation in negative-sense RNA viruses (Klein *et al.*, 2021; Dahmane *et al.*, 2022).

2.4 Overview of bRSV Replication

2.4.1 Viral Entry and Uncoating

bRSV infection begins with the attachment (G) and fusion (F) glycoproteins facilitating viral entry. G binds to heparan sulfate proteoglycans and nucleolin, concentrating virions at the cell surface and enhancing tropism for airway epithelial cells (Martínez and Melero, 2000; Rincheval *et al.*, 2017). F undergoes a conformational transition upon receptor engagement, merging the viral envelope with the host plasma membrane, bypassing endocytosis (Garcia *et al.*, 1993).

Following fusion, the viral ribonucleoprotein (RNP) complex is released into the cytoplasm, where it remains protected from degradation and immune recognition (Santangelo *et al.*, 2009). This complex, consisting of genomic RNA encapsidated by nucleoprotein (N), polymerase (L), and the cofactor phosphoprotein (P), remains structurally intact to support viral replication. P stabilises L, facilitating efficient

transcription initiation within cytoplasmic IBs (Collins *et al*., 2013; Rincheval *et al*., 2017).

2.4.2 Transcription and mRNA Synthesis

Transcription occurs within IBs, where the L polymerase, guided by P, initiates a sequential stop-start mechanism generating capped and polyadenylated mRNAs. Genes near the 3′ end are transcribed more abundantly, ensuring high levels of structural proteins essential for virion assembly (Collins *et al*., 2013).

M2-1 functions as a transcription anti-terminator, stabilising nascent mRNAs and preventing premature termination (Rincheval *et al*., 2017). IBAGs concentrate viral mRNA and replication components, potentially enhancing transcript stability and facilitating translation while contributing to immune evasion (Jobe *et al*., 2020).

2.4.3 Viral Translation and M2-1

bRSV mRNAs closely mimic host transcripts, allowing them to efficiently recruit translation initiation factors. Within IBAGs, these mRNAs co-localise with ribosomes and eIF4F, supporting localised and efficient translation (Rincheval *et al*., 2017; Jobe *et al*., 2024). M2-1 also facilitates mRNA stabilisation, ensuring full-length transcript production and efficient protein synthesis (Diot *et al*., 2023).

IB compartmentalisation protects viral transcripts from degradation while maintaining optimal local concentrations of mRNA and ribosomes (Zhang *et al*., 2024). This spatial organisation is particularly important for the synthesis of structural proteins such as N and matrix protein (M), which are directly involved in nucleocapsid assembly.

2.4.4 Genome Replication

Full-length positive-sense antigenomes serve as templates for negative-sense genomic RNA synthesis. L drives synthesis of new genomes, while P acts as a scaffold and N coats the RNA co-transcriptionally, preventing recognition by cytoplasmic RNA sensors (Rincheval *et al*., 2017).

Replication occurs within IBs, where the spatial separation of transcription and replication optimises efficiency. Unbound N (N^0) must be available for encapsidation, ensuring stability and shielding RNA from cytoplasmic immune sensors such as RIG-I and MDA5 (Collins *et al*., 2013). The newly synthesised genomic RNA integrates into mature RNPs, which are then transported to IB peripheries in preparation for packaging (Jobe *et al*., 2024).

2.4.5 Nucleocapsid Assembly

Nucleocapsid assembly occurs at IB peripheries, where viral RNA, N, and polymerase components converge. As N encapsidates the genome in a helical structure, P

maintains polymerase association, ensuring efficient replication and assembly (Rincheval *et al*., 2017).

The M protein links RNPs to viral glycoproteins embedded in the plasma membrane, guiding nucleocapsid transport to virion assembly sites (Collins *et al*., 2013). This interaction ensures structural fidelity and spatial coordination between replication and virion packaging.

2.4.6 Virion Assembly and Release

bRSV virions assemble at the plasma membrane, where M links RNPs to F and G glycoproteins, initiating budding (Rincheval *et al*., 2017). This process is facilitated by host endosomal sorting complexes, ensuring membrane scission and release.

bRSV also employs syncytial spread, promoting the fusion of infected cells with neighbouring cells to form multinucleated syncytia. This strategy enables viral dissemination while evading extracellular immune factors, supporting viral persistence within respiratory tissues (Garcia *et al*., 1993). While enhancing viral survival, syncytia contribute to airway obstruction and inflammation, exacerbating disease severity.

2.5 Overview of FMDV Replication

2.5.1 Viral Entry and Uncoating

FMDV initiates infection by binding to integrin receptors, primarily αvβ6, via the VP1 protein's RGD motif, facilitating viral entry into epithelial cells (Jackson *et al*., 2000). Alternative integrins, such as αvβ3, may expand the host range (Curry *et al*., 1995). Upon receptor engagement, FMDV undergoes clathrin-mediated endocytosis (O'Donnell *et al*., 2011).

Endosomal acidification then induces conformational changes in the viral capsid, resulting in the externalisation of the N terminus of VP1 and the small internal protein VP4. These hydrophobic elements insert into the endosomal membrane, forming pores that allow translocation of the viral RNA genome into the cytoplasm (Curry *et al*., 1997; Tuthill *et al*., 2006). This pH-triggered mechanism ensures efficient genome delivery while minimising exposure to innate immune sensors. Host chaperones may further stabilise the released RNA, protecting it from degradation (Tuthill *et al*., 2006).

2.5.2 Translation of Viral Proteins

FMDV employs a cap-independent translation mechanism via an internal ribosome entry site (IRES) in its 5′ UTR, recruiting host factors such as eIF4G and PTB for ribosome assembly (Martinez-Salas *et al*., 2008). Translation produces a single polyprotein, which is co- and post-translationally cleaved by viral proteases 2A and 3C

into functional structural and non-structural proteins (Carrillo *et al*., 2005; Belsham, 1990).

The viral 2A protease cleaves eIF4G, shutting down host translation and redirecting ribosomes to viral mRNA (Gradi *et al*., 1998). This hijacking of cellular translation machinery ensures high viral protein output within a short replication cycle.

2.5.3 Formation of Replication Organelles

FMDV induces membrane rearrangements to form ROs, primarily derived from the ER and Golgi, creating a vesicular network of SMVs and DMVs that concentrate replication components while shielding viral RNA from immune detection (Belov, *et al*., 2007; Berryman *et al*., 2016).

Non-structural proteins 2B, 2C, and 3A mediate vesicle formation. 2B disrupts membrane permeability, 2C promotes membrane curvature, and 3A interacts with host trafficking proteins to remodel Golgi-derived membranes (Belov *et al*., 2012; Sanz-Parra *et al*., 1999). Host factors such as GBF1 and ARF1 regulate vesicle trafficking, further supporting RO biogenesis (Lanke *et al*., 2009).

2.5.4 Negative- and Positive-Strand RNA Synthesis

FMDV replication begins with the synthesis of a complementary negative-sense RNA strand, which serves as a template for generating new positive-sense genomes. These

processes occur within ROs and are catalysed by the viral RNA-dependent RNA polymerase 3Dpol, with VPg acting as a primer (Paul *et al*., 2013).

Replication is tightly regulated, ensuring asymmetry in RNA synthesis, with positive-sense RNA produced in excess for both genome packaging and translation (Martinez-Salas *et al*., 2008). The spatial organisation of ROs minimises exposure of viral RNA intermediates to cytoplasmic immune sensors, such as RIG-I and MDA5 (Belov and van Kuppeveld, 2012).

2.5.5 Encapsidation

FMDV RNA packaging involves the assembly of structural proteins (VP0-VP3) into protomers, which then form pentamers that arrange into an icosahedral capsid with RNA facilitated maturation cleavage of VP0 to produce VP2 and VP4 (Tuthill *et al*., 2010). VP4 stabilises the interior of the capsid, while VP1-VP3 provide structural integrity (Tuthill *et al*., 2010; Logan *et al*., 1993).

Encapsidation is selective, mediated by RNA packaging signals that interact with capsid proteins to nucleate assembly. High-resolution structural work on other picornaviruses has shown that ordered RNA segments interact directly with conserved residues of VP1 and VP3, supporting a packaging signal-driven mechanism rather than a purely electrostatic process (Shakeel *et al*., 2016; Stockley *et al*., 2013). In this way, RNA structure guides capsid assembly with high specificity, ensuring production of infectious particles while maintaining immune evasion (Belsham, 2005).

2.5.6 Virion Assembly and Maturation

Provirion maturation occurs when VP0 is cleaved into VP2 and VP4, stabilising the capsid for infectivity (Curry *et al*., 1997). In enteroviruses, it has been established that this cleavage is tightly linked to genome encapsidation: the incorporation of RNA induces conformational rearrangements that position the VP0 scissile bond for hydrolysis, although RNA alone is not sufficient to drive cleavage (Kingston *et al*., 2024). Recent structural work has shown that conserved residues within VP0 (namely, Y078, R081, W107, E096) facilitate these conformational changes, with the process likely proceeding through an aspartic protease-like mechanism centred on VP2 H195 (Kingston *et al*., 2024).

However, in some picornaviruses such as aphthoviruses (including FMDV) and senecaviruses, VP0 cleavage can in some instances occur without RNA packaging, suggesting that their maturation pathway may differ somewhat from that of enteroviruses (Kingston *et al*., 2024).

Structural rearrangements following VP0 cleavage tighten inter-subunit interactions, enhancing capsid resilience to environmental stresses (Fry *et al*., 2005). The final maturation step thus yields a fully infectious virion, primed for host cell egress and transmission (Belsham, 2005).

2.5.7 Virion Release

FMDV predominantly exits host cells via lytic release, wherein cytopathic effects result in membrane rupture and the release of thousands of progeny virions (Tuthill *et al*., 2010). Viral proteins 2B and 3C contribute to membrane permeabilisation and cytoskeletal breakdown, accelerating host cell lysis (Carrillo *et al*., 2005; Belsham, 2005).

Evidence suggests that FMDV may also employ non-lytic release mechanisms, including vesicular exocytosis, potentially allowing immune evasion and persistence in specific cell types (Bird *et al*., 2014). These alternative pathways could facilitate viral dissemination without inducing immediate host cell destruction.

FMDV's accelerated replication, suppression of host translation, and potent cytopathic effects underpin its highly contagious, aggressive nature. The combination of vesicle-based immune evasion, rapid RNA synthesis, and high viral yields enables volatile outbreaks, driving large-scale livestock epidemics with severe economic consequences.

2.5.8 Comparative Note on ERAV

ERAV, the bovine rhinitis A and B viruses and FMDV constitute the genus Aphthovirus. ERAV shares many replication features with FMDV. Both viruses possess type II IRES (Internal Ribosome Entry Site) elements to drive cap-

independent translation, although ERAV preferentially initiates at the first AUG initiation codon whilst for FMDV the second AUG codon is more frequently selected (Hinton and Crabb, 2000). Capsid architectures are also similar, with acid-labile virions that undergo low pH-induced destabilisation (Tuthill *et al*., 2009).

It is likely that both ERAV and FMDV follow similar uncoating pathways triggered by acidic pH via transient intermediate capsid structure/s that protect the RNA prior to its translocation across the endosomal membrane, before the capsid falls apart into pentamers (Tuthill *et al*., 2009).

Replication organelles are a conserved feature across both viruses, with ERAV and FMDV inducing ER- and Golgi-derived vesicular networks that appear independent of PI4P lipid metabolism (Berryman *et al*., 2016; Groppelli *et al*., 2010). Despite these mechanistic similarities, their host range and disease outcomes diverge, FMDV drives systemic vesicular disease in cloven-hooved livestock whereas ERAV is a respiratory pathogen of horses, associated with febrile upper respiratory disease, viremia, and prolonged shedding through nasal secretions, urine, and faeces (Rossi *et al*., 2019; Stasiak *et al*., 2024).

2.6 Relevance of Phase Separation and Membraneless Organelles

2.6.1 Mechanisms of LLPS in Viral Inclusion Bodies

LLPS is primarily driven by weak multivalent interactions, including hydrogen bonds, van der Waals forces, and electrostatic interactions, which are individually weak but stabilise dynamic assemblies when combined (Patel *et al*., 2017; Molliex *et al*., 2015). This multivalency allows proteins and RNA to form phase-separated condensates, providing spatiotemporal regulation of cellular processes (Patel *et al*., 2017; Li *et al*., 2012).

In RSV, the N and P proteins contain intrinsically disordered regions that facilitate phase separation, assembling IBs that dynamically recruit viral and host factors necessary for replication (Galloux *et al*., 2020). These IBs exhibit a hierarchical organisation: dispersed cytoplasmic material, the main IB matrix, and internal substructures known as IB-associated granules (IBAGs) that further specialise in viral mRNA condensation and sorting. IBAGs demonstrate hallmark LLPS properties, including fusion, liquidity, and sensitivity to disruption by 1,6-hexanediol, a reagent known to interfere with weak hydrophobic interactions (Rincheval *et al*., 2017; Zhang *et al*., 2023).

2.6.2 Functional Role of LLPS in Viral Replication

LLPS provides multiple functional advantages in viral replication. By forming membraneless compartments, RSV IBs create a controlled microenvironment that

optimises transcription and genome replication while shielding viral components from immune detection. The ability of LLPS to selectively recruit essential factors while excluding host antiviral proteins further enhances replication efficiency (Zhang *et al*., 2024).

IBs maintain a liquid-like state during active replication, allowing for rapid molecular exchange of viral RNA, polymerase complexes, and nucleoprotein. However, under stress or antiviral conditions, IBs transition into a gel-like state, stabilising their structure and preserving essential replication machinery (Jobe *et al*., 2020; Nikolic *et al*., 2017). These transitions demonstrate how LLPS allows viruses to modulate replication dynamics in response to cellular conditions.

The functional role of IBs in viral replication has been studied using 1,6-hexanediol, which disrupts phase separation by interfering with weak molecular interactions. However, this reagent also affects general protein-protein interactions and membrane integrity, raising questions about its specificity (Zhang *et al*., 2023). Notably, the precise molecular interactions stabilising RSV IBs remain only partially understood, as P protein phosphorylation appears to be essential for IB function in vivo (Düster *et al*., 2021), suggesting additional regulatory layers beyond LLPS alone.

2.6.3 Comparative Insights: LLPS in Other Viruses

LLPS is a conserved mechanism observed across multiple viral families. SARS-CoV-2 nucleocapsid protein undergoes phase separation to regulate RNA packaging,

replication, and immune suppression, forming condensates like RSV IBs (Yang *et al*., 2020). However, unlike RSV, SARS-CoV-2 also relies on membrane-bound ROs, indicating that viruses often integrate both LLPS and vesicular compartmentalisation to enhance replication efficiency.

Mumps virus similarly forms phase-separated replication condensates, which transition between liquid-like and gel-like states to stabilise viral components and sequester immune-signalling molecules (Zhang *et al*., 2023). Additionally, LLPS has been implicated in DNA viruses, such as herpes simplex virus, where replication compartments concentrate polymerases and viral factors (Mazarakos *et al*., 2022).

Double-stranded RNA viruses provide another well-defined model. Rotaviruses form cytoplasmic replication factories, viroplasms, through LLPS of the scaffold protein NSP5 and RNA chaperone NSP2 (Geiger *et al*., 2021). Early viroplasms behave as liquid-like droplets that fuse, exchange components, and dissolve in aliphatic alcohols, while later in infection they undergo liquid-to-solid transitions associated with NSP5 hyperphosphorylation. These condensates selectively enrich viral transcripts and replication enzymes, coordinating the packaging of the eleven segmented dsRNA genome. In this way, rotavirus viroplasms provide a clear parallel to RSV inclusion bodies, but also a key contrast: while RSV IBs organise replication of a non-segmented negative-sense genome, rotaviruses exploit LLPS to coordinate the simultaneous replication and assortment of multiple RNA genome segments.

Together, these findings highlight the evolutionary conservation of LLPS as a strategy for viral replication and immune evasion across diverse viral families.

2.6.4 Implications for Therapeutic Development

Targeting LLPS represents a novel antiviral strategy. Since IBs function as replication hubs in RSV, disrupting their phase-separated organisation could impair viral RNA synthesis and protein production without directly targeting the viral genome, thereby reducing the likelihood of resistance mutations.

Small molecules that interfere with N-P interactions in RSV have been shown to destabilise IBs, leading to a loss of compartmentalisation and reduced replication efficiency (Zhang *et al.*, 2024).

The ability of LLPS to organise viral replication structures suggests that targeting phase separation could provide a new avenue for antiviral intervention. Inhibition of viral biomolecular condensates, such as those formed by RSV, SARS-CoV-2, mumps virus and rotavirus, may offer a promising therapeutic approach, potentially disrupting viral replication while minimising off-target effects on host cellular functions (Galloux *et al.*, 2020; Hoenen *et al.*, 2012).

2.7 The Role of Advanced Bioimaging in Virology

Modern bioimaging has revolutionised our understanding of virus-host dynamics, offering near-native, nanometre-scale views of replication structures like ROs and IBs that were once inaccessible. Techniques such as cryogenic electron tomography (cryo-ET) and cryo focused ion beam scanning electron microscopy (FIB-SEM) provide multiscale insights, ranging from atomic-level structural details to whole-cell organisation (Turoňová *et al*., 2020; Mendonça *et al*., 2021; Zhang *et al*., 2023). These technologies have been instrumental in clarifying virus-host interactions, organelle biogenesis, and the spatial dynamics of viral replication compartments (Lyu *et al*., 2024).

Recent work illustrates the power of this approach. Shah *et al*., (2023) used cryo-FIB milling and cryo-ET to capture the stepwise assembly of rotavirus particles *in situ*, resolving four discrete intermediates (SLP, DLP, eDLP, and TLP) by subtomogram averaging at near-atomic resolution. This study demonstrated not only how viral polymerase VP1 recruits genomes into assembling particles but also revealed previously unobserved conformations of the VP4 spike during budding through the ER. Such advances highlight how state-of-the-art imaging can access fleeting intermediates of viral replication and assembly that are inaccessible to traditional biochemical methods.

2.7.1 Advances in Cryo-ET

Cryo-ET is a powerful tool for capturing the architecture and dynamics of viral replication compartments. This technique enables three-dimensional imaging at nanometre resolution while preserving ultrastructure in a frozen-hydrated state. In unprocessed tomograms, cryo-ET typically achieves resolutions of ~3 nm, with sub-nanometre resolution attainable through sub-tomogram averaging, making it ideal for studying molecular assemblies, such as viral polymerase complexes or ribosome-enriched zones, within ROs and IBs.

Multimodal imaging workflows, such as correlative light electron microscopy (CLEM), further enhance cryo-ET's capabilities by integrating fluorescence microscopy with electron tomography. CLEM enables researchers to track the formation and maturation of viral replication compartments, linking molecular specificity to ultrastructural details. This approach has been employed to study the organisation of human RSV infection, by combining fluorescence imaging with cryogenic soft X-ray tomography (Spink *et al.*, 2018).

2.7.2 Integration of FIB-SEM in Multimodal Imaging

Focused ion beam scanning electron microscopy (FIB-SEM) is a critical preparative technique for cryo-ET, particularly for imaging viral replication structures within intact cells. Since whole cells are too thick for direct cryo-ET imaging, FIB-SEM is used to

generate thin vitrified sections (lamellae), exposing intracellular regions of interest while preserving native morphology.

A lamella is a ~100-200 nm thick section of a vitrified cell, precisely milled using an ion beam to enable high-resolution cryo-ET imaging of subcellular structures. This method allows researchers to visualise viral replication compartments in situ and analyse their molecular architecture. Computational techniques such as sub-tomogram averaging further refine cryo-ET data, enhancing structural resolution to sub-nanometre levels.

The integration of advanced volume-imaging tools with electron microscopy has dramatically deepened our view of viral replication. For example, Monaghan *et al*., (2004) used ultrastructural EM and fluorescence microscopy to show that FMDV infection induces early host membrane rearrangements in BHK-38 cells, where fragmented rough ER, Golgi, and smooth membrane-bound vesicles accumulate in a perinuclear region as viral RNA synthesis begins. Similarly, more recent studies using FIB-SEM and cryo-ET imaging of positive-sense RNA viruses (Quan *et al*., 2022) reveal how DMVs in enteroviruses serve as specialised platforms for genome replication while shielding viral RNA from immune detection.

Together, these bioimaging approaches provide a comprehensive framework for studying viral replication compartments at multiple spatial scales, bridging the gap between molecular interactions and cellular architecture. Their continued development will further advance our understanding of virus-host interactions, offering new avenues for antiviral strategies targeting replication organelles and biomolecular condensates.

2.8 Research Questions and Objectives

Understanding the formation and function of viral replication compartments is essential for clarifying how viruses optimise genome replication while evading host immune surveillance. Despite significant advances, key questions remain about the molecular mechanisms underlying the formation, dynamics, and functional specialisation of these compartments. This study aims to address key gaps in knowledge regarding the biogenesis of FMDV ROs and the functional organisation of IBAGs within RSV IBs.

Key Research Questions

1. What are the molecular determinants driving FMDV RO formation, and how do these organelles support viral genome replication?

- Hypothesis: FMDV ROs arise from extensive ER membrane remodelling, with viral proteins 2B, 2C, and 3A hijacking host lipid-modifying enzymes to establish vesicular compartments. These structures may function not only as sites of viral genome replication but also as shielded environments that sequester viral dsRNA intermediates, minimising innate immune recognition (Monaghan *et al.*, 2004; Dahmane *et al.*, 2022).
- Approach: By integrating cryo-ET and FIB-SEM, this study aims to map the structural dynamics of ROs, investigating whether membrane curvature and vesicle tethering facilitate polymerase recruitment and RNA synthesis.

2. What functional roles do IBAGs play in RSV replication, and do they serve as translation-competent microdomains?

- Hypothesis: IBAGs are spatially distinct substructures within RSV IBs, concentrating viral mRNA and translation machinery. While prior research suggests IBAGs are enriched in ribosomes (Rincheval *et al.*, 2017), it remains unclear whether active translation occurs within IBs or whether IBAGs primarily function as mRNA storage sites for subsequent cytoplasmic translation, or both.
- Approach: Using correlative bioimaging, CLEM and cryo-ET, this study aims to assess the presence of active ribosomes and translation initiation factors within IBAGs to determine their functional role in viral protein synthesis.

3. How do RSV and FMDV replication compartments compare in terms of their spatial organisation and immune evasion strategies?

- Hypothesis: RSV IBs and FMDV ROs represent distinct yet functionally convergent replication strategies. While IBs leverage LLPS-driven phase separation to concentrate viral factors in a membraneless state (Galloux *et al.*, 2020), FMDV ROs utilise membrane encapsulation to create a controlled microenvironment, minimising immune detection.
- Approach: This study aims to compare the subcellular distribution and macromolecular architecture of IBs and ROs to explore how each structure adapts to the constraints of its respective viral life cycle.

3. Materials and Methods

Cells and Viruses

Vero E6 cells (monkey kidney epithelial) were obtained from the Pirbright Institute Central Services Unit and cultured in Dulbecco's modified Eagle's medium (DMEM) supplemented with 10% heat-inactivated fetal calf serum (FCS; TCS Biologicals), sodium pyruvate (Gibco), and penicillin-streptomycin (Sigma).

Wild-type recombinant bRSV (rbRSV) and the deletion mutants rbRSV-ΔSH, ΔNS1, ΔNS2, and ΔNS1/2 were kindly generated by Dr Fatoumatta Jobe (The Pirbright Institute) using reverse genetics from the rbRSV strain A51908 variant Atue51908 (GenBank accession no. AF092942) (Schlender *et al*., 2000; Buchholz *et al*., 1999; Karger *et al*., 2001). The RSV non-structural proteins NS1 and NS2 function as interferon antagonists, suppressing host innate immune responses, deletion mutants lacking these genes provide tools to assess how viral replication and host-virus interactions are altered in the absence of these immune modulators. These viruses were propagated in Vero cells, while human RSV subtype A (A2 strain) was maintained in Hep-2 cells.

For ERAV viral infections, a virus growth medium was prepared using the same base components as the standard culture medium. This medium was supplemented with 1% fetal bovine serum (FBS) - vs 10% in standard medium - with an additional 25 mM HEPES (Gibco) included to maintain pH stability.

All virus stocks were purified at The Pirbright Institute by the Viral Glycoprotein and Picornavirus Groups, led by Dr Dalan Bailey and Dr Toby Tuthill, respectively. Purification was performed from total cell lysates using polyethylene glycol (MW 8,000) precipitation, followed by discontinuous sucrose gradient centrifugation to ensure high-purity viral preparations.

Plasmids and Transfections

All viral gene sequences used in this study were obtained from:

- Bovine RSV A51908 (GenBank accession no. NC_038272)
- Human RSV A2 (GenBank accession no. KT992094)

Expression plasmids were constructed, (pcDNA3.1), containing codon-optimized N genes, which were cloned at KpnI-BamHI sites (designated pN) and acquired from Bio Basic Inc. Full-length P genes were amplified by Dr Fatoumatta Jobe (The Pirbright Institute) through reverse transcriptase PCR (RT-PCR) using gene-specific primers and Superscript II reverse transcriptase (Invitrogen). The resulting amplicons were subsequently inserted into pcDNA3.1 at KpnI-BamHI sites, yielding the pP construct.

The p65 open reading frame was amplified from pcDNA3.1-HA-p65 (from Carlos Maluquer de Motes, University of Surrey) and subcloned into pcDNA3.1 at HindIII-BamHI sites, where it was designated as pP65.

All plasmid sequences were verified via conventional Sanger sequencing, and plasmid transfections were performed using TransIT-X2 (Geneflow).

3.1 Sample Preparation for Bioimaging

3.1.1 PRIMO Micropatterning

Gold Quantifoil grids (200-mesh, R 1.2/1.3 and R 1.2/2.5) were plasma-cleaned (Harrick Plasma) to enhance grid hydrophilicity for improved cell adhesion. Grids were coated with poly(L-lysine)-graft-poly(ethylene glycol) (PLL-g-PEG) to create a non-adhesive layer. UV photopatterning (PRIMO, Alvéole) was performed in the presence of a photoinitiator gel, using a UV laser to selectively degrade PLL-g-PEG, exposing defined adhesion sites. UV doses ranged from 40 to 800 mJ/mm², optimised based on experimental requirements.

3.1.2 Cell Seeding on EM Grids

Vero E6 cells were cultured in DMEM supplemented with 10% FBS, 2 mM L-glutamine, and 1% penicillin-streptomycin at 37 °C in 5% CO_2. Gold grids were preconditioned within 6-well plates in serum-containing media and rinsed with phosphate-buffered saline (PBS). Cells were trypsinised, resuspended in serum-free DMEM, and seeded at 2×10^5 cells/well. After 6-hours of incubation, 10% FBS was added to promote adherence before viral infection or transfection.

3.1.3 bRSV Infection and Transfection Protocols

Vero E6 cells were infected with recombinant bRSV-GFP (MOI 3) or transfected with N-GFP and P plasmids using Lipofectamine 3000 (Thermo Fisher). Following a 1-hour adsorption period at 37 °C, cells were washed with PBS and incubated in DMEM + 2% FBS for 24- or 48-hours before vitrification.

Transfection of N-GFP and P plasmids enabled the formation of pseudo-inclusion bodies (pIBs), allowing phase separation studies independent of viral replication.

3.1.4 ERAV Infection Protocols

Vero cells were infected with ERAV at MOI 120, a condition optimised based on infection time-course and plaque assay data from Lai (2023). This high MOI ensured abundant RO formation and minimised variability from uninfected cells, improving imaging consistency (Dahmane *et al*., 2022).

Cells were seeded onto micropatterned gold Quantifoil grids (200-mesh, R 1.2/1.3 and R 1.2/2.5) EM grids, incubated overnight for adherence, and infected in serum-free media at 37 °C for 1 hour. After PBS washes, DMEM + 2% FBS was added. Vitrification at 8 hpi captured early replication events, with later time points analysed separately to assess RO morphogenesis. This was informed by previous cryo-ET sample optimisation by Dr Audrey Lai (2023).

The high MOI also compensated for cryo-EM sample losses improving the likelihood of capturing ROs in cryo-ET datasets (Vijayakrishnan, 2023).

3.1.5 Sample Vitrification: Vitrobot Plunge Freezing

Grids were vitrified using a Vitrobot Mark IV (Thermo Fisher) under controlled conditions (95% humidity, 4 °C). Plunge-freezing parameters included: single-sided blotting, 10 s blot time, +10 blot force and no wait time. Single-sided blotting was achieved by physically removing one of the Vitrobot blotting arms, so that only one filter paper contacted the grid. This adaptation was necessary to avoid demembranating adherent cells during blotting, a common issue with double-sided blotting of cell-laden EM grids. Optimisations included adjustments to optimise ice thickness and control contamination. It is worth noting that Vitrobot instrument-to-instrument reproducibility can vary, so these parameters should be treated as an approximate guide rather than universally transferable settings.

3.1.6 Room Temperature TEM Imaging

Room temperature TEM imaging was performed by The Bioimaging Group at The Pirbright Institute to visualise the ultrastructural features of bRSV IBs in infected cells. bRSV-infected MDBK cells were fixed in 2.5% glutaraldehyde in 0.1 M sodium cacodylate buffer (pH 7.4) for 1 hour at room temperature, followed by post-fixation in 1% osmium tetroxide for 1 hour. Cells were dehydrated through a graded ethanol

series (50%, 70%, 90%, and 100%), embedded in Epon resin, and polymerised at 60 °C for 48 hours.

Ultrathin sections (~70 nm) were cut using a diamond knife on an ultramicrotome and collected on formvar-coated copper grids. Sections were stained with 2% uranyl acetate for 10-minutes and lead citrate for 5-minutes before imaging. TEM imaging was performed on a JEOL 2100F TEM operating at 200 kV using a TVIPS F416 camera for data acquisition.

MDBK cells were used in this Pirbright dataset as they represent a bovine-derived host system, capturing bRSV IB ultrastructure in a biologically relevant context. In contrast, subsequent experiments performed in this project employed Vero E6 cells to ensure continuity across workflows involving plunge-freezing and FIB-milling. Vero cells grow as flat monolayers, which improves lamella preparation and cryo-ET imaging by minimising ice thickness and cytoplasmic crowding. Thus, while MDBK cells provide host-relevant data, the use of Vero cells enabled methodological optimisation for downstream cryo-imaging.

Data collection for this method was conducted by Professor Pippa Hawes, Jennifer Simpson, and Joanna Wells at The Pirbright Institute. My role in this study involved the IMOD segmentation and analysis of the TEM dataset.

3.2 Correlative Fluorescence Imaging

3.2.1 Pre-Vitrification Imaging: Widefield and Live Confocal

Live-cell fluorescence imaging was performed on an inverted confocal microscope (Zeiss) and a widefield light microscope (Leica). Grids were imaged in Leibovitz's L-15 medium under controlled conditions. LasX software (Leica) was used for stitching fluorescence images captured with a 10x objective into a composite tile map. Z-stacking was applied to improve focus across varying grid heights.

3.2.2 Post-Vitrification Imaging

Cryo-fluorescence imaging was performed using a Leica cryo-THUNDER microscope. LasX software was used to generate fluorescence maps correlating with cryo-ET regions of interest. To minimise surface ice contamination, cryo-compatible covers were used and grid exposure to atmospheric moisture was kept to a minimum.

3.3 Cryo-TEM Screening of EM Grids

Clipped EM grids were screened on Thermo Scientific Glacios and Talos Arctica Cryo-TEMs (200 kV). Tomography 5 software automated low-magnification atlas generation, grid square detection, and suitability assessment. Criteria for selection included the absence of crystalline ice, optimal ice thickness, and uniform cell distribution. Suitable grids were FIB-milled and later transferred to the Titan Krios Cryo-TEM for high-resolution tomography acquisition.

3.4 Correlative FIB-Milling Sample Lamellae

3.4.1 Sample Preparation and Workflow

Grids were sputter-coated with platinum before loading onto the Scios DualBeam FIB-SEM (Thermo Fisher). A protective organo-platinum layer was deposited using a gas injection system (GIS) to reduce ion beam damage (Schaffer *et al*., 2015). Lamellae were milled in four sequential stages. Coarse removal was performed at 0.3 nA to trench either side of the region of interest. Intermediate thinning was carried out at 0.1 nA, followed by pre-final polishing at 50pA. Final polishing was performed at 30 pA to produce lamellae of 100-200 nm thickness.

3.4.2 FIB-Milling Applications in Virology

FIB milling was used to generate lamellae for cryo-ET analysis of viral replication compartments. Integration with CLEM workflows for vitrified bRSV samples enabled targeted milling of virus-associated regions.

3.5 Cryo-Electron Tomography

Tomograms were acquired on a Titan Krios Cryo-TEM (300 kV) equipped with a Falcon IV direct electron detector with Selectris energy filter. Zero-loss energy filtering (5 eV slit width) improved contrast. A dose-symmetric tilt scheme (±40° or ±50°, 2° increments) was used (Hagen *et al.*, 2017). Tomography 5 software automated batch tomography, and fiducial-free alignment was performed using patch-tracking algorithms. Table 1 summarises key microscopy modalities used in this study, detailing their resolution, sample preparation requirements, and specific relevance to the analysis of bRSV IBs and ERAV ROs.

Table 1: Comparison of Microscopy Techniques Used in the Study. *This table summarises the key microscopy techniques employed, highlighting their approximate resolution ranges, sample preparation requirements, strengths, limitations, and typical applications. The techniques compared include widefield light microscopy, confocal microscopy (live and fixed), freeze substitution, scanning electron microscopy (FIB-milling), cryo-CLEM, and cryo-ET. An additional column details the specific relevance of each technique to this thesis, particularly for studying RSV inclusion bodies and ERAV replication organelles (eBIC, Diamond Light Source; The Pirbright Institute; STRUBI, University of Oxford).*

Microscope	Resolution	Sample Prep	Strengths	Limitations	Applications	Relevance to Thesis
Light Microscope	200-250 nm (lateral), 500-700 nm (axial)	Minimal, live or fixed	Fast, easy to use, live imaging	Low resolution, limited contrast	Basic cell imaging, general morphology	Basic imaging for general morphology, useful for verifying sample integrity before advanced techniques
Confocal (Live)	200 nm (lateral), 400-500 nm (axial)	Fluorophores	Allows live-cell imaging with depth penetration, compatible with dynamic protein localisation studies	Limited resolution, photobleaching risk	Live-cell dynamics, protein localisation	Useful for live-cell imaging of RSV IBs, providing insights into dynamic protein interactions
Confocal (Fixed)	200 nm (lateral), 400-500 nm (axial)	Fixed, permeabilised, stained	Good for fixed fluorescently labelled samples	Limited resolution, photobleaching	Fixed-cell imaging, colocalisation studies	Used for fixed-cell imaging of viral replication sites, co-localisation of proteins in IBs
TEM (Chemical Fixation)	5 nm	Chemical fixation, dehydration, and resin embedding	Preserves ultrastructure relatively well	Fixation artifacts, time-intensive	Ultrastructure preservation, cellular architecture	Preserves ultrastructure of viral replication organelles, allowing better post-fixation imaging
SEM (FIB-Milling)	1-10 nm	Sample fixation, dehydration, and metal coating	High-resolution surface imaging and volume reconstruction	Limited depth penetration, destructive in conventional mode	3D imaging of cell surfaces and structures	Used for high-resolution imaging of virus-induced replication structures in cell membranes
Cryo-CLEM	20-50 nm (correlative limit)	Cryo-preserved, correlated with fluorescence	Correlates fluorescence with electron microscopy	Low throughput, requires fluorescence correlation	Correlative fluorescence and electron microscopy	Key technique for correlating fluorescence-marked viral replication sites with electron microscopy data
TEM (Tomography)	3-5 nm (sub-tomogram averaged)	High-pressure freezing, cryo-sectioning or plunge-freezing	High-resolution internal cellular structures	Requires complex sample preparation, sample sensitive to radiation degradation	Ultrastructure analysis, organelle organisation	Essential for high-resolution ultrastructure analysis of RSV inclusion bodies and FMDV replication organelles

3.6 Computational Processing

Computational cryo-ET refinement and training were carried out under the guidance of Dr Pranav Shah and the Department of Structural Biology, University of Oxford. This study employed an integrated processing pipeline using Warp, RELION, and M (Shah, Sanchez-Garcia and Stuart, 2025), providing a robust framework for handling cryo-ET datasets. This approach addressed key challenges in motion correction, tilt series alignment, tomogram reconstruction, and high-resolution refinement, critical for visualising the ultrastructural details of viral ROs and IBs (Tegunov and Cramer, 2019; Hagen *et al*., 2017).

3.6.1 Motion Correction and CTF Estimation in Warp

Motion correction and contrast transfer function estimation were performed in Warp. Tilt series were aligned using either AreTomo (marker-free) or, in some cases, by referencing intrinsic high-contrast cellular landmarks such as ribosomes, which served as internal markers during alignment. No exogenous fiducial beads were added to the samples in this study.

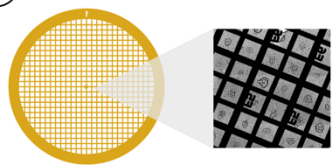
3.6.2 Tomogram Reconstruction and Subtomogram Averaging

Tomograms were reconstructed using weighted back-projection in Warp. Subtomogram averaging was performed in RELION-4 for 3D classification and refinement, with multi-particle optimisation in M improving resolution.

3.6.3 Quantification of Replication Organelles

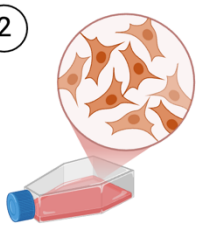
ROs were segmented in IMOD by manual contouring across tomographic slices. These contours were then converted into a triangulated 3D surface mesh using IMOD's mesh-generation function, which allowed extraction of enclosed volumetric data. A 3D Volume Ratio was defined as the ratio of the surface mesh-derived volume to the raw contour-based volume, providing a quantitative metric for assessing replication organelle shape and sphericity (with values closer to 1 indicating near-spherical symmetry). Figure 2 outlines the full experimental workflow, from micropatterning and sample vitrification through to tomographic reconstruction and data analysis.

1



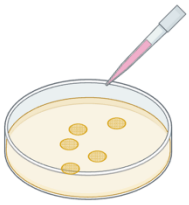
PRIMO micropatterning of EM grids

2



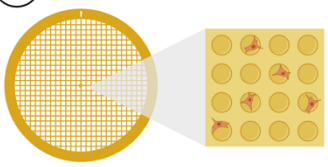
Passage vero cells

3



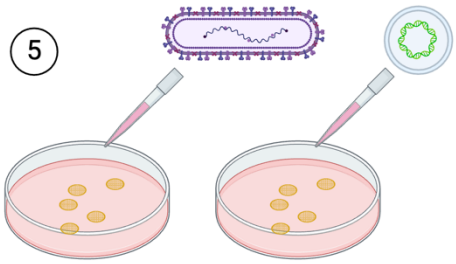
Grids transferred to a petri dish containing FBS with penstrep, where vero cells are added

4



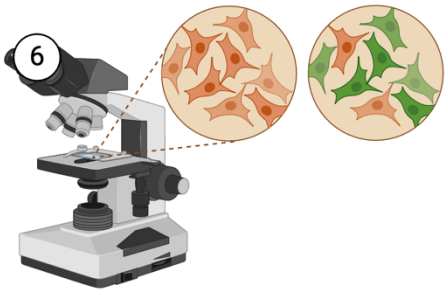
Incubation for vero cells to adhere to the EM grids

5



Infection and co-transfection, followed by incubation

6



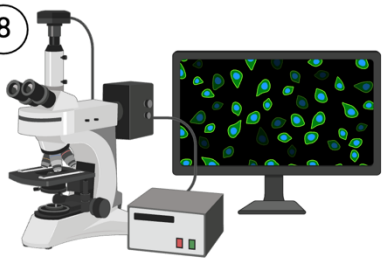
Inspecting infection and co-transfection

7



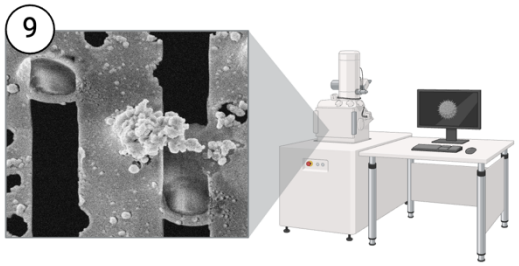
Vitrobot plunge freezing of samples

8



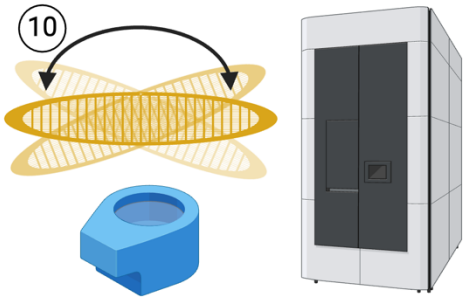
TEM screening grids, then cryo-CLEM mapping

9



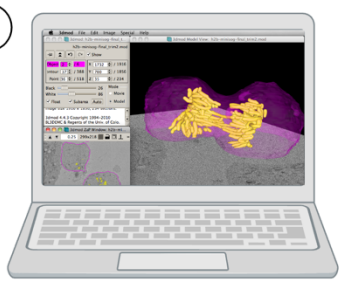
FIB-milling lamella

10



Cryo-ET of lamella

11



Processing tomograms

Made in bioRender

Figure 2: Experimental Workflow for Cryo-ET Analysis of RSV and ERAV Replication. *Schematic overview of the experimental workflow used for cryo-ET analysis of RSV and ERAV replication. The pipeline integrates micropatterning of EM grids, infection and co-transfection of Vero cells, vitrification, correlative cryo-light microscopy, cryo-FIB milling, and tomographic imaging/segmentation, enabling high-resolution structural studies of replication organelles. Created with BioRender.com.*

4. Results

4.1 Technical Optimisation for Cryo-EM Imaging

4.1.1 Enhancing Sample Reproducibility through PRIMO Micropatterning

To enhance cell adhesion and optimise cell sample distribution for cryo-ET, PRIMO micropatterning was used, enabling precise spatial control of Vero cells by using UV photopatterning of a non-adherent gel layer. This approach addresses a common challenge in cryo-EM workflows (Strale *et al.*, 2016), where inconsistent cell adherence on EM grids often leads to uneven distribution and cell clustering along grid bars, limiting accessibility for FIB-milling and subsequent imaging.

Micropatterned grids were compared to non-micropatterned grids using Cryo-THUNDER fluorescence imaging (Figure 3). On non-micropatterned grids, cells adhered inconsistently, often localising along the grid bars rather than the open central regions, leading to suboptimal sample distribution (Figure 3, panels A & B). In contrast, micropatterned grids significantly improved cell adherence to the central grid squares (Figure 3, panels C & D), creating a more even distribution of cells suitable for FIB-milling protocols.

Despite these advantages, high cell seeding densities on micropatterned grids often led to excessive clustering in the patterned regions, increasing sample thickness, which can hinder vitrification on a Vitrobot (Figure 3, panel D). These findings informed subsequent seeding optimisations, ensuring an optimal cell seeding density (2×10^5 cells/well) for cryo-EM preparation.

While micropatterning is a valuable preparation step for optimising cell adhesion and distribution on cryo-EM grids, it can also make the grids more vulnerable to handling damage. As a result, micropatterned grids are more susceptible to breakage, particularly during grid transfer and mounting, even before cells are seeded. In certain workflows, it may be safer to use non-micropatterned grids to minimise the risk of damage, especially when working with delicate grid types or high-throughput sample preparations where reproducibility and grid stability are critical. In summary, while micropatterning improves accessibility for FIB milling, it must be carefully balanced against grid fragility and seeding density to ensure reproducible vitrification.

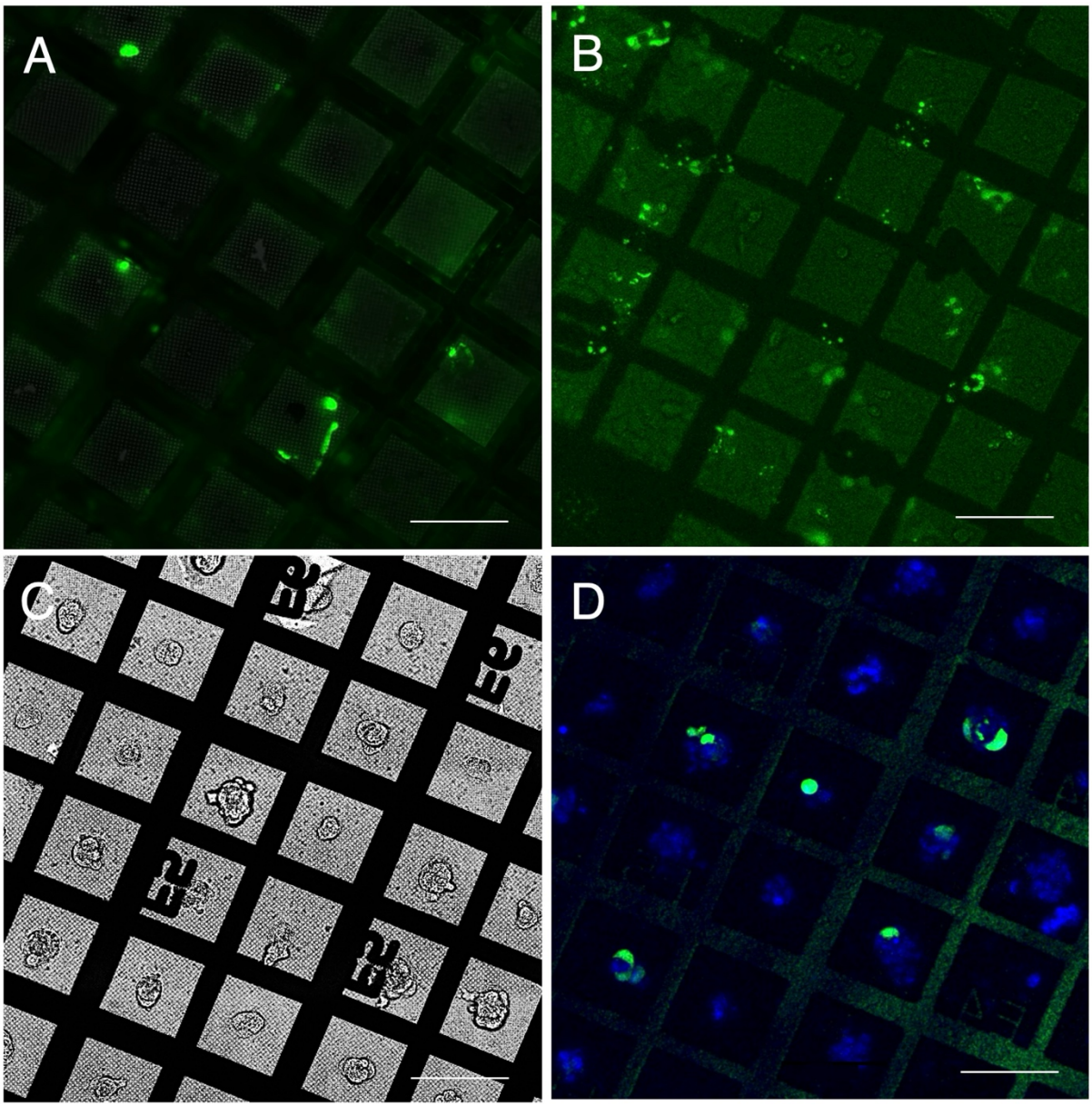


Figure 3: Cryo-THUNDER Imaging of Vero Cell Adherence on EM Grids. *[A, B] pIB-cotransfected Vero cells on non-micropatterned grids, with some cells adhering to grid bars rather than central regions. [C, D] Vero cells clustering preferentially in the centre of each grid square on micropatterned grids. [D] shows pIB-cotransfected cells with Hoechst nuclear stain (blue). While micropatterning improves central adherence, high seeding density can still produce excessive clustering, which may hinder plunge-freezing efficiency on a Vitrobot due to increased sample thickness. Scale bar: 100 µm.*

4.1.2 Optimisation of FIB-Milling for Lamella Preparation

Cryo-FIB milling is essential for generating electron-transparent lamellae suitable for tomography. The flat morphology of Vero cells on EM grids presents both advantages and challenges. Their thin profile increases the likelihood of freezing in a near-native state, reducing the risk of ice crystal formation, which is a common artefact in cryo-EM sample preparation (Schaffer *et al.*, 2015). However, their low height requires a shallow milling angle to produce suitable lamellae, requiring modifications to the standard FIB milling strategy. To accommodate this, a sequential milling workflow was optimised to minimise beam-induced damage while maintaining consistent thinning.

To generate high-quality lamellae, a four-step milling approach was used, progressively reducing the ion beam current to refine sample thickness while preserving ultrastructure. Coarse milling was conducted at 0.3 nA to remove bulk material and define the lamella shape (Figure 4, panels A and B). This was followed by intermediate milling at 0.1 nA, which further reduced the sample thickness (Figure 4, panel C). A pre-final thinning step at 50 pA was used to refine lamellae dimensions while minimising stress-induced bending. Finally, to achieve sufficient electron-transparency, the lamellae were thinned at 30 pA to a thickness of approximately 100-300 nm (Figure 4, panel D). While this iterative manual milling approach is time-intensive, it provides greater control over lamella quality compared to automated workflows. In particular, manual intervention allowed dynamic adjustment of milling angles for shallow Vero cell morphology, real-time correction of charging or curtaining artefacts, and targeted trimming of regions enriched for inclusion bodies or replication

organelles. Automated protocols are efficient for bulk lamella production but lack this flexibility, often carrying on through the process despite early signs of bending or drift. By contrast, manual optimisation reduced artefacts such as charging effects, bending, and ion beam-induced structural damage, making it preferable for preserving *in situ* viral replication structures.

To further enhance lamella stability and sample preservation during FIB milling, protective coatings were applied to the samples. A thin platinum layer (~10 nm) was first deposited by argon plasma sputtering. In this process, an argon plasma was generated and used to bombard a platinum target, dislodging platinum atoms that then condensed onto the sample surface. This conductive coating reduced charging effects, improved thermal conductivity, and stabilised the lamellae. In addition, a gas injection system (GIS) was used to deposit a protective layer of organometallic platinum directly onto the sample, which further prevented beam-induced deformations and reduced ion beam penetration depth, thereby preserving the native ultrastructure. Together, these protective measures improved sample integrity and increased the likelihood of producing high-quality lamellae suitable for downstream cryo-ET analysis.

This optimised milling workflow further supports the use of PRIMO micropatterning as a preparatory step in sample preparation. Achieving a controlled shallow milling angle is only reliably possible when single cells adhere at the centre of a grid square, a spatial arrangement that can be facilitated through micropatterning. This level of

precision ensures improved milling accessibility and consistency in thinning, reinforcing micropatterning as a valuable tool for lamella preparation.

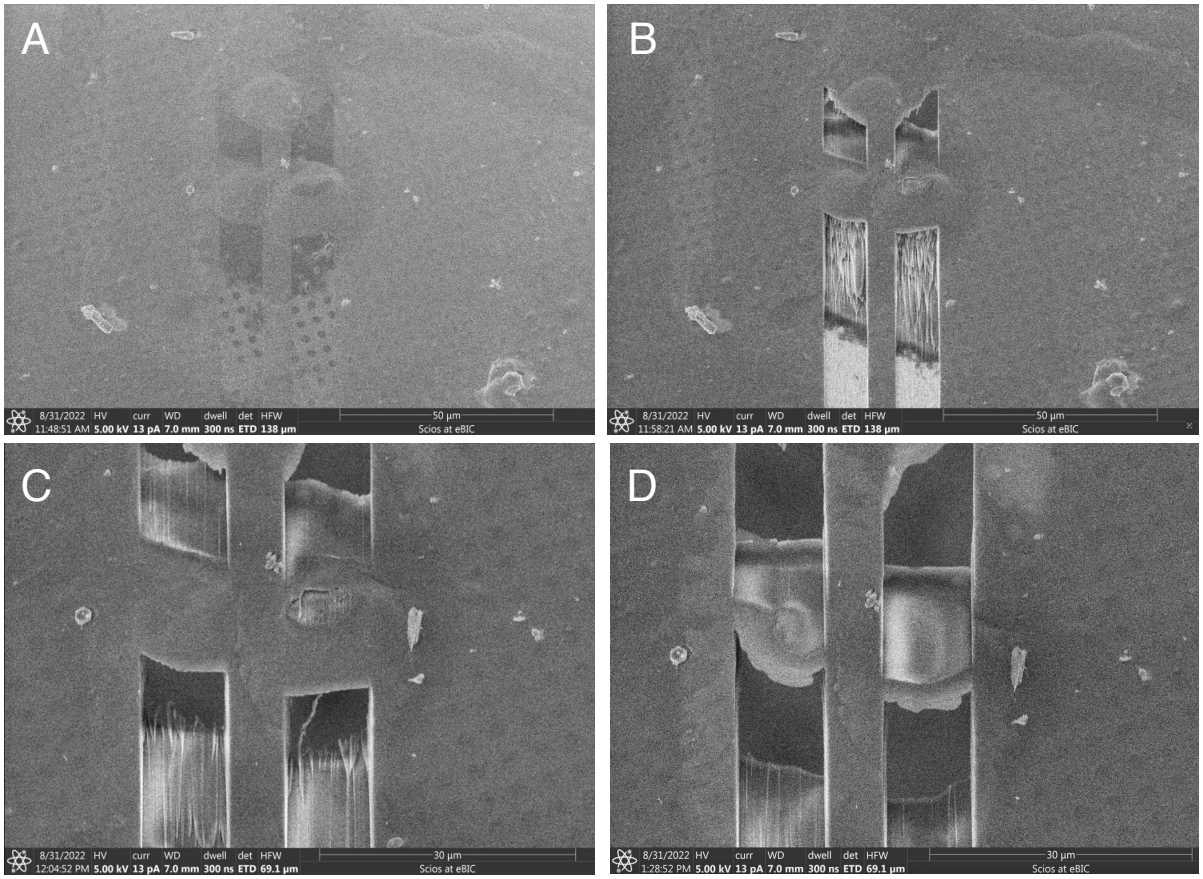


Figure 4: Sequential FIB Milling of Two Adjacent Vero Cell Lamellae. *Cryo-FIB milling of two adjacent Vero cells grown on EM grids, shown at four different time stages. Due to the relatively flat morphology of Vero cells, a shallow milling angle was required to optimise lamella formation while maintaining uniform thinning. [A] Initial site selection with protective overlayer deposition. [B] Continued coarse milling using high ion beam currents to remove bulk material. [C] Intermediate milling stage, refining the lamellae while minimising surface damage. [D] Final thinning using low ion beam currents to achieve a ~100-300 nm electron-transparent lamella, suitable for cryo-ET. Scale bars: 50 µm [A, B], 30 µm [C, D].*

4.1.3 Comparative Performance of Microscopy Techniques for Structural Analysis

Multiple imaging techniques were used to capture the structural and functional characteristics of viral replication, each with distinct advantages and limitations. Table 1 (Section 3.5) summarises key microscopy techniques used in this study, detailing their resolution, sample preparation requirements, and specific relevance to the analysis of bRSV IBs and ERAV ROs.

Light microscopy provided a rapid and accessible method for verifying sample integrity prior to cryo-preservation using plunge freezing. Low resolution imaging ensured that cell seeding and infection protocols were optimised before high-resolution imaging. Confocal microscopy (both live and fixed) was essential for monitoring IB dynamics in bRSV-infected cells, while freeze-substitution (Bioimaging Group, The Pirbright Institute) and FIB-SEM allowed high-resolution surface imaging of virus-induced membrane modifications.

Cryo-CLEM played a critical role in bridging fluorescence and electron microscopy datasets, enabling direct correlation and validation of IBs and ROs between the different imaging techniques (Arnold *et al*., 2016). Without this correlative insight, tomography insights can only be subjectively interpreted. Cryo-TEM tomography provided the highest level of ultrastructural detail, enabling the three-dimensional reconstruction of viral replication stages at chosen timepoints of infection.

4.2 Bovine RSV Inclusion Bodies

4.2.1 Low-Resolution Segmentation of bRSV IBs: A General Overview

Primarily, low-resolution images of bRSV inclusion bodies were captured, where Imaris segmentation (Oxford Instruments) was applied to a fixed confocal imaging dataset (Figure 5). This captured z-stacks through wild-type GFP-tagged bRSV-infected Vero cells. Imaris segmentation in this case used a standard intensity-based thresholding algorithm within the “Surface” module, rather than a machine-learning or AI-trained classifier. The segmentation was therefore semi-automated: IB boundaries were identified by software, but parameters (intensity threshold, smoothing, and size filters) were manually defined and iteratively adjusted to optimise inclusion body recognition.

This dataset provided an early assessment of infection efficiency, allowing validation of the infection protocol prior to proceeding with high-resolution cryo-ET experimentation. The segmentation enabled 3D reconstruction of IB morphology, allowing recognition of IB dimensions, volume distribution, and spatial relationships within the infected-host cytoplasm. The resulting segmentations confirmed that IBs exhibit a dynamic size range, suggesting continuous maturation and remodelling throughout the infection cycle.

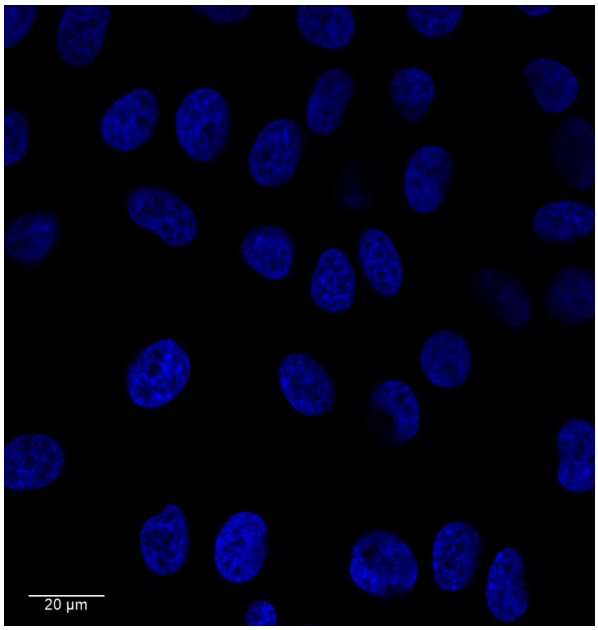
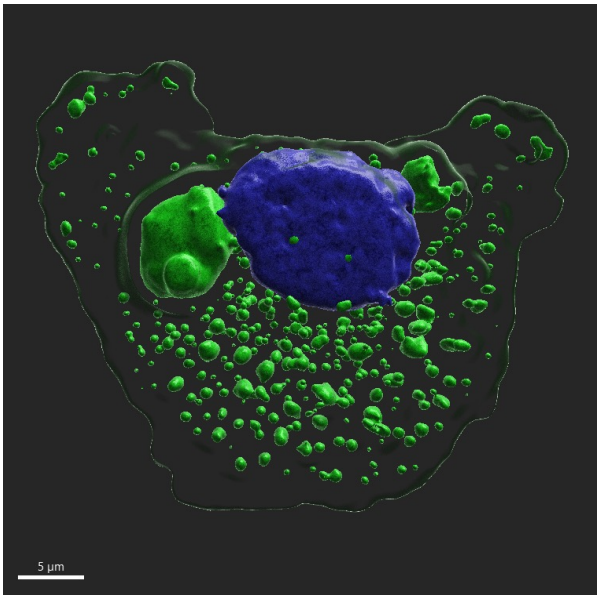
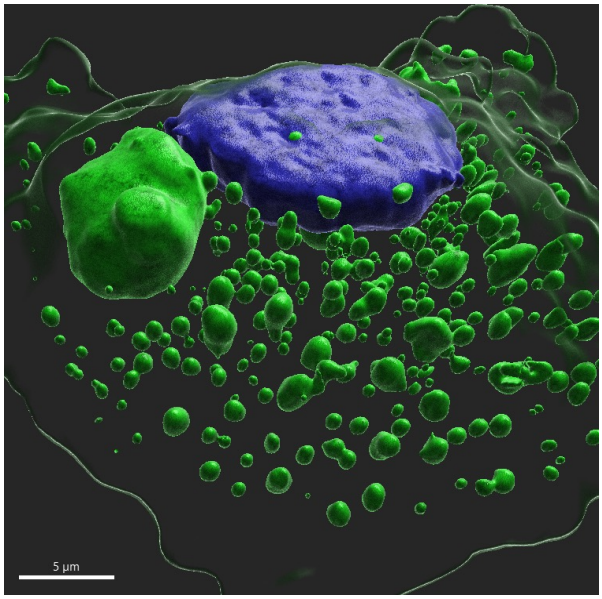


Figure 5: 3D Reconstruction of GFP-bRSV Infected Vero Cell. *3D-rendered confocal microscopy images of a fixed GFP-bRSV-infected (green) Vero cell, reconstructed from a z-stack and segmented using Imaris. The nucleus (blue, DAPI stain) is centrally located, with viral inclusions accumulating around it. The reconstruction highlights the spatial organisation of viral structures within the infected cell. Scale bars: 5 µm for WT infections (MOI 3); 20 µm for mock veros.*





4.2.2 Measurement of IB Dimensions Using CLEM

To quantify IB size and function, CLEM was used, allowing for direct comparison between fluorescence-based IB imaging and ultrastructural electron microscopy data. This approach ensured accurate measurements while enabling cross-validation between imaging techniques. IB diameters were quantified using Imaris and LAS X, supporting a robust analysis of IB morphologies.

This study builds upon my contributions to Jobe *et al*., (2024), where I measured IB dimensions using the same workflow to validate size distribution across imaging techniques (Figure 6). Statistical analysis of IB diameters in bRSV-infected Vero and MDBK cells revealed a broad size range (~2 μm to ~10 μm), reinforcing a model in which IBs dynamically grow, coalesce, and evolve throughout infection. This dynamic nature is consistent with their function as phase-separated viral replication compartments.

Further analysis sought to determine whether N^0P, a transient nucleocapsid-phosphoprotein complex, forms a concentration gradient around IBs (Galloux *et al*., 2020). In these experiments, N^0P was visualised indirectly via fluorescently tagged phosphoprotein (P), which acts as the obligate chaperone for N and reports the localisation of the N^0P complex. In fluorescence microscopy, this signal appears as a peripheral ring, yet is lost upon entering the IB, likely due to a conformational change that occurs as N^0P transitions into the phase-separated IB environment. This observation suggests that N^0P acts as a pre-entry staging point, accumulating at the IB periphery before being incorporated into the replication complex.

The localisation of N^0P at the IB boundary is functionally significant, as N alone has a high affinity for RNA and would otherwise bind non-specifically to cellular RNA if unregulated. The interaction with P prevents premature RNA binding, ensuring that N^0P remains in a chaperoned state until it reaches the IB. Once inside, N^0P dissociates, releasing N to encapsidate newly synthesised viral RNA, a critical step for RSV

genome replication. The presence of a potential N^{0}P gradient further supports the idea that IBs regulate nucleocapsid availability, ensuring a controlled supply of N for encapsidation at replication sites.

These findings highlight the importance of multimodal imaging approaches in defining IB structure and function. The observed differences between fluorescence and electron microscopy measurements reflect the complexity of RSV IB organisation, reinforcing the need for high-resolution, correlative analyses to fully resolve the molecular dynamics within these phase-separated compartments.

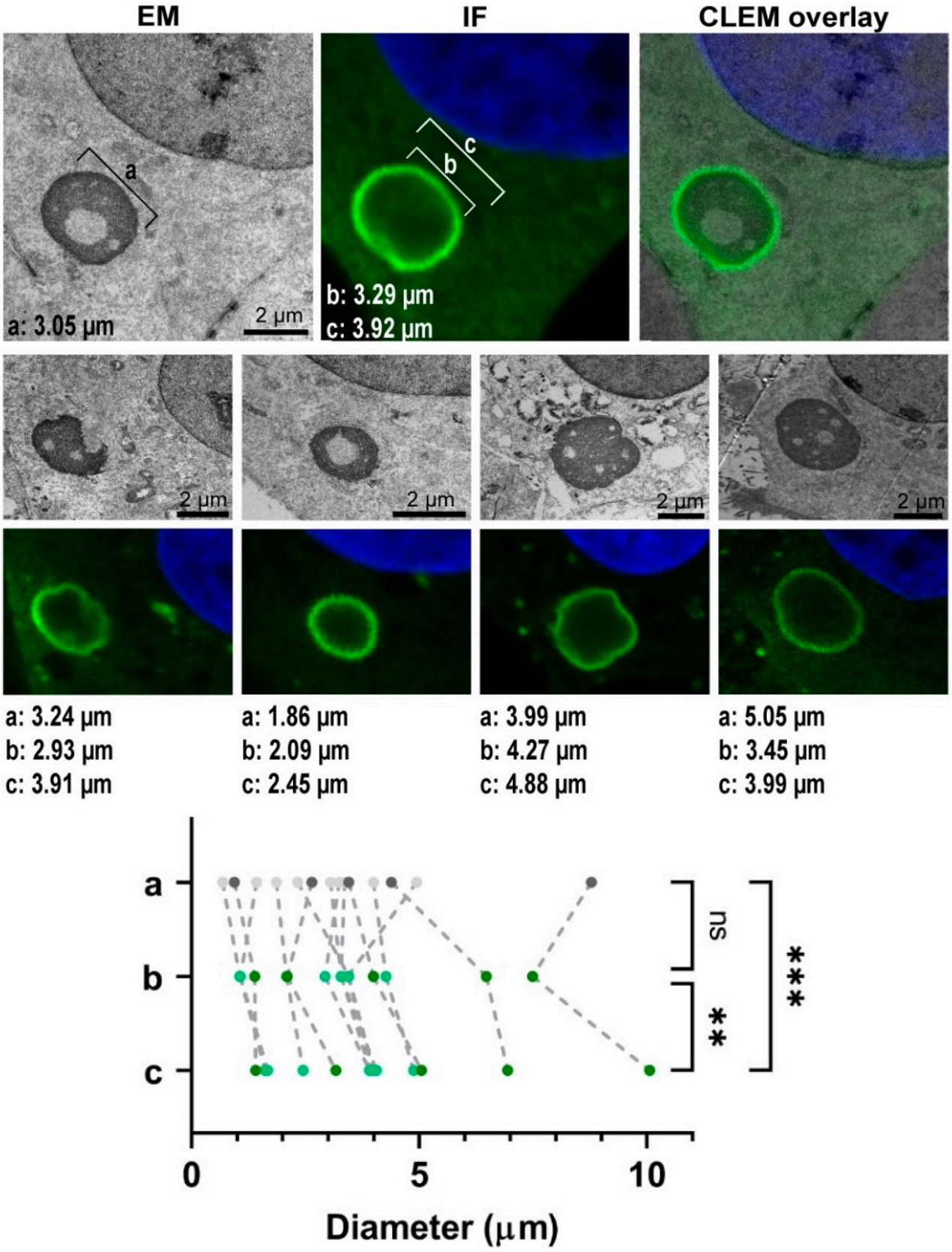

EM
IF
CLEM overlay
a
b
c
a: 3.05 µm
2 µm
b: 3.29 µm
c: 3.92 µm
2 µm
2 µm
2 µm
2 µm
a: 3.24 µm
b: 2.93 µm
c: 3.91 µm
a: 1.86 µm
b: 2.09 µm
c: 2.45 µm
a: 3.99 µm
b: 4.27 µm
c: 4.88 µm
a: 5.05 µm
b: 3.45 µm
c: 3.99 µm
a
b
c
ns
**
****
0
5
10
Diameter (µm)

Figure 6: Correlative Light and Electron Microscopy Analysis of Inclusion Body Dimensions in bRSV-Infected Cells. *CLEM imaging and quantitative analysis in Imaris and LAS X were used to measure the longest diameter of RSV IBs in EM micrographs (a) and compare them to the internal (b) and external (c) diameters of the same IBs imaged by confocal fluorescence microscopy. Representative IB measurements are shown above, with all quantified data presented below. Grey dots represent EM measurements, while green dots represent confocal measurements; variations in shading (light vs dark) reflect overlapping datapoints rather than separate conditions. Statistical analysis was performed using one-way ANOVA with Tukey's multiple comparisons; *P < 0.001, P < 0.01, ns = non-significant (Jobe et al., 2024).*

4.2.3 Comparative Imaging of GFP-bRSV-Infected and Co-Transfected pseudo-IB Cells, 24 hpi

To distinguish between native bRSV IBs and artificially induced pseudo-IBs, comparative imaging was first conducted using GFP-bRSV-infected Vero cells (MOI 3) alongside pseudo-IBs generated by N and P plasmid co-transfection. Imaging across multiple modalities (fixed confocal, widefield, and Leica cryo-light microscopy) revealed clear differences between infection-driven IBs and pseudo-IBs (Figure 7; Jobe *et al.*, 2020). Infected cells displayed IBs that clustered near the perinuclear region, while pseudo-IBs appeared more dispersed, reflecting the artificial induction of condensates by N and P expression.

To directly assess how the stoichiometry of N and P expression influenced pseudo-IB morphology, cells were transfected with N:P plasmid ratios of either 1:1 or 3:1. Fixed confocal microscopy confirmed that higher N:P ratios (3:1) yielded larger and more compact pseudo-IB condensates, which more closely resembled wild-type IBs

observed in infected cells (Figure 8; Galloux *et al.*, 2020). In contrast, pseudo-IBs formed at a 1:1 ratio were smaller and more heterogeneous, supporting the idea that protein dosage governs condensate morphology.

Importantly, each sample type offers distinct advantages within the cryo-ET pipeline: GFP-bRSV-infected cells provide biologically relevant IBs that capture native ultrastructures involved in viral replication, while pseudo-IBs serve as controlled models, isolating the effects of specific viral proteins on IB formation and facilitating targeted biochemical analyses. Additionally, cryo-light microscopy confirmed that both authentic and pseudo-IBs remained structurally intact post-vitrification, validating their suitability for downstream cryo-EM. Together, these complementary models and imaging approaches strengthen the robustness of the system for investigating RSV IB ultrastructure.

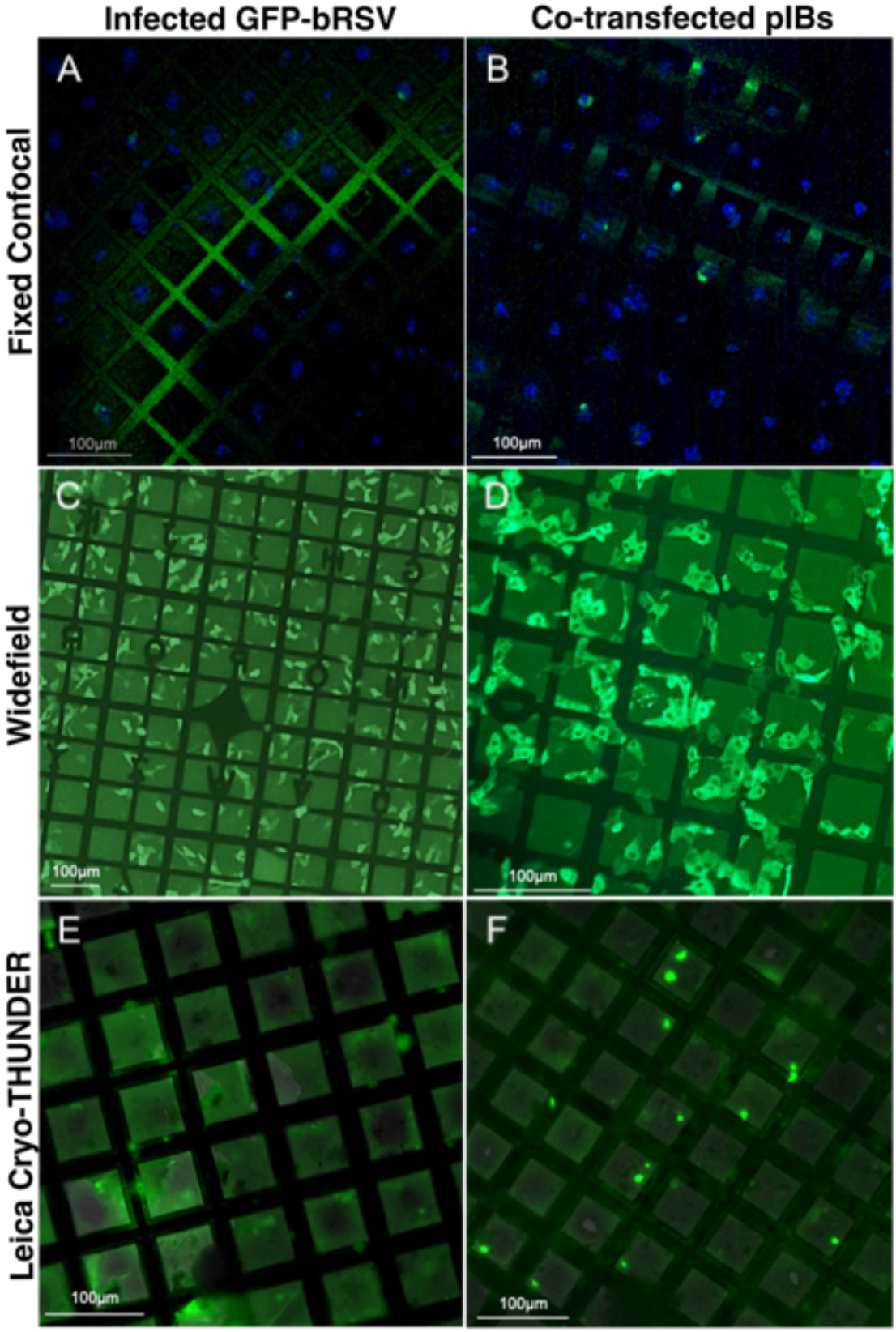

Infected GFP-bRSV
Co-transfected pIBs
Fixed Confocal
Widefield
Leica Cryo-THUNDER
A
B
C
D
E
F
100µm
100µm
100µm
100µm
100µm
100µm

Figure 7: Comparative Imaging of GFP-bRSV-Infected (MOI 3) and Co-Transfected pseudo-IB Cells, 24 hpi. *Representative images of GFP-bRSV-infected Vero cells (left column: panels A, C, E) and N+P co-transfected pseudo-IB cells (right column: panels B, D, F). Images were acquired using three imaging modalities:*

- *Panels A and B: fixed confocal microscopy (green = GFP, blue = DAPI-stained nuclei).*
- *Panels C and D: widefield microscopy, providing grid-wide overviews of GFP-positive cells.*
- *Panels E and F: Leica Cryo-THUNDER, confirming preservation of GFP fluorescence in vitrified samples.*

These comparisons highlight the differences in resolution and fluorescence retention across imaging approaches. Scale bars: 100 µm. Blue staining in fixed confocal images corresponds to nuclei (DAPI dye). Scale bars: 100 µm.

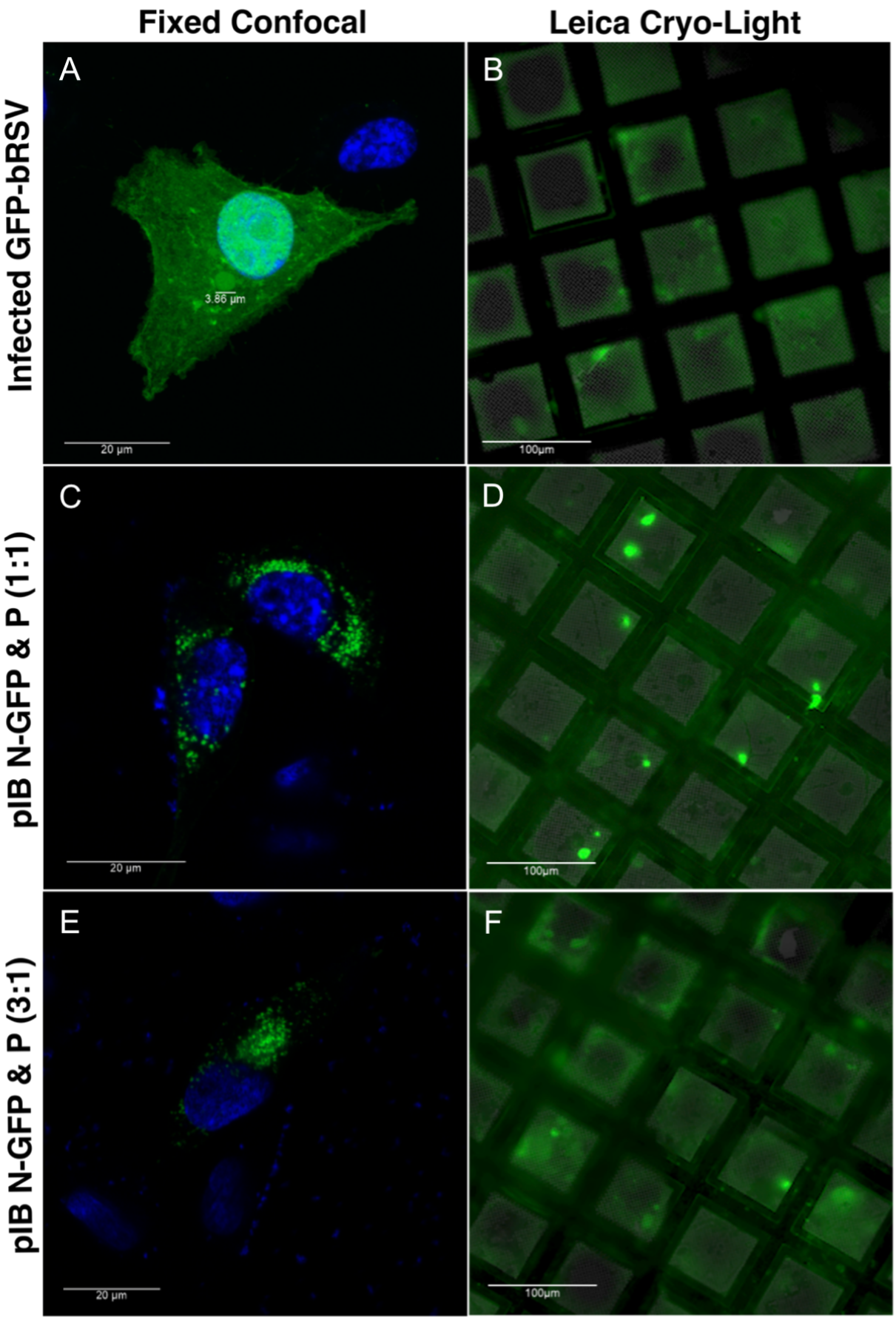

Fixed Confocal
Leica Cryo-Light
Infected GFP-bRSV
pIB N-GFP & P (1:1)
pIB N-GFP & P (3:1)
A
B
C
D
E
F
3.86 µm
20 µm
100µm
20 µm
100µm
20 µm
100µm

Figure 8: Low-resolution characterisation of WT IBs (MOI 3) and pseudo-IBs using fixed confocal microscopy and Leica cryo-light imaging, 24 hpi. *Representative images of authentic bRSV IBs (GFP-bRSV-infected Vero cells, MOI 3; panels A, B), and pseudo-IBs generated by N+P plasmid co-transfection at either 1:1 (panels C, D) or 3:1 ratios (panels E, F).*

- *Panels A, C, E (left column): Fixed confocal microscopy. Green = GFP-tagged IBs or pseudo-IBs, blue = DAPI-stained nuclei.*
- *Panels B, D, F (right column): Leica cryo-light microscopy of vitrified grids, showing GFP fluorescence preserved post-vitrification.*

These comparisons illustrate how higher N:P expression ratios (3:1) produce larger pseudo-IB condensates that more closely resemble authentic IBs, while cryo-light microscopy confirms that both authentic and pseudo-IBs remain structurally intact under cryogenic conditions. Scale bars: left column, 20 µm; right column, 100 µm.

4.2.4 Room-Temperature TEM and 3D Segmentation of RSV IB Morphology

To gain higher-resolution insights into IB ultrastructure, room-temperature TEM was performed on bRSV-infected cells (MOI 3, 24 hpi). TEM imaging captured the dense core-peripheral phase separation within IBs, supporting their classification as LLPS condensates. Room-temperature TEM was performed by Jennifer Simpson, Professor Pippa Hawes, and Joanna Wells at The Pirbright Institute. I carried out the computational processing of these datasets (Figure 9).

3D segmentation of TEM datasets further resolved internal IB substructures, highlighting distinct IBAGs. These IBAGs appeared as electron-dense compartments within the IB, suggesting potential roles in RNA processing and viral genome organisation.

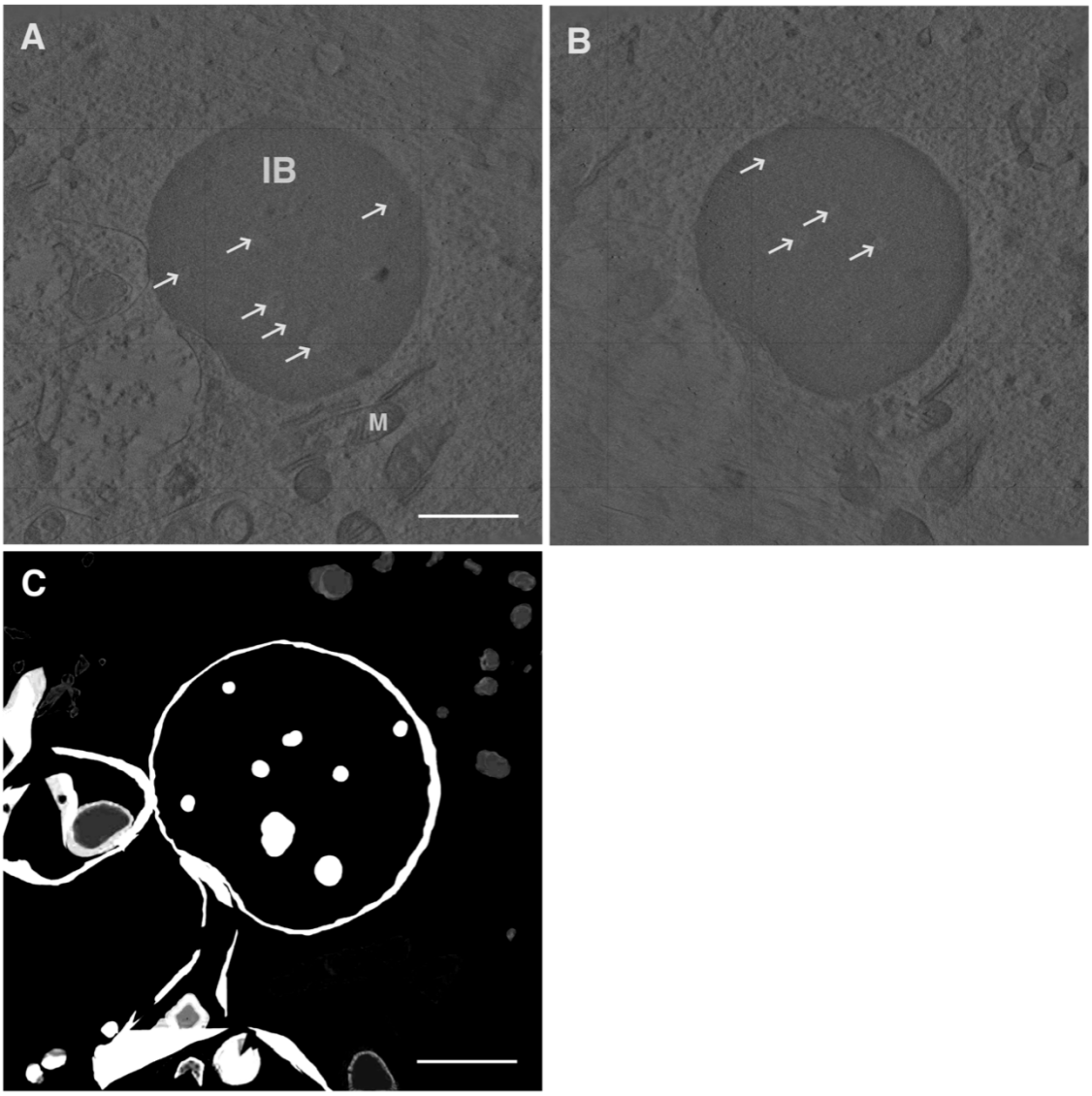


Figure 9: Room-Temperature TEM and 3D Segmentation of RSV IB Morphology. *[A, B] Two tomographic slices from a resin-embedded TEM dataset highlighting an RSV IB with distinct ultrastructural features. White arrows indicate IBAGs, small substructures within the IB. The larger spherical structure is the IB itself (labelled IB), while the adjacent mitochondrion is marked (M). [C] 3D segmentation of the tomogram, generated in IMOD, providing a clear view of the IB and its internal IBAGs, showcasing their distribution and relationship within the cellular context. Room-temperature TEM was done by Jennifer Simpson and Professor Pippa Hawes, The Pirbright Institute. Scale bar: 200 nm.*

4.2.5 TEM Imaging of a Bovine RSV Inclusion Body in Vero Cells

High-magnification TEM images identified ribosomes within IBAGs, providing evidence that these structures may serve as sites of viral translation (Rincheval *et al*., 2017; Jobe *et al*., 2024). The presence of ribosome clusters suggestive of polysomes, consistent with potential local translation, suggests that viral mRNA translation may occur within IBAGs. Notably, these ribosome-containing IBAGs were predominantly located in IB regions with lower electron density, a characteristic often associated with active translation (Figure 10). These findings were potentially reinforced by cryo-tomography data. Sample preparation was performed by Dr Fatoumatta Jobe, Jennifer Simpson, Joanna Wells, and Professor Pippa Hawes. The final TEM dataset was captured by myself.

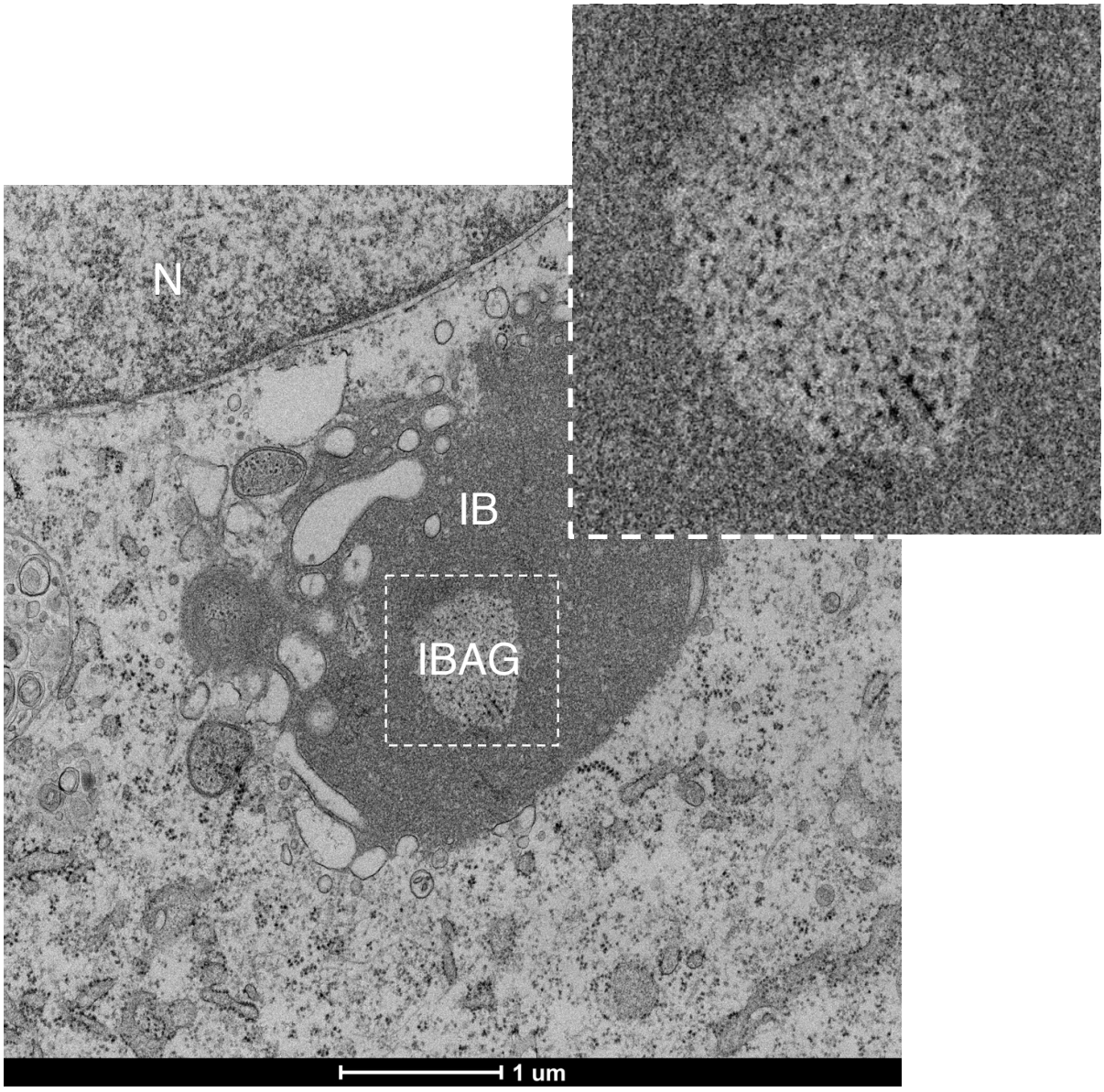


Figure 10: TEM Imaging of a Bovine RSV Inclusion Body in Vero Cells. *Electron micrograph of a bRSV inclusion body (IB) within an infected Vero cell. The sample was prepared by chemical fixation followed by resin embedding, preserving cellular ultrastructure. The IB contains a distinct IB-associated granule (IBAG), visible as a lighter region within the inclusion. Notably, black specks within the IBAG are interpreted as ribosomes, supporting tomography-based findings in this thesis that suggest active translation may occur within IBs. The inset provides a magnified view of the IBAG, highlighting ribosomal density. Sample preparation by Dr Fatoumatta Jobe, Jennifer Simpson, Joanna Wells, and Professor Pippa Hawes; imaging performed by myself. Scale bar: 1 μm.*

4.2.6 Cryo-ET Analysis of Potential LLPS-Driven IBs in bRSV-Infected Vero Cells

To capture cellular ultrastructure, cryo-ET was performed on lamellae from bRSV-infected and co-transfected Vero cells. Tomographic slices revealed electron-dense cytoplasmic condensates with a granular interior and ultrastructural features that could be consistent with phase-separated IBs, such as differential ribosome density and a lack of surrounding membrane (Figure 11; Rincheval *et al*., 2017; Nikolic *et al*., 2017).

One particular structure displayed compartmentalisation into electron-dense ‘islands’ interspersed with regions of lower density. Within these domains, ribosome-sized particles (~20-25 nm) were observed, both within the islands and the surrounding cytoplasm. While correlative fluorescence data was not available to definitively confirm the viral identity of the structure, the observed morphology strongly suggests it may represent a LLPS IB or a related viral replication compartment.

To further assess these particles, manual (n = 910), semi-automated (template matching), and fully automated particle picking was performed using TomoCPT (Shah, Sanchez-Garcia, Stuart, 2025), followed by processing through the Warp-Relion-M pipeline. However, no interpretable sub-volume average could be obtained, likely due to the limited number of particles detected, which falls short of the threshold typically needed for high-quality averaging. These findings emphasise the need for additional high-resolution data collection at a pixel size optimised for ribosome-scale averaging.

In total, four additional condensates with similar electron-dense properties were observed across the dataset, although none could be conclusively verified as bRSV inclusion bodies. Future experiments using cryo-CLEM and more extensive tilt series acquisition will be essential to confirm the viral nature of these compartments and to explore their potential roles in compartmentalised viral replication.

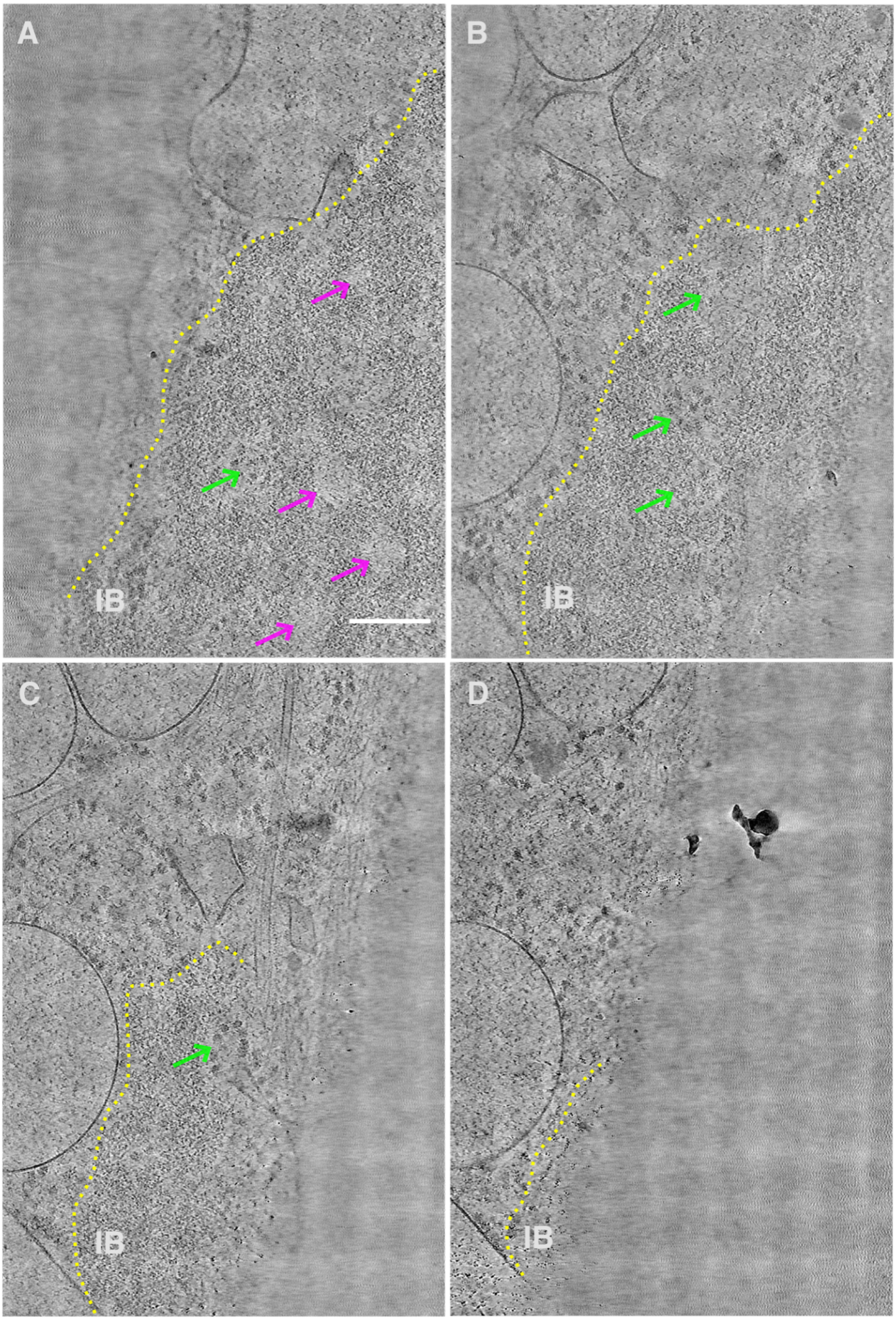

A
IB
B
IB
C
IB
D
IB

Figure 11: Cryo-ET analysis of potential LLPS-driven condensate in bRSV-infected vero cells, MOI 3, 24 hpi. *Panels [A-D] represent sequential tomographic slices of the same condensate, highlighting its internal organisation. The condensate periphery is demarcated by a yellow dotted line, signifying a distinct boundary characterised by altered tomographic density and the exclusion of membranous organelles, consistent with a phase-separated condensate. Green arrows indicate potential IBAGs densely populated with ribosome-like particles, suggesting they may serve as sites of active translation. Pink arrows highlight potential IBAGs that lack ribosomes, potentially reflecting specialised sub-compartments within the condensate. These observations underscore the spatial organisation and functional heterogeneity of these components in facilitating viral replication and immune evasion. Scale bar: 100 nm. TEM Parameters: Pixel size: 2.68 Å/px; Dose rate: 10.62 e^-/px/sec; Tilt range: ±50° with a 2° tilt step; Total dose: 119.85 e^-/Å²; Target dose per tilt: 2.35 e^-/Å²; Exposure time per tilt: 0.799 seconds.*

4.2.7 Cryo-ET Image and Segmentation Model of a Proposed IB in bRSV-Infected Cells

The final cryo-ET segmentation model provided a high-resolution reconstruction of a potential bRSV condensate, capturing the arrangement of viral ribonucleoproteins within suggested IBAGs (Figure 12, adapted from Figure 11). The model further demonstrated that ribosome-like densities were localised within IBAGs, suggesting that translation may occur within these subdomains before nascent viral proteins are exported to the cytoplasm. With an accompanying CLEM overlay, these findings could provide stronger evidence supporting the role of IBs as dynamic biomolecular condensates that are functionally stratified to facilitate viral replication and translation processes, as discussed in Jobe *et al.* (2024).

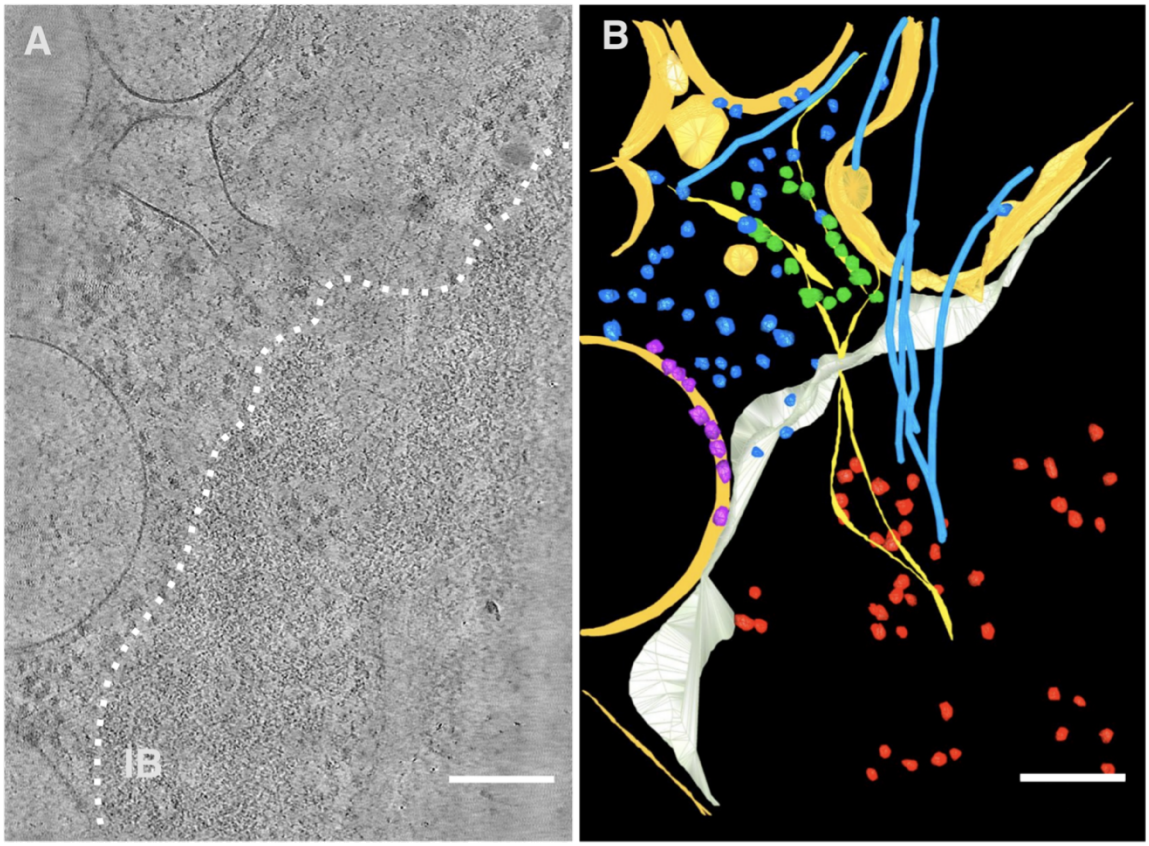


Figure 12: Cryo-ET image and segmentation model of a proposed IB in a bRSV-infected cell, MOI 3, 24 hpi. *[A] Cryo-ET slice showing the LLPS condensate from Figure 11, with its periphery highlighted by a white dotted line. The condensate exhibits a distinct phase-separated boundary, characterised by the exclusion of membranous organelles and a uniform internal density. [B] 3D segmentation of the same tomogram. Key structural elements are colour-coded: red represents internal ribosomes, blue marks external cytoplasmic ribosomes, purple highlights membrane-bound ribosomes, yellow denotes membranous structures surrounding the condensate, and filamentous structures are traced in blue. Scale bar: 100 nm. TEM Parameters: Pixel size: 2.68 Å/px; Dose rate: 10.62 e^-/px/sec; Tilt range: ±50° with a 2° tilt step; Total dose: 119.85 $e^-/Å^2$; Target dose per tilt: 2.35 $e^-/Å^2$; Exposure time per tilt: 0.799 seconds.*

4.3 Equine Rhinitis A Virus Replication Organelles

4.3.1 Lipid Distribution and Nuclear Localisation in ERAV-Infected Vero Cells

To assess changes in host lipid organisation during ERAV infection, fluorescence imaging of lipid-associated probes was performed on Vero cells infected at a MOI of 120. Figure 13 shows a distinct redistribution of lipid membranes, when compared with mock uninfected cells, particularly around the nuclear periphery, where virus-induced membranous structures appear enriched.

While the observed perinuclear lipid accumulation could suggest a role in RO biogenesis, it is important to consider that Golgi dispersal has been reported in related picornavirus infections, such as FMDV. As a result, the BODIPY-labelled lipid structures observed here are unlikely to reflect intact Golgi morphology but may instead represent membrane reorganisation driven by viral replication demands. This redistribution of lipid-rich domains captured in Figure 13 aligns with the proposed role of host membrane remodelling in facilitating viral genome replication and the formation of ROs. BODIPY-ceramide puncta that normally mark intact Golgi in mock cells instead concentrated perinuclearly in infected cells, consistent with the Golgi dispersal and ER-derived membrane remodelling reported for related picornaviruses (Groppelli *et al.*, 2010; Berryman *et al.*, 2016).

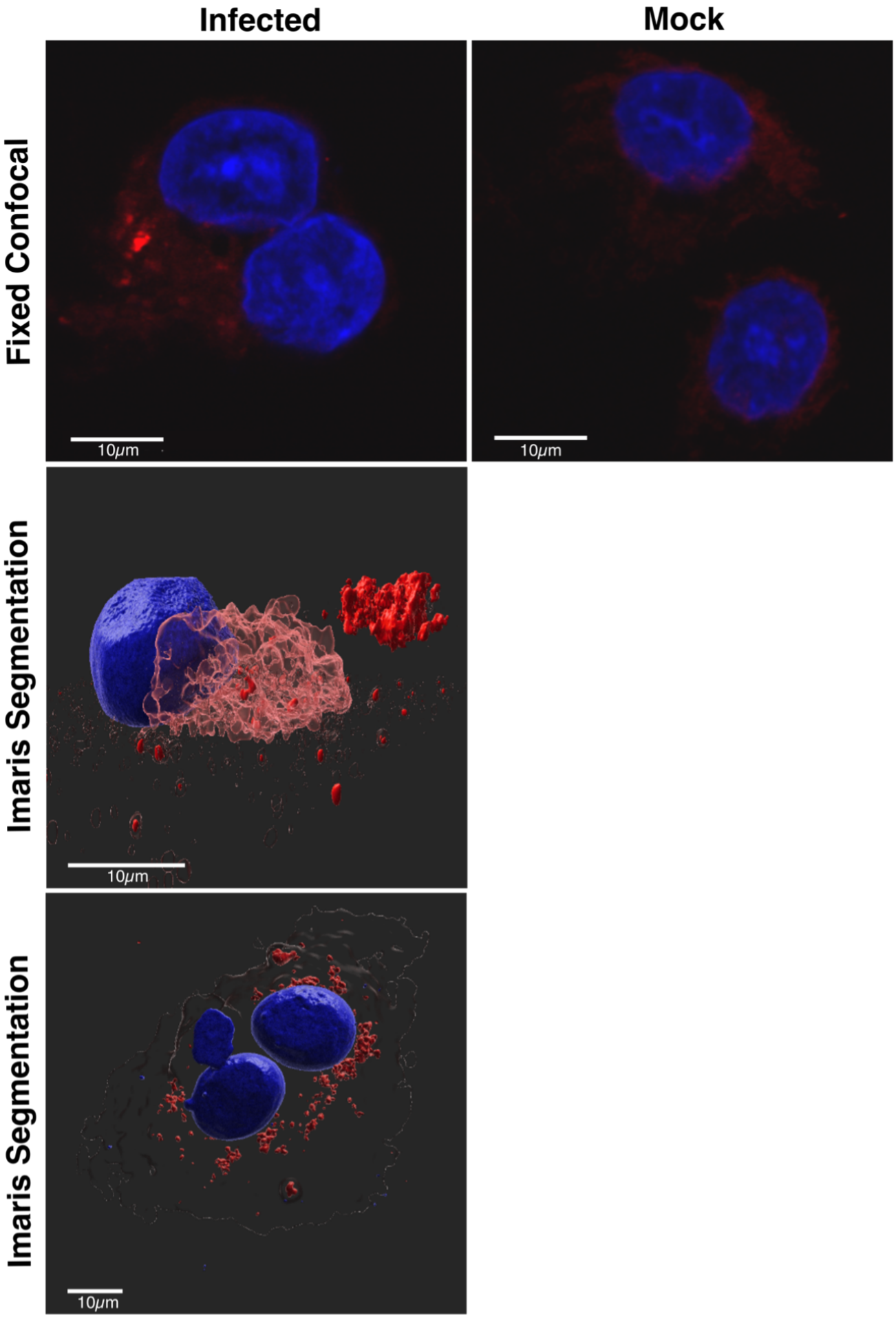

Infected
Mock
Fixed Confocal
10μm
10μm
Imaris Segmentation
10μm
Imaris Segmentation
10μm

Figure 13: Lipid Distribution and Nuclear Localisation in ERAV-Infected Vero Cells, MOI 120. *Infected cells stained with BODIPY™ Ceramide (red) to highlight lipid distribution and Hoechst (blue) for nuclear staining. Top panels display fixed confocal microscopy images, showing red fluorescent lipid accumulations near nuclei, indicating ROs or lipid droplet involvement. Lower panels present 3D segmentations of the infected cell z-stack micrographs, generated in Imaris (Oxford Instruments), illustrating the spatial distribution of lipids and nuclei within the cell. Scale bars: 10 µm.*

4.3.2 Ferrous Ion BioTracker Staining in Mock and ERAV-Infected Cells

To further investigate ERAV-induced membrane remodelling, Ferrous Ion BioTracker staining was used to visualise iron-enriched intracellular compartments (Figure 14). In mock-infected cells, iron-rich vesicles were evenly distributed throughout the cytoplasm. In contrast, ERAV-infected cells showed an enrichment of iron-associated compartments in perinuclear regions, coinciding with viral replication sites.

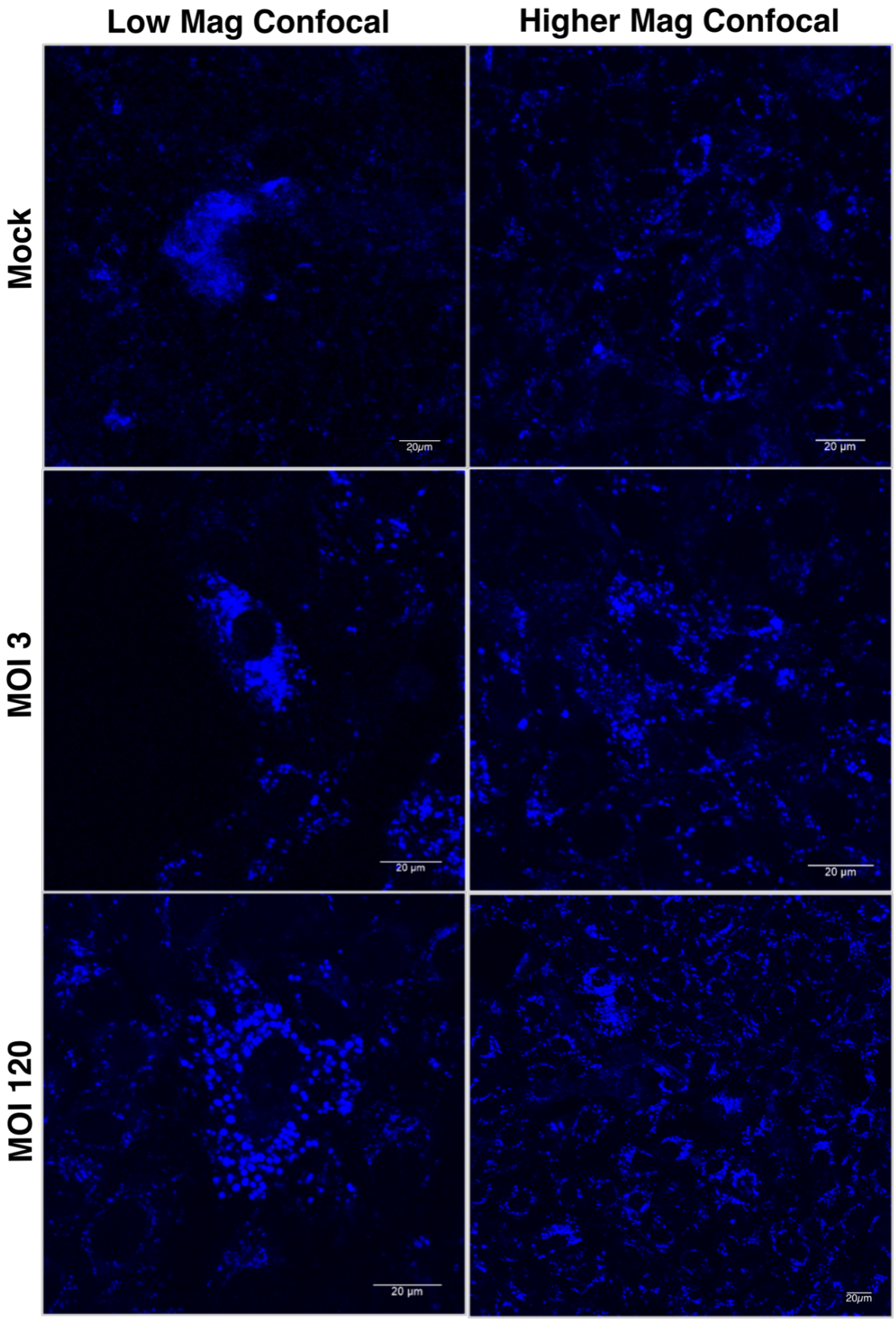

Low Mag Confocal
Higher Mag Confocal
Mock
MOI 3
MOI 120
20μm
20 μm
20 μm
20 μm
20 μm
20μm

Figure 14: Ferrous Ion BioTracker Staining in Mock and ERAV-Infected Vero Cells*. Representative confocal images comparing ferrous ion distribution in mock-infected cells and ERAV-infected cells at MOI 3 and MOI 120, 7 hpi. Panels display low- and higher-magnification views of cells stained with Ferrous Ion BioTracker (blue). The morphological disparities between the mock and increasing viral concentrations; namely the vesicular compartmentalisation of ferrous iron ions correlates with an increased MOI. Thus highlighting potential alterations in iron homeostasis during infection, in membrane-bound perinuclear organelles. Scale bars: 20 μm.*

4.3.3 Visualisation and Segmentation of ERAV Replication Organelles

To characterise the morphology and distribution of ERAV ROs, a correlative workflow incorporating fluorescence microscopy and cryo-ET was used. A total of 140 tilt series were acquired at the electron Bio-Imaging Centre (eBIC, Diamond Light Source) using a nominal magnification of 64,000× (1.97 Å pixel size). Tilt series were pre-processed, aligned using IMOD, and reconstructed in Warp (v1.1.0). Tomograms were denoised using the Noise2Map tool in Warp to enhance structural contrast and visual clarity for downstream analysis.

From this dataset, 76 tilt series were identified as well-aligned and of sufficient quality for detailed analysis. Of these, 19 tomograms revealed membrane-bound structures with morphological features characteristic of picornaviral replication organelles, including SMVs, convoluted membranes, and vesicle clusters (Figure 15). Several vesicles displayed a granular lumenal appearance, closely resembling the protein- and RNA-rich densities reported in poliovirus-induced replication organelles (Dahmane *et*

al., 2019; Dahmane *et al*., 2022), further supporting their identification as functional replication sites. These structures were segmented and visualised at 8 hpi with an MOI of 120, a time point selected to capture the early stages of replication organelle biogenesis. This was informed by previous cryo-ET data from Dr Audrey Lai (11 hpi), which showed more mature RO morphologies (Lai, 2023). Quantitative morphometric segmentation of these structures revealed a heterogeneous size range, reinforcing the hypothesis that ERAV manipulates host membranes in a manner analogous to poliovirus, creating spatially organised domains for genome replication.

Surprisingly, across all 76 tomograms, only 23 virus particles were observed, despite infection at a high MOI and sampling at 8 hpi, a mid-to-late stage of the replication cycle in other picornaviruses. This low virion count may reflect a stage-specific delay in ERAV assembly kinetics, or more likely the limited sampling volume inherent to cryo-ET, where only thin regions of the cell are captured. Further high-resolution imaging and time-course studies are needed to clarify whether the scarcity of particles reflects genuine differences in ERAV replication dynamics or simply technical sampling constraints.

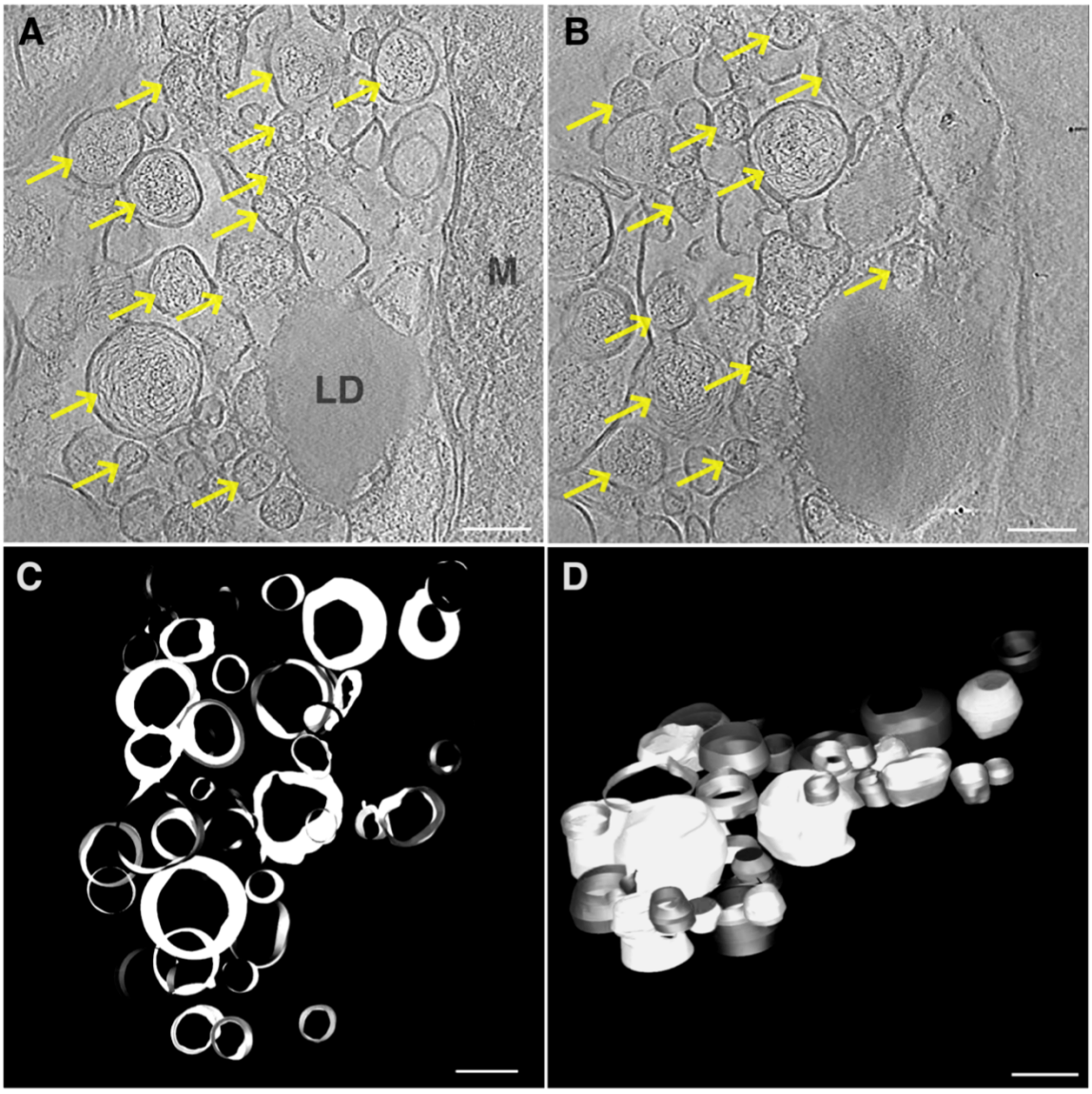


Figure 15: Visualisation and segmentation of ROs in ERAV-infected Vero cells at 8 hpi (MOI 120). *[A, B] Cryo-ET slices from the same tomogram showing ROs (yellow arrows). The surrounding cellular structures include mitochondria (M) and lipid droplets (LD). These images highlight the close spatial association of ROs with lipid and organelle compartments within the cytoplasm. [C, D] 3D segmentation of the ROs from the same tomogram. [C] Top-down view demonstrating the densely packed arrangement of spherical ROs. [D] Side view providing insight into the spatial distribution and uniformity of ROs relative to their surrounding environment. Scale bars: 100 nm. TEM Parameters: Pixel size: 1.97 Å/px; Tilt range: ±50° with a 2° tilt step; Total dose: 119.85 $e^-/Å^2$; Target dose per tilt: 2.35 $e^-/Å^2$; Exposure time per tilt: 0.532 seconds.*

4.3.4 Distribution of SMV Volumes During ERAV Infection

To quantitatively assess SMV dynamics, volumetric analysis of segmented ROs was conducted at 8 and 11 hpi (MOI 120). Figure 16 presents a histogram of SMV size distributions, revealing a shift toward a higher proportion of larger SMVs between these two time points. At 8 hpi, SMVs were predominantly smaller (100-300 nm in diameter), whereas by 11 hpi, larger SMVs (>500 nm) became more frequent.

Rather than a universal size increase, these data suggest a progressive redistribution of SMV sizes, with a greater proportion of larger SMVs emerging at 11 hpi. This could indicate a fusion-driven maturation process, wherein smaller vesicles merge to form larger ROs, potentially optimising viral genome replication and RNA synthesis. Such a mechanism would align with previous observations of RO coalescence in other picornaviruses, where vesicle expansion and interconnection have been described as central to replication organelle maturation (Melia *et al.*, 2019; Dahmane *et al.*, 2022). Further investigation into the dynamics of SMV fusion events could clarify whether this process actively contributes to ERAV replication efficiency.

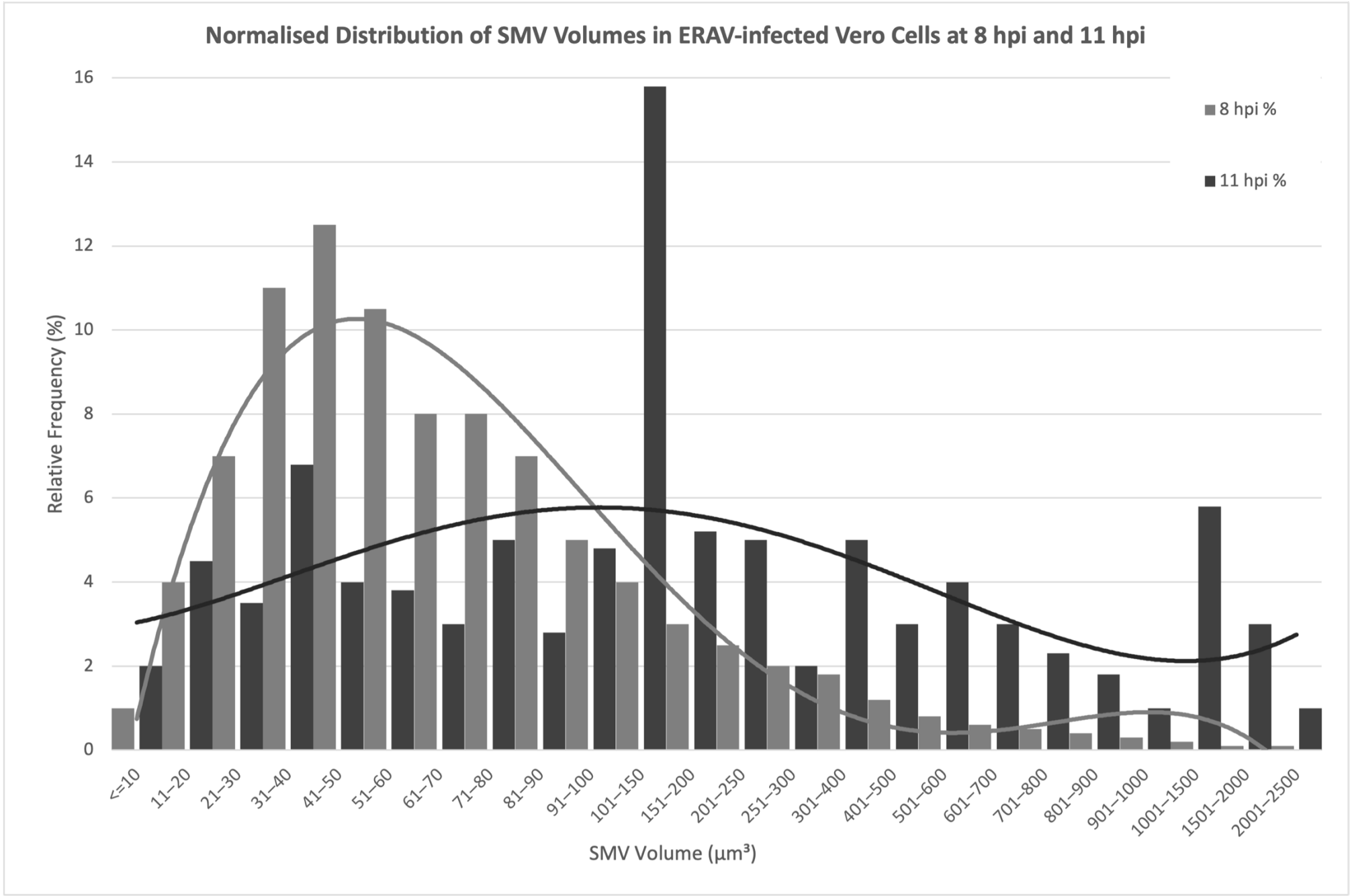

Normalised Distribution of SMV Volumes in ERAV-infected Vero Cells at 8 hpi and 11 hpi
8 hpi %
11 hpi %
Relative Frequency (%)
0
2
4
6
8
10
12
14
16
<=10
11–20
21–30
31–40
41–50
51–60
61–70
71–80
81–90
91–100
101–150
151–200
201–250
251–300
301–400
401–500
501–600
601–700
701–800
801–900
901–1000
1001–1500
1501–2000
2001–2500
SMV Volume (µm³)

Figure 16: Distribution of SMV volumes at 8 and 11 hpi in ERAV-infected Vero cells, MOI 120. *Histogram comparing the relative frequency (%) of SMV volumes at two time points post-infection: 8 hpi (light grey, n = 328) and 11 hpi (black, n = 170). Data were normalised such that the total frequency for each timepoint sums to 100%, enabling direct comparison of volume distributions independent of vesicle counts. Overlaid line plots indicate distribution trends at each timepoint. These findings reveal a shift toward larger SMVs by 11 hpi, consistent with progressive RO maturation. 11 hpi data provided by Dr. Pui Yiu Audrey Lai, University of Oxford.*

4.3.5 Cryo-ET Imaging of ERAV Virions and Their Association with SMVs

To investigate the spatial relationship between ERAV virions and their replication organelles, subtomogram slices were examined from cryo-ET datasets of infected Vero cells at 8 hpi (MOI 120) (Figure 17). Of the 76 tomograms reconstructed, only one instance revealed intact ERAV virions in proximity to replication organelles. Despite the high MOI and sampling at 8 hpi – a stage when many picornaviruses typically accumulate abundant particles – only 23 virions were observed across the dataset, an unexpectedly low number given the conditions of infection. This suggests either a low efficiency of virion maturation or potential challenges in visualising these structures within the captured field of view.

In this single tomogram, ERAV virions were positioned at a remarkably consistent distance from the surface of SMVs, suggestive of a non-random, possibly regulated spatial organisation. This observation may reflect a structured interaction between viral particles and host-derived membranes during the late stages of viral replication.

Closer inspection hinted at filamentous densities – putative tethers – bridging the viral capsids and SMV membranes. While these features could not be definitively resolved, their repeated presence in multiple z-slices lends support to the hypothesis that SMVs may function as docking platforms for viral morphogenesis, acting either as scaffolds for virion assembly or as exit points for trafficking to the plasma membrane.

Small membrane invaginations were also noted at the SMV surface (Figure 17, yellow arrows), possibly indicating budding or envelopment intermediates. These architectural features, although preliminary, align with current models of picornavirus replication organelles (Belov *et al.*, 2012; Melia *et al.*, 2019; Dahmane *et al.*, 2022) and merit further investigation.

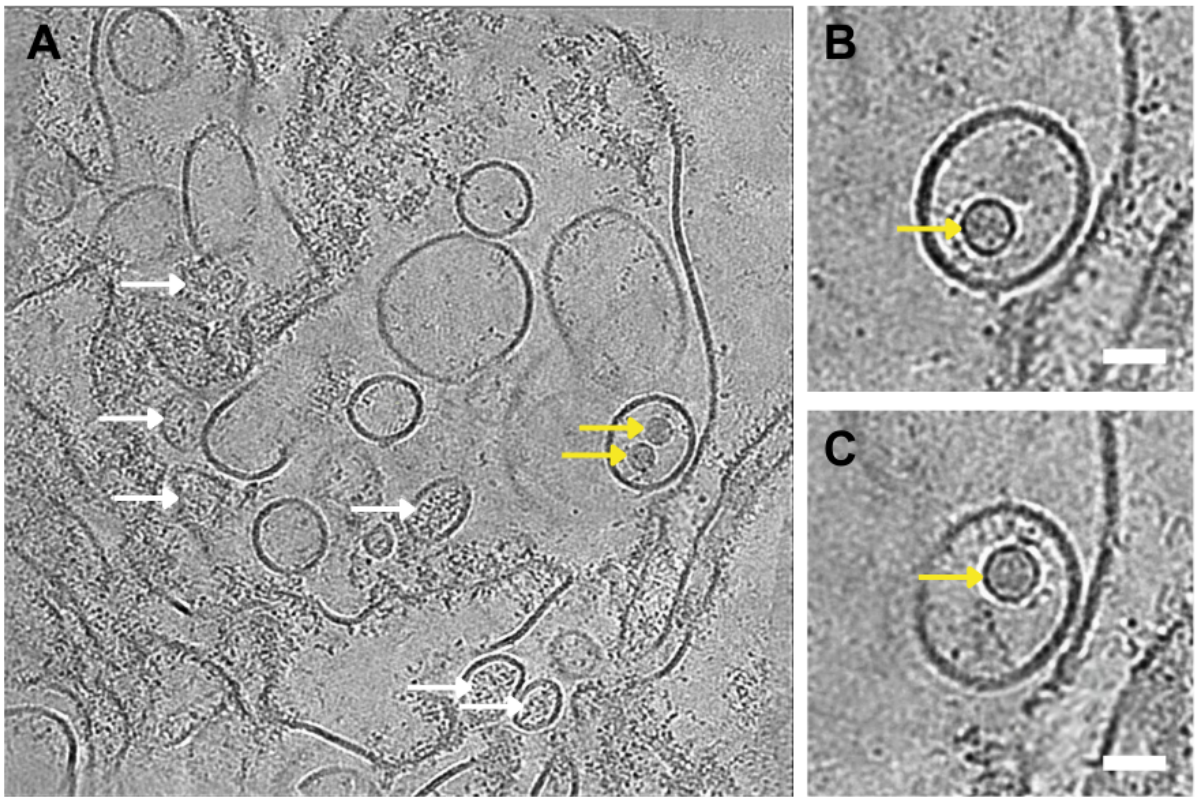


Figure 17: Cryo-ET images of ERAV virions in proximity to SMVs at 8 hpi (MOI 120). *[A] Wide-field cryo-ET slice showing the spatial organisation of small membrane-bound vesicles (SMVs, highlighted with white arrows) and nearby ERAV virions (highlighted with yellow arrows). SMVs display a spherical morphology consistent with ROs, while virions are seen in close association. [B, C] Enlarged views of ERAV virions (yellow arrows) in proximity to SMVs. The images suggest the intimate association between virions and ROs, implying their functional interplay in viral assembly. Scale bars: 30 nm. TEM Parameters: Pixel size: 1.97 Å/px; Tilt range: ±50° with a 2° tilt step; Total dose: 119.85 $e^-/Å^2$; Target dose per tilt: 2.35 $e^-/Å^2$; Exposure time per tilt: 0.532 seconds.*

Quantitative Analysis of SMV Properties During ERAV Infection

To obtain a comprehensive overview of SMV characteristics throughout infection, quantitative analysis was conducted on a dataset of segmented ROs at 8 and 11 hpi (MOI 120) (Table 2). The mean SMV volume increased from ~1.6×10^5 nm³ (~70 nm diameter) at 8 hpi to ~4.3×10^5 nm³ (~95 nm diameter) at 11 hpi, supporting the observed trend of RO expansion over time. Variability was assessed using standard deviations and confidence intervals, which provided a more robust measure of spread than simple maximum-minimum ranges.

The Mean 3D Volume Ratio was used as a quantitative measure of SMV morphology, providing an alternative to traditional sphericity calculations. This metric assesses how closely the observed SMV volume approximates a reference volume, offering insights into SMV shape without assuming a perfect sphere. Unlike sphericity, which depends on surface area measurements that may be influenced by imaging resolution and segmentation variability, the Mean 3D Volume Ratio provides a robust, dimensionless indicator of SMV compactness and structural changes over time. This approach enables comparisons of SMV morphology across different conditions while minimising artefacts introduced by surface and computational irregularities.

Table 2: Quantitative analysis of SMV properties during ERAV infection at 8 and 11 hpi, MOI 120. *Morphometric characteristics of segmented SMVs are summarised at two infection time points. Data at 11 hpi were provided by Dr Pui Yiu Audrey Lai (University of Oxford). Mean volumes, standard deviations, and confidence intervals are reported to capture central tendency and variability. The standard deviation values are presented in preference to simple range, as they provide a more robust description of distribution spread.*

Metric	**8 hpi**	**11 hpi**
Mean 3D Volume Ratio	0.72	0.73
Mean 3D Volume Ratio **SD**	0.04	0.05
Mean Volume (nm^3)	162560	434417
Mean Volume (nm^3) **SD**	290068	582387
Mean Volume (nm^3) % Change	N/A	167
Sample Size	328	170
Mean Volume Confidence Interval	131168 to 193952	346870 to 521965
Mean 3D Volume Ratio Confidence Interval	0.711 to 0.720	0.718 to 0.732

5. Discussion

5.1 Evaluation of Imaging-Based Approaches

This study applied a multimodal imaging workflow to characterise RSV IBs and ERAV ROs, providing comparative insights into two distinct replication strategies: LLPS-driven condensates versus membrane-bound vesicles. Cryo-ET resolved the ultrastructure of ERAV ROs with high fidelity, while the absence of a membrane boundary in RSV IBs posed a major challenge, necessitating fluorescence-guided segmentation (Figure 13). Although this introduced potential artefacts, it nevertheless enabled ribosome localisation within IBAGs, offering evidence of translation competence.

5.1.1 Contrast Limitations in RSV Inclusion Body Imaging

Unlike membrane-bound ROs, RSV IBs exhibited low electron density, making it difficult to resolve their internal organisation using cryo-ET alone (Figure 12). To overcome this limitation, fluorescence imaging was used to clarify IB structures. While this approach provided valuable spatial information, it introduced two key challenges. First, the reliance on computational segmentation for tomograph interpretation rather than true electron contrast posed the risk of oversimplifying IB subdomains, such as IBAGs, potentially leading to misinterpretation of their structural organisation. The absence of a defined membrane boundary meant that IBs were identified based on fluorescence intensity rather than intrinsic physical features, increasing the likelihood of segmentation artefacts.

Second, correlating fluorescence and cryo-ET data introduced misalignment issues. Although post-vitrification fluorescence imaging provided a useful spatial reference for IB localisation, ice contamination and fluorescence signal drift occasionally led to discrepancies when aligning these images while generating lamella (Figures 7 and 8).

To address these challenges, future studies could integrate phase plate cryo-ET, which enhances contrast for low-density structures by reducing phase contrast loss, allowing for better visualisation of IBs and their internal subdomains (Tegunov and Cramer, 2019). Another promising approach is cryo-soft X-ray tomography, which provides label-free imaging of biological structures at near-native states, allowing IB architecture to be visualised without relying on fluorescence-based segmentation (Oikonomou and Jensen, 2023; Spink *et al.*, 2018). Additionally, using live-cell super-resolution microscopy before cryo-fixation could help track IB formation in real time, ensuring that the structures observed in fixed samples accurately represent biologically relevant states.

5.1.2 Replication Organelle Classification and Quantification Challenges

Cryo-ET successfully captured the morphological diversity of ERAV-associated replication structures at two infection timepoints, including vesicles consistent with SMVs described in previous ERAV studies (Figure 16). While mock-infected Vero cells were used throughout the infection protocol as qualitative controls for monitoring cytopathic effects, dedicated cryo-ET datasets were not collected from uninfected

cells. This decision reflected the high experimental cost of lamella preparation and Krios acquisition, which prioritised maximising data from infected samples. As such, the attribution of these vesicles as virus-induced relies on comparisons with prior reports of *aphthovirus* ROs (Berryman *et al*., 2016; Groppelli *et al*., 2010), as well as the clear absence of comparable vesicular morphologies in uninfected control cells observed at the light microscopy level.

Classification of these vesicles presented two key challenges. First, vesicle heterogeneity was evident in quantitative analysis (Table 2), which showed a significant increase (by 167%) in SMV volume between 8 and 11 hpi. Despite this overall trend, considerable size variation was observed within each time point, suggesting that vesicle development may be influenced by biological heterogeneity or sampling biases introduced by cryo-ET field selection, milling strategies, or segmentation limitations. This variability complicates attempts to define a clear developmental trajectory for SMVs within the viral replication cycle.

Additionally, the functional distinction between the developmental relationship between SMVs and DMVs remains unresolved. While SMVs were prevalent at early time points, it is unclear whether they serve as active sites of viral RNA replication or function as precursors to DMVs. Future studies could clarify this by using fluorescent viral RNA labelling to determine whether viral RNA synthesis occurs predominantly within SMVs or if they transition into DMVs as infection progresses.

To improve vesicle classification accuracy, automated machine learning-driven segmentation could be implemented to reduce subjectivity and increase dataset throughput. This approach would enable high-throughput quantitative analysis, allowing for more precise correlations between vesicle morphology and replication function while minimising operator bias in vesicle identification.

5.1.3 Tethering Structures: Potential for Functional Significance?

Filamentous tether-like structures were observed in only one instance between ERAV virions and an SMV, but it is consistent with Lai (2020) – suggesting a potential role in viral docking, genome packaging, or trafficking (Figure 17B and C). While our dataset was limited in scope, similar structures have been described extensively in previous ERAV studies. Lai (2020) reported frequent tethers connecting both full and empty virions to SMVs and DMVs, with variable lengths and widths distinct from the more uniform ~6 nm tethers observed in enteroviruses (Dahmane *et al*., 2022). Quantitative measurements revealed that empty virions often tethered closer to membranes (~5.6 nm) compared to full virions (~8 nm), raising the possibility that some of these structures represent viral genomes extending from capsids into replication organelles. In addition, virions tethered to autophagic-like membranes were occasionally observed, suggesting that tethers may also contribute to unconventional secretion or degradation pathways (Lai, 2020).

The functional significance of these tethering structures remains unresolved, but they may play a role in spatially organising virion assembly and release. In other viral

systems, tethering interactions have been attributed to direct protein linkages, lipid-mediated attachment, or host-derived scaffolding elements. For example, in FMDV, the viral 3C protease interacts with host cytoskeletal proteins, including vimentin and microtubules, leading to their redistribution around viral replication sites (Armer *et al*., 2008). This suggests a possible cytoskeleton-mediated mechanism for virion tethering in aphthoviruses. Structural studies further indicate that FMDV capsid rearrangements influence genome encapsidation and particle stability, potentially facilitating tethering interactions with ROs (Malik *et al*., 2017). If ERAV follows similar assembly dynamics, capsid conformational changes could underpin tethering to SMVs.

Future work should aim to expand tomographic datasets to strengthen the statistical basis of these observations. Given sufficient particle numbers, subtomogram averaging could provide a high-resolution view of tether structures, while geometric modelling might clarify whether virion-SMV distances deviate from random association. Additionally, immunolabelling of cytoskeletal and trafficking proteins could establish whether host-derived scaffolding components, such as actin or microtubule-associated factors, contribute to tether formation. Building on both the preliminary data presented here and the more extensive findings of Lai (2020), such approaches may clarify whether tethering represents a conserved mechanism of virion maturation and release within aphthoviruses.

5.1.4 Future Imaging Considerations

While this study presents a framework for quantitative viral RO analysis, several imaging refinements could further enhance future investigations. A key priority would be integrating live-cell fluorescence tracking with cryo-ET, which would ensure that IB and RO structures remain biologically relevant post-vitrification. The challenges of post-vitrification fluorescence misalignment (Figures 7 and 8) and reliance on computational segmentation of IBs (Figure 12) highlight the need for real-time tracking of IB dynamics before cryo-fixation. This would help distinguish between transient and stable substructures, reducing the risk of artefacts introduced during sample preparation.

Increasing the throughput of cryo-FIB milling would also improve the statistical power of ultrastructural analyses by allowing for a greater number of high-quality lamellae per experiment (Figure 4). Automated milling strategies, combined with AI-assisted computational processing, could enhance reproducibility and dataset consistency across different infection conditions.

Finally, correlating cryo-ET data with biochemical assays would provide molecular validation of structural observations. For example, while Figure 16 reveals size heterogeneity in SMVs, it remains unclear whether these changes correspond to specific lipid or RNA composition shifts. Integrating mass spectrometry-based lipidomics could clarify membrane composition differences between SMVs and DMVs, while RNA-seq and CLIP-seq could provide a more detailed understanding of viral and

host RNA localisation within IBs. RNA-seq has been successfully applied to profile viral and host RNA dynamics within SARS-CoV-2 ROs, demonstrating its utility in identifying replication-associated RNA species (Sun *et al*., 2021). Similarly, CLIP-seq has enabled nucleotide-resolution mapping of RNA-protein interactions (Zhou *et al*., 2021), which could distinguish actively replicating viral RNA from sequestered transcripts within IBs. These multimodal approaches would bridge the gap between ultrastructural imaging and functional insights, refining our understanding of how RSV IBs and ERAV ROs contribute to viral replication and immune evasion.

5.2 Biological Implications and Model Refinements

The findings from this study contribute to a growing understanding of how RNA viruses restructure intracellular environments to optimise replication. RSV IBs and FMDV/ERAV ROs exemplify two contrasting viral strategies, membraneless phase-separated condensates and membrane-bound ROs, each with distinct advantages, constraints, and evolutionary trade-offs.

5.2.1 RSV IBs: Strengths and Limitations as Viral Replication Sites

RSV IBs were confirmed to be liquid-like, phase-separated condensates containing internal substructures, IBAGs, which are enriched in ribosomes, viral mRNA, and translation machinery, depicted in Figure 18. Their highly dynamic nature likely allows RSV to adapt to fluctuations in host cell conditions, facilitating the coordination of

transcription and translation. However, this membraneless organisation may also introduce vulnerabilities that could affect viral replication efficiency.

One major limitation of IBs is their sensitivity to environmental distress (Galloux *et al*., 2020). The biophysical properties governing LLPS depend on molecular interactions that can be disrupted by changes in ionic strength, osmotic pressure, or small-molecule modulators (Hyman *et al*., 2014; Li *et al*., 2012). As demonstrated in Figure 11, IBs exhibited relatively low electron density, requiring fluorescence-guided segmentation to define their structure. This highlights their inherently diffuse nature, which may leave them susceptible to external factors. The effects of small-molecule inhibitors such as 1,6-hexanediol, which disrupt weak hydrophobic interactions, have been demonstrated in other phase-separated systems, raising the possibility that RSV IBs could be pharmacologically destabilised, thereby impairing viral replication (Rincheval *et al*., 2017; Zhang *et al*., 2023).

While IBs function to sequester viral RNA away from host pattern recognition receptors, they lack a physical membrane barrier, potentially leaving them vulnerable to host-mediated disassembly mechanisms. Unlike the membrane-bound ROs of picornaviruses, which provide structural insulation against cytosolic antiviral detection (Doyle *et al*., 2019), RSV IBs are exposed to host cellular stress responses. In particular, their gel-like morphology may allow host degradation pathways to target viral replication intermediates (Tollervey *et al*., 2022). This vulnerability is highlighted by the heterogeneous appearance of IBs in Figure 8, where differences in fluorescence intensity suggest that IB stability may be influenced by cellular

conditions. Understanding how IBs evade host cell stress responses and innate immune activation will be critical for determining their stability under host-imposed antiviral pressures.

Ribosome-rich IBAGs (Figures 6 and 10) suggest localised translation competence, yet their non-uniform density (Figure 12) leaves open whether they act as default translation factories or transient storage hubs for viral mRNA (Jobe *et al.*, 2024). Resolving this ambiguity will be central to understanding how RSV organises gene expression within IBs.

Beyond these limitations, the broader spatial organisation of IBs highlights their role as integrated replication hubs. Subdomains such as IBAGs concentrate ribosomes and translation initiation factors (eIF4E, eIF4G, eIF4A), suggesting that viral mRNA processing and translation may be spatially regulated (Rincheval *et al.*, 2017; Jobe *et al.*, 2020). In 3D reconstructions, IBAGs appeared as discrete sub-compartments lacking obvious continuity with the cytoplasm, raising questions about how viral mRNA traffics out of IBs. It remains unclear whether IBAGs are dedicated translation factories or transient processing stations prior to cytosolic export.

The presence of an N^0P ring around IBs suggests a regulated entry-exit mechanism for viral proteins, potentially preventing premature RNA binding. Size heterogeneity further supports a model of IB growth driven by accumulating RNA and proteins (Jobe *et al.*, 2024). Comparative work with pseudo-IBs demonstrated that the N:P expression

ratio is critical for condensate formation, with higher N:P ratios generating larger, more wild-type-like inclusions (Galloux *et al.*, 2020).

Cytoskeletal associations were also observed, suggesting that IB positioning may be stabilised by host structural scaffolds. This is consistent with other viral systems: Ebolavirus IBs dynamically reorganise around cytoskeletal filaments (Hoenen *et al.*, 2012), mammalian orthoreovirus factories exploit microtubule networks (Lee *et al.*, 2025), and plant rhabdoviruses leverage actin filaments for IB motility (Liang *et al.*, 2023). These parallels indicate that RSV IBs may exploit cytoskeletal interactions to regulate spatial organisation, facilitate mRNA trafficking, and shield replication processes from host defences.

The compartmentalisation of RSV IBs mirrors other phase-separated organelles, such as PML nuclear bodies, which organise transcriptional regulators and antiviral proteins within distinct subdomains (Banani *et al.*, 2017). Like PML-NBs, IBs may enhance viral protein production by locally concentrating mRNAs and ribosomes while excluding antiviral effectors. Proteomic analysis of purified IBs and IBAGs, although technically challenging, could provide a powerful means of identifying scaffolding and client proteins. Precedent exists in rabies Negri bodies (Nikolic *et al.*, 2017) and measles IBs (Zhou *et al.*, 2019), where phase-separated viral organelles were shown to recruit both viral and host proteins.

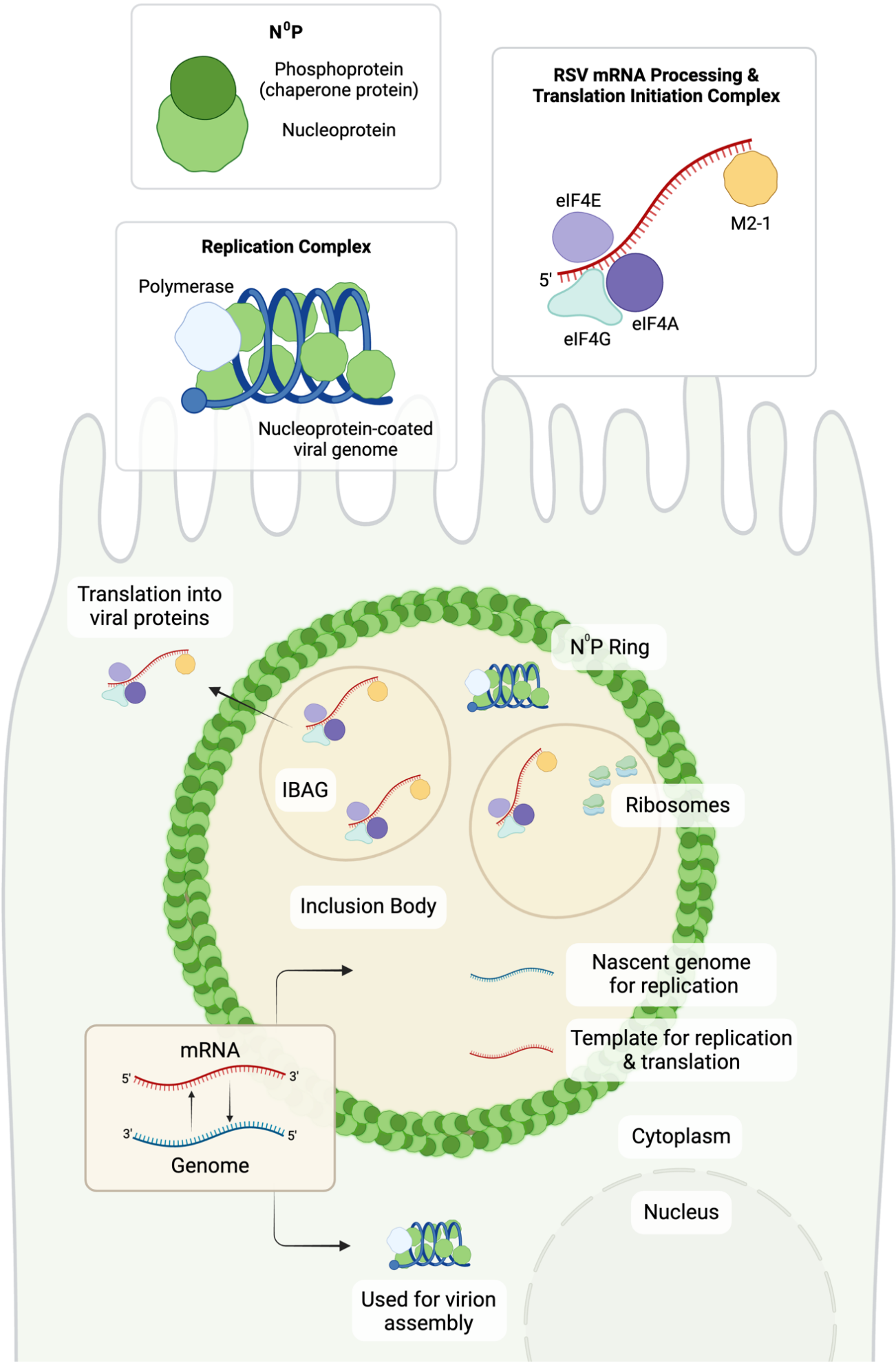

N⁰P
Phosphoprotein
(chaperone protein)
Nucleoprotein
RSV mRNA Processing &
Translation Initiation Complex
eIF4E
M2-1
5'
eIF4A
eIF4G
Replication Complex
Polymerase
Nucleoprotein-coated
viral genome
Translation into
viral proteins
N⁰P Ring
IBAG
Ribosomes
Inclusion Body
Nascent genome
for replication
Template for replication
& translation
mRNA
5'
3'
3'
5'
Genome
Cytoplasm
Nucleus
Used for virion
assembly

Figure 18: Proposed Spatial Organisation of RSV Inclusion Bodies and Their Role in Viral Genome Replication and Translation. *This schematic illustrates the compartmentalisation of RSV IBs, which serve as sites for viral RNA synthesis, nucleocapsid assembly, and translation regulation. Subdomains such as IBAGs concentrate ribosomes and translation initiation factors, while an N^0P ring surrounds the IB, regulating protein entry. The model highlights how IBs coordinate viral replication, gene expression, and assembly while evading host defences.*

Taken together, these findings support a refined model in which RSV IBs act as multifunctional centres of transcription, translation, and immune evasion. Their liquid-like nature provides flexibility but also vulnerability, contrasting with the structural stability of picornavirus ROs. Open questions remain about the regulation of N^0P entry, the precise function of IBAGs, and the trafficking of viral mRNAs from IBs to the cytoplasm. Future studies combining live-cell super-resolution microscopy, FRAP, and proteomics will be critical for resolving these mechanistic questions and clarifying how RSV leverages LLPS to optimise replication.

5.2.2 ERAV ROs: Structural Stability and Metabolic Dependency

Unlike RSV IBs, ERAV ROs exhibited greater structural stability, forming well-defined SMVs that compartmentalise viral RNA synthesis. This membrane-based strategy provides a physical barrier against host immune sensors, shielding viral replication intermediates from pattern recognition receptors (Dolnik *et al.*, 2021; Doyle *et al.*, 2019).

A key requirement for ERAV RO biogenesis is its dependence on Golgi and ER-derived membranes, a feature consistent with other picornavirus replication compartments (Belov and van Kuppeveld, 2012; Lanke *et al*., 2009). As demonstrated in Figure 17, SMVs are observed in close proximity to cellular membranes, though direct association with host-derived membranes was not observed in this dataset. Given the structural similarities between FMDV and ERAV ROs, a comparable lipid dependency in ERAV suggests that targeting vesicle biogenesis could represent a viable antiviral strategy.

Beyond lipid dependence, the energetic cost of vesicle biogenesis presents another potential constraint on viral replication efficiency. Quantitative analysis (Table 2) revealed a 167% increase in mean SMV volume between 8 and 11 hpi, suggesting that vesicle expansion is an active, energy-intensive process. The formation of large pleomorphic ROs at later time points could indicate that viral replication places increasing demands on host lipid synthesis and membrane trafficking. This raises the possibility that under conditions of cellular stress or co-infection, host metabolic limitations may restrict RO expansion, reducing overall viral replication efficiency. Our volumetric data suggest SMVs evolve functionally over time, with smaller vesicles enriched at early replication stages and enlarged vesicles later supporting assembly, echoing maturation pathways described in poliovirus and enteroviruses (Melia *et al*., 2019; Dahmane *et al*., 2022).

In addition to lipid metabolism, our observations of iron-associated vesicles enriched near ERAV ROs suggest that host iron homeostasis may also be co-opted during

infection. Iron can influence membrane properties and redox balance, potentially supporting vesicle formation or stability. Future experiments could test whether these iron-rich compartments colocalise with viral proteins such as ERAV 3A, for example using antisera-based immunofluorescence. If confirmed, this would expand the picture of RO metabolic dependency beyond lipids to encompass iron homeostasis, hinting at a multi-faceted host resource hijack. Such studies would clarify whether iron-rich vesicles directly contribute to RO biogenesis, expanding our understanding of the metabolic dependencies that sustain *aphthovirus* replication.

Finally, the volumetric data and cryo-ET imaging presented here suggest that ERAV ROs may undergo a functional maturation process. Early-stage SMVs are likely to represent highly active sites of genome replication, whereas later-stage, enlarged SMVs may shift toward supporting virion assembly and release. This interpretation aligns with previous work on enteroviruses and poliovirus, where replication organelles were shown to transition structurally and functionally over the course of infection (Melia *et al.*, 2019; Dahmane *et al.*, 2022). These parallels highlight the possibility that ERAV, like other picornaviruses, reprograms host membranes not only to create protective replication niches but also to choreograph the temporal progression from RNA synthesis to virion maturation.

FMDV ROs resemble the vesicular replication structures of hepatitis C virus and poliovirus (Roingeard *et al.*, 2022; Dahmane *et al.*, 2022). Further work employing live-cell lipidomics and metabolic tracing assays could determine whether ERAV preferentially recruits specific lipid species to sustain RO biogenesis.

5.3 Future Directions and Open Questions

5.3.1 Investigating IBAG Formation and Function

Despite progress in characterising RSV IBs, the precise role and formation dynamics of IBAGs remain unresolved. A critical question is whether IBAGs represent structurally distinct, stable compartments or whether they dynamically form and dissolve depending on the viral replication stage. As suggested in Figure 11, ribosome-rich IBAGs are embedded within IBs, but their heterogeneous distribution suggests they may undergo regulated assembly and disassembly in response to transcriptional and translational demands. Understanding this process is essential for determining whether IBAGs act as transient hubs for translation or serve longer-term compartmentalisation roles within IBs.

One possibility is that IBAGs enhance translation initiation efficiency by concentrating viral mRNA within a defined subregion of the IB. This localisation effect could increase ribosomal loading onto viral transcripts, optimising translation while shielding mRNAs from host immune detection (Jobe *et al.*, 2020). However, the extent to which IBAGs actively regulate translation remains unclear. While ribosomes and translation initiation factors have been observed within membraneless entities, analogous to IBAG structures, (Figure 10; Jobe *et al.*, 2020), the degree of mRNA enrichment has yet to be quantified.

Addressing these theories will provide deeper insights into how RSV IBs coordinate transcription and translation within a membraneless environment and whether IBAGs function as viral ‘translation factories’ or temporary storage sites for mRNA and ribosomal complexes. Clarifying whether IBAGs act as translation factories or transient RNA storage sites will be essential for refining models of RSV replication.

5.3.2 Resolving the Role of Tethering Structures in ROs

Cryo-ET imaging of ERAV-infected cells revealed, in one instance, filamentous tether-like structures linking virions to an SMV (Figure 17). Together with previous observations (Lai, 2020), this raises important questions about their functional significance. A central issue is whether such tethers actively mediate virion docking and genome packaging, or whether they instead reflect structural artefacts introduced during sample preparation. Similar virion-membrane associations have been reported in other picornaviruses (Armer *et al*., 2008; Dahmane *et al*., 2022), suggesting that ERAV may employ conserved mechanisms to anchor virions to ROs. However, the molecular composition of these tethers and their precise role in viral assembly remain unresolved.

One possibility is that virions dock at RO membranes to initiate or regulate genome encapsidation, with tethering interactions mediated by viral capsid proteins or host-derived scaffolding elements. To test whether these structures are spatially organised rather than random, future studies could increase the number of virion-positive tomograms and apply geometric modelling approaches. For example, virion capsids

could be represented as spheres and SMVs as ellipsoidal membranes within segmented 3D models, enabling calculation of inter-structural distances. Consistent virion-membrane spacing across multiple tomograms would strengthen the case that tethering is a genuine assembly feature rather than a coincidental alignment. Whether these tethers are definitive viral structures or fixation artefacts remains unresolved, where additional tomograms are essential to establish biological significance.

In parallel, immunolabelling of host cytoskeletal and trafficking proteins could help determine whether host components, such as actin or microtubule-associated factors, contribute to tether formation. Given that FMDV 3C protease remodels vimentin and microtubules to support replication (Armer *et al*., 2008), ERAV may similarly exploit cytoskeletal elements to position ROs and facilitate virion assembly or egress. Establishing whether virion-SMV tethers are structured assembly intermediates or artefacts will determine how ERAV organises morphogenesis.

5.3.3 Targeting Viral Replication Compartments as Therapeutic Strategies

The structural and functional differences between RSV IBs and FMDV ROs present distinct opportunities for antiviral intervention. RSV IBs, as membraneless, liquid-like condensates, could be destabilised using small molecules that disrupt phase separation, whereas FMDV ROs, which rely on host-derived lipid membranes, may be targeted through metabolic inhibitors that disrupt vesicle biogenesis.

A key strategy for RSV involves using small-molecule phase modulators to interfere with LLPS and disrupt IB integrity. Studies on other phase-separated viral compartments suggest that hexanediol, which disrupts weak hydrophobic interactions, or synthetic peptides targeting intrinsically disordered regions in N and P proteins could prevent IB formation or accelerate their dissolution (Galloux *et al.*, 2020). However, it remains unclear whether RSV can compensate for IB disruption by redistributing replication complexes throughout the cytoplasm. Future experiments should test whether phase-separation inhibitors affect RSV replication efficiency or induce alternative compartmentalisation mechanisms.

For FMDV ROs, a more effective strategy may involve selective host pathways sustaining RO biogenesis, as these replication structures depend on continuous membrane trafficking from the Golgi and ER. Lipidomic profiling of ROs could identify specific host pathways essential for vesicle formation, providing candidate targets for pharmacological inhibition. However, the specific lipid composition of ERAV/FMDV ROs has not been fully characterised, highlighting the need for lipidomics-based approaches to map the host-derived lipid dependencies of these structures. Antivirals directed at host factors may offer broad-spectrum potential, such as disrupting both FMDV and other positive-RNA viruses.

By integrating imaging-based structural analysis with biochemical approaches, future work can determine whether targeting viral replication compartments represents a viable broad-spectrum antiviral strategy. Disrupting phase-separated IBs or membrane-derived ROs could impair viral replication at the subcellular level,

presenting novel avenues for host-directed antiviral therapies. Targeting phase separation or RO lipid dependencies represents a promising antiviral avenue but requires careful mapping of host factors to minimise off-target effects.

6. Conclusion

This study provides a comparative structural analysis of RSV IBs and ERAV ROs, two functionally distinct viral replication compartments. Using cryo-ET, correlative fluorescence microscopy, and quantitative segmentation, this work highlights both the strengths and limitations of current bioimaging workflows, while identifying opportunities to integrate additional modalities such as spatially resolved mass spectrometry and RNA-seq in future studies.

RSV IBs, as membraneless, liquid-like condensates, exhibit dynamic phase-separated organisation with internal substructures (IBAGs) enriched in ribosomes and viral mRNA, potentially facilitating translation within the cytoplasm. By contrast, ERAV ROs, as membrane-bound replication factories, provide a structurally insulated environment that shields viral RNA synthesis from host immune surveillance, but at the cost of imposing a high metabolic burden on the host cell.

The contrasting architectures of RSV IBs and ERAV ROs underscore the divergent strategies viruses employ to balance adaptability, efficiency, and immune evasion. These findings refine our understanding of how viral replication compartments are organised and present both methodological challenges and new opportunities for bioimaging-guided antiviral discovery.

7. References

Abrams, E.M., Doyon-Plourde, P., Davis, P., Lee, L., Rahal, A., Brousseau, N., Siu, W. and Killikelly, A. (2025). Burden of disease of respiratory syncytial virus in older adults and adults considered at high risk of severe infection. *Canada Communicable Disease Report*, 51(1), p.26.

Acharya, R., Fry, E., Stuart, D., Fox, G., Rowlands, D. and Brown, F. (1990). The structure of foot-and-mouth disease virus: implications for its physical and biological properties. *Veterinary Microbiology*, 23(1-4), pp.21-34.

Alenquer, M., Vale-Costa, S., Etibor, T.A., Ferreira, F., Sousa, A.L. and Amorim, M.J. (2019). Influenza A virus ribonucleoproteins form liquid organelles at endoplasmic reticulum exit sites. *Nature Communications*, 10(1), p.1629.

Ali, M.Z., Dewan, D., Khan, M.M.R. and Meher, M.M. (2024). Prevalence, genetic characteristics and economic losses of Foot-and-Mouth Disease Virus (FMD) in global and Bangladesh context: A Review. *Ukrainian Journal of Veterinary and Agricultural Sciences*, 7(2), pp.8-19.

Alshareedah, I. and Banerjee, P.R. (2022). Measurement of protein and nucleic acid diffusion coefficients within biomolecular condensates using in-droplet fluorescence correlation spectroscopy. In Phase-Separated Biomolecular Condensates: Methods and Protocols (pp. 199-213). New York, NY: Springer US.

Andronov, L., Han, M., Zhu, Y., Balaji, A., Roy, A.R., Barentine, A.E., Patel, P., Garhyan, J., Qi, L.S. and Moerner, W.E. (2024). Nanoscale cellular organization of viral RNA and proteins in SARS-CoV-2 replication organelles. *Nature Communications*, 15(1), p.4644.

Armer, H., Moffat, K., Wileman, T., Belsham, G.J., Jackson, T., Duprex, W.P., Ryan, M. and Monaghan, P. (2008). Foot-and-mouth disease virus, but not bovine enterovirus, targets the host cell cytoskeleton via the nonstructural protein 3Cpro. *Journal of Virology*, 82(21), pp.10556-10566.

Arnold, J., Mahamid, J., Lucic, V., De Marco, A., Fernandez, J.J., Laugks, T., Mayer, T., Hyman, A.A., Baumeister, W. and Plitzko, J.M. (2016). Site-specific cryo-focused ion beam sample preparation guided by 3D correlative microscopy. *Biophysical Journal*, 110(4), pp.860-869.

Bahar, M.W., Nasta, V., Fox, H., Sherry, L., Grehan, K., Porta, C., Macadam, A.J., Stonehouse, N.J., Rowlands, D.J., Fry, E.E. and Stuart, D.I. (2022). A

conserved glutathione binding site in poliovirus is a target for antivirals and vaccine stabilisation. *Communications Biology*, 5(1), p.1293.

Bahar, M.W., Porta, C., Fox, H., Macadam, A.J., Fry, E.E. and Stuart, D.I. (2021). Mammalian expression of virus-like particles as a proof of principle for next generation polio vaccines. *npj Vaccines*, 6(1), p.5.

Banjade, S. and Rosen, M.K. (2014). Phase transitions of multivalent proteins can promote clustering of membrane receptors. *elife*, 3, p.e04123.

Beale, E.V., Waterman, D.G., Hecksel, C., Van Rooyen, J., Gilchrist, J.B., Parkhurst, J.M., De Haas, F., Buijsse, B., Evans, G. and Zhang, P. (2020). A workflow for protein structure determination from thin crystal lamella by micro-electron diffraction. *Frontiers in Molecular Biosciences*, 7, p.179.

Belov, G.A. and van Kuppeveld, F.J. (2012). (+) RNA viruses rewire cellular pathways to build replication organelles. *Current Opinion in Virology*, 2(6), pp.740-747.

Belsham, G.J., Brangwyn, J.K., Ryan, M.D., Abrams, C.C. and King, A.M. (1990). Intracellular expression and processing of foot-and-mouth disease virus capsid precursors using vaccinia virus vectors: influence of the L protease. *Virology*, 176(2), pp.524-530.

Bentham, M., Holmes, K., Forrest, S., Rowlands, D.J. and Stonehouse, N.J. (2012). Formation of higher-order foot-and-mouth disease virus 3Dpol complexes is dependent on elongation activity. *Journal of Virology*, 86(4), pp.2371-2374.

Berger, C., Dumoux, M., Glen, T., Yee, N.B.Y., Mitchels, J.M., Patáková, Z., Darrow, M.C., Naismith, J.H. and Grange, M. (2023). Plasma FIB milling for the determination of structures in situ. *Nature Communications*, 14(1), p.629.

Berger, C., Dumoux, M., Glen, T., Yee, N.B.Y., Mitchels, J.M., Patáková, Z., Darrow, M.C., Naismith, J.H. and Grange, M. (2023). Plasma FIB milling for the determination of structures in situ. *Nature Communications*, 14(1), p.629.

Berry, J., Weber, S.C., Vaidya, N., Haataja, M. and Brangwynne, C.P. (2015). RNA transcription modulates phase transition-driven nuclear body assembly. *Proceedings of the National Academy of Sciences*, 112(38), pp.E5237-E5245.

Berryman, S., Brooks, E., Burman, A., Hawes, P., Roberts, R., Netherton, C., Monaghan, P., Whelband, M., Cottam, E., Elazar, Z. and Jackson, T. (2012). Foot-and-mouth disease virus induces autophagosomes during cell entry via a class III phosphatidylinositol 3-kinase-independent pathway. *Journal of Virology*, 86(23), pp.12940-12953.

Berryman, S., Moffat, K., Harak, C., Lohmann, V. and Jackson, T. (2016). Foot-and-mouth disease virus replicates independently of phosphatidylinositol 4-phosphate and type III phosphatidylinositol 4-kinases. *Journal of General Virology*, 97(8), pp.1841-1852.

Bisson, C., Hecksel, C.W., Gilchrist, J.B. and Fleck, R.A. (2021). Preparing lamellae from vitreous biological samples using a dual-beam scanning electron microscope for cryo-electron tomography (No. 174). SLAC National Accelerator Lab., Menlo Park, CA (United States).

Boeynaems, S., Alberti, S., Fawzi, N.L., Mittag, T., Polymenidou, M., Rousseau, F., Schymkowitz, J., Shorter, J., Wolozin, B., Van Den Bosch, L. and Tompa, P. (2018). Protein phase separation: a new phase in cell biology. *Trends in Cell Biology*, 28(6), pp.420-435.

Bracha, D., Walls, M.T. and Brangwynne, C.P. (2019). Probing and engineering liquid-phase organelles. *Nature Biotechnology*, 37(12), pp.1435-1445.

Bracha, D., Walls, M.T., Wei, M.T., Zhu, L., Kurian, M., Avalos, J.L., Toettcher, J.E. and Brangwynne, C.P. (2018). Mapping local and global liquid phase behavior in living cells using photo-oligomerizable seeds. *Cell*, 175(6), pp.1467-1480.

Brangwynne, C.P., Eckmann, C.R., Courson, D.S., Rybarska, A., Hoege, C., Gharakhani, J., Jülicher, F. and Hyman, A.A. (2009). Germline P granules are liquid droplets that localize by controlled dissolution/condensation. *Science*, 324(5935), pp.1729-1732.

Buchholz UJ, Finke S, Conzelmann KK. (1999). Generation of bovine respiratory syncytial virus (BRSV) from cDNA: BRSV NS2 is not essential for virus replication in tissue culture, and the human RSV leader region acts as a functional BRSV genome promoter. *Journal of Virology*, 73:251-259

Burt, A., Gaifas, L., Dendooven, T. and Gutsche, I. (2021). A flexible framework for multi-particle refinement in cryo-electron tomography. *PLoS Biology*, 19(8), p.e3001319.

Burt, A., Toader, B., Warshamanage, R., von Kügelgen, A., Pyle, E., Zivanov, J., Kimanius, D., Bharat, T.A. and Scheres, S.H. (2024). An image processing pipeline for electron cryo-tomography in RELION-5. *FEBS Open Bio*, 14(11), pp.1788-1804.

Byrne, D., Power, V., Bergin, A., Panaro, A., Cardwell, K., Teljeur, C., Walsh, K.A., Harrington, P. and Ryan, M. (2024). Rapid health technology assessment to

inform policy: a case study with respiratory syncytial virus. *European Journal of Public Health*, 34.

Carlomagno, Y., Chung, D.E.C., Yue, M., Castanedes-Casey, M., Madden, B.J., Dunmore, J., Tong, J., DeTure, M., Dickson, D.W., Petrucelli, L. and Cook, C. (2017). An acetylation-phosphorylation switch that regulates tau aggregation propensity and function. *Journal of Biological Chemistry*, 292(37), pp.15277-15286.

Chitray, M., Kotecha, A., Nsamba, P., Ren, J., Maree, S., Ramulongo, T., Paul, G., Theron, J., Fry, E.E., Stuart, D.I. and Maree, F.F. (2020). Symmetrical arrangement of positively charged residues around the 5-fold axes of SAT type foot-and-mouth disease virus enhances cell culture of field viruses. *PLoS Pathogens*, 16(9), p.e1008828.

Clarke, J.D., Duyvesteyn, H.M., Perez-Martin, E., Latišenko, U., Porta, C., Humphreys, K.V., Hay, A.L., Ren, J., Fry, E.E., van den Born, E. and Charleston, B. (2024). A broadly reactive ultralong bovine antibody that can determine the integrity of foot-and-mouth disease virus capsids. *Journal of General Virology*, 105(10), p.002032.

Curry, S., Fry, E., Blakemore, W., Abu-Ghazaleh, R., Jackson, T., King, A., Lea, S., Newman, J. and Stuart, D. (1997). Dissecting the roles of VP0 cleavage and RNA packaging in picornavirus capsid stabilization: the structure of empty capsids of foot-and-mouth disease virus. *Journal of Virology*, 71(12), pp.9743-9752.

Dahmane, S., Doucet, C., Le Gall, A., Chamontin, C., Dosset, P., Murcy, F., Fernandez, L., Salas, D., Rubinstein, E., Mougel, M. and Nollmann, M. (2019). Nanoscale organization of tetraspanins during HIV-1 budding by correlative dSTORM/AFM. *Nanoscale*, 11(13), pp.6036-6044.

Dahmane, S., Kerviel, A., Morado, D.R., Shankar, K., Ahlman, B., Lazarou, M., Altan-Bonnet, N. and Carlson, L.A. (2022). Membrane-assisted assembly and selective secretory autophagy of enteroviruses. *Nature Communications*, 13(1), p.5986.

Diot, C., Richard, C.A., Risso-Ballester, J., Martin, D., Fix, J., Eléouët, J.F., Sizun, C., Rameix-Welti, M.A. and Galloux, M. (2023). Hardening of respiratory syncytial virus inclusion bodies by cyclopamine proceeds through perturbation of the interactions of the M2-1 protein with RNA and the P protein. *International Journal of Molecular Sciences*, 24(18), p.13862.

Dolnik, O., Gerresheim, G.K. and Biedenkopf, N. (2021). New perspectives on the biogenesis of viral inclusion bodies in negative-sense RNA virus infections. *Cells*, 10(6), p.1460.

Dorobantu, C.M., Albulescu, L., Harak, C., Feng, Q., van Kampen, M., Strating, J.R., Gorbalenya, A.E., Lohmann, V., van der Schaar, H.M. and van Kuppeveld, F.J., (2015). Modulation of the host lipid landscape to promote RNA virus replication: the picornavirus encephalomyocarditis virus converges on the pathway used by hepatitis C virus. *PLoS Pathogens*, 11(9), p.e1005185.

Doyle, N., Hawes, P.C., Simpson, J., Adams, L.H. and Maier, H.J. (2019). The porcine deltacoronavirus replication organelle comprises double-membrane vesicles and zippered endoplasmic reticulum with double-membrane spherules. *Viruses*, 11(11), p.1030.

Doyle, N., Neuman, B.W., Simpson, J., Hawes, P.C., Mantell, J., Verkade, P., Alrashedi, H. and Maier, H.J. (2018). Infectious bronchitis virus nonstructural protein 4 alone induces membrane pairing. *Viruses*, 10(9), p.477.

Doyle, N., Simpson, J., Hawes, P.C. and Maier, H.J. (2021). Coronavirus RNA synthesis takes place within membrane-bound sites. *Viruses*, 13(12), p.2540.

Düster, R., Kaltheuner, I.H., Schmitz, M. and Geyer, M. (2021). 1, 6-Hexanediol, commonly used to dissolve liquid-liquid phase separated condensates, directly impairs kinase and phosphatase activities. *Journal of Biological Chemistry*, 296.

Engel, L., Gaietta, G., Dow, L.P., Swif, M.F., Pardon, G., Volkmann, N., Weis, W.I., Hanein, D. and Pruitt, B.L. (2019). Extracellular matrix micropatterning technology for whole cell cryogenic electron microscopy studies. *Journal of Micromechanics and Microengineering*, 29(11), p.115018.

Engel, L., Vasquez, C.G., Montabana, E.A., Sow, B.M., Walkiewicz, M.P., Weis, W.I. and Dunn, A.R. (2021). Lattice micropatterning for cryo-electron tomography studies of cell-cell contacts. *Journal of Structural Biology*, 213(4), p.107791.

Esfahani, B.G., Randolph, P.S., Peng, R., Stroupe, E., Grant, T. and Stagg, S.M. (2024). SPOT-RASTR-a cryo-EM specimen preparation technique that overcomes problems with preferred orientation and the air/water interface. *Biophysical Journal*, 123(3), p.184a.

Falsey, A.R., Hennessey, P.A., Formica, M.A., Cox, C. and Walsh, E.E. (2005). Respiratory syncytial virus infection in elderly and high-risk adults. *New England Journal of Medicine*, 352(17), pp.1749-1759.

Ferrer-Orta, C., Ferrero, D.S. and Verdaguer, N. (2023). Dual role of the foot-and-mouth disease virus 3B1 protein in the replication complex: As protein primer and as an essential component to recruit 3Dpol to membranes. *PLoS Pathogens*, 19(5), p.e1011373.

Förster, F. and Briegel, A. (2024). *Cryo-electron Tomography: Structural Biology in Situ*. Springer International Publishing AG.

Fry, E.E., Lea, S.M., Jackson, T., Newman, J.W., Ellard, F.M., Blakemore, W.E., Abu-Ghazaleh, R., Samuel, A., King, A.M. and Stuart, D.I. (1999). The structure and function of a foot-and-mouth disease virus-oligosaccharide receptor complex. *EMBO Journal*.

Fry, E.E., Newman, J.W., Curry, S., Najjam, S., Jackson, T., Blakemore, W., Lea, S.M., Miller, L., Burman, A., King, A.M. and Stuart, D.I. (2005). Structure of Foot-and-mouth disease virus serotype A1061 alone and complexed with oligosaccharide receptor: receptor conservation in the face of antigenic variation. *Journal of General Virology*, 86(7), pp.1909-1920.

Fu, X., Ning, J., Zhong, Z., Ambrose, Z., Charles Watkins, S. and Zhang, P. (2019). AutoCLEM: an automated workflow for correlative live-cell fluorescence microscopy and cryo-electron tomography. *Scientific Reports*, 9(1), p.19207.

Galloux, M., Risso-Ballester, J., Richard, C.A., Fix, J., Rameix-Welti, M.A. and Eléouët, J.F. (2020). Minimal elements required for the formation of respiratory syncytial virus cytoplasmic inclusion bodies in vivo and in vitro. *American Society for Microbiology*, 11(5), pp.10-1128.

Ganser, L.R., Ge, Y. and Myong, S. (2022). Single-molecule fluorescence methods to study protein-RNA interactions underlying biomolecular condensates. In Phase-Separated Biomolecular Condensates: Methods and Protocols (pp. 149-160). New York, NY: Springer US.

García, J., García-Barreno, B., Vivo, A. and Melero, J.A. (1993). Cytoplasmic inclusions of respiratory syncytial virus-infected cells: formation of inclusion bodies in transfected cells that coexpress the nucleoprotein, the phosphoprotein, and the 22K protein. *Virology*, 195(1), pp.243-247.

Geiger, F., Acker, J., Papa, G., Wang, X., Arter, W.E., Saar, K.L., Erkamp, N.A., Qi, R., Bravo, J.P., Strauss, S. and Krainer, G. (2021). Liquid-liquid phase separation underpins the formation of replication factories in rotaviruses. *The EMBO Journal*, 40(21), p.e107711.

Ghosh, A., Kota, D. and Zhou, H.X. (2022). Determining thermodynamic and material properties of biomolecular condensates by confocal microscopy and optical tweezers. In Phase-Separated Biomolecular Condensates: Methods and Protocols (pp. 237-260). New York, NY: Springer US.

Ginell, G.M. and Holehouse, A.S. (2022). An introduction to the stickers-and-spacers framework as applied to biomolecular condensates. In Phase-Separated Biomolecular Condensates: Methods and Protocols (pp. 95-116). New York, NY: Springer US.

Groppelli, E., Tuthill, T.J. and Rowlands, D.J. (2010). Cell entry of the aphthovirus equine rhinitis A virus is dependent on endosome acidification. *Journal of Virology*, 84(12), pp.6235-6240.

Guo, H.C., Jin, Y., Han, S.C., Sun, S.Q., Wei, Y.Q., Liu, X.J., Feng, X., Liu, D.X. and Liu, X.T. (2015). Quantitative proteomic analysis of BHK-21 cells infected with foot-and-mouth disease virus serotype Asia 1. *PLoS One*, 10(7), p.e0132384.

Han, S., Mao, L., Liao, Y., Sun, S., Zhang, Z., Mo, Y., Liu, H., Zhi, X., Lin, S., Seo, H.S. and Guo, H. (2019). Sec62 Suppresses Foot-and-Mouth Disease Virus Proliferation by Promotion of IRE1α-RIG-I Antiviral Signaling. *The Journal of Immunology*, 203(2), pp.429-440.

Hanna IV, M.G., Block, S., Frankel, E.B., Hou, F., Johnson, A., Yuan, L., Knight, G., Moresco, J.J., Yates III, J.R., Ashton, R. and Schekman, R. (2017). TFG facilitates outer coat disassembly on COPII transport carriers to promote tethering and fusion with ER-Golgi intermediate compartments. *Proceedings of the National Academy of Sciences*, 114(37), pp.E7707-E7716.

Haynes, R.M., Myers, J., López, C.S., Evans, J., Davulcu, O. and Yoshioka, C. (2024). A strategic approach for efficient cryo-EM grid optimization using design of experiments. *Journal of Structural Biology*, p.108068.

Hinton, T.M., Li, F. and Crabb, B.S. (2000). Internal ribosomal entry site-mediated translation initiation in equine rhinitis A virus: similarities to and differences from that of foot-and-mouth disease virus. *Journal of Virology*, 74(24), pp.11708-11716.

Hirai, Y. and Horie, M. (2023). Nyamanini Virus Nucleoprotein and Phosphoprotein Organize Viral Inclusion Bodies That Associate with Host Biomolecular Condensates in the Nucleus. *International Journal of Molecular Sciences*, 24(7), p.6550.

Hoenen, T., Shabman, R.S., Groseth, A., Herwig, A., Weber, M., Schudt, G., Dolnik, O., Basler, C.F., Becker, S. and Feldmann, H. (2012). Inclusion bodies are a site of ebolavirus replication. *Journal of Virology*, 86(21), pp.11779-11788.

Hoenger, A. (2014). High-resolution cryo-electron microscopy on macromolecular complexes and cell organelles. *Protoplasma*, 251, pp.417-427.

Hofstadter, W.A., Tsopurashvili, E. and Cristea, I.M. (2024). Viral regulation of organelle membrane contact sites. *PLoS Biology*, 22(3), p.e3002529.

Houtman, J.C., Yamaguchi, H., Barda-Saad, M., Braiman, A., Bowden, B., Appella, E., Schuck, P. and Samelson, L.E. (2006). Oligomerization of signaling complexes by the multipoint binding of GRB2 to both LAT and SOS1. *Nature Structural & Molecular* Biology, 13(9), pp.798-805.

Hsu, N.Y., Ilnytska, O., Belov, G., Santiana, M., Chen, Y.H., Takvorian, P.M., Pau, C., van der Schaar, H., Kaushik-Basu, N., Balla, T. and Cameron, C.E. (2010). Viral reorganization of the secretory pathway generates distinct organelles for RNA replication. *Cell*, 141(5), pp.799-811.

Huang, W.Y., Yan, Q., Lin, W.C., Chung, J.K., Hansen, S.D., Christensen, S.M., Tu, H.L., Kuriyan, J. and Groves, J.T. (2016). Phosphotyrosine-mediated LAT assembly on membranes drives kinetic bifurcation in recruitment dynamics of the Ras activator SOS. *Proceedings of the National Academy of Sciences,* 113(29), pp.8218-8223.

ICTV. (2021). Virus Taxonomy: *The ICTV Report on Virus Classification and Taxon Nomenclature*. [Online]. Available at: https://ictv.global/report

Jain, S., Wheeler, J.R., Walters, R.W., Agrawal, A., Barsic, A. and Parker, R. (2016). ATPase-modulated stress granules contain a diverse proteome and substructure. *Cell*, 164(3), pp.487-498.

Jain, S., Wheeler, J.R., Walters, R.W., Agrawal, A., Barsic, A. and Parker, R. (2016). ATPase-modulated stress granules contain a diverse proteome and substructure. *Cell*, 164(3), pp.487-498.

Jha, A., Jarvis, H., Fraser, C. and Openshaw, P. (2016). Respiratory syncytial virus. *SARS, MERS and other viral lung infections* (ch. 5). Sheffield: European Respiratory Society.

Jobe, F., Kelly, J.T., Simpson, J., Wells, J., Armstrong, S.D., Spick, M., Lacey, E., Logan, L., Geifman, N., Hawes, P. and Bailey, D. (2024). Viral PIC-pocketing: RSV sequestration of translational preinitiation complexes into bi-phasic biomolecular condensates. Journal of Virology, 98(3), pp.e00153-24.

Jobe, F., Simpson, J., Hawes, P., Guzman, E. and Bailey, D. (2020). Respiratory syncytial virus sequesters NF-κB subunit p65 to cytoplasmic inclusion bodies to inhibit innate immune signaling. Journal of Virology, 94(22), pp.10-1128.

Jun, S., Ro, H.J., Bharda, A., Kim, S.I., Jeoung, D. and Jung, H.S. (2019). Advances in cryo-correlative light and electron microscopy: applications for studying molecular and cellular events. *The Protein Journal*, 38, pp.609-615.

Karger, A., Schmidt, U. and Buchholz, U.J. (2001). Recombinant bovine respiratory syncytial virus with deletions of the G or SH genes: G and F proteins bind heparin. *Journal of General Virology*, 82(3), pp.631-640.

Kelley, K., Raczkowski, A.M., Klykov, O., Jaroenlak, P., Bobe, D., Kopylov, M., Eng, E.T., Bhabha, G., Potter, C.S., Carragher, B. and Noble, A.J. (2022). Waffle Method: A general and flexible approach for improving throughput in FIB-milling. *Nature Communications*, 13(1), p.1857.

Kelly, J.T., Dellosa, G.K., Newman, J., Hills, R., Mohamed, A.A., Aniscenko, J., Johnston, S.L. and Tuthill, T.J. (2024). Induction of neutralising antibodies against conserved rhinovirus capsid protein VP4 depends on presenting VP4 in a virus-like conformation. *bioRxiv*, pp.2024-06.

Kelly, J.T., Swanson, J., Newman, J., Groppelli, E., Stonehouse, N.J. and Tuthill, T.J. (2022). Membrane interactions and uncoating of aichi virus, a picornavirus that lacks a VP4. *Journal of Virology*, 96(7), pp.e00082-22.

Kieser, Q., Noyce, R.S., Shenouda, M., Lin, Y.C.J. and Evans, D.H. (2020). Cytoplasmic factories, virus assembly, and DNA replication kinetics collectively constrain the formation of poxvirus recombinants. *PLoS One*, 15(1), p.e0228028.

Klein, S., Wachsmuth-Melm, M., Winter, S.L., Kolovou, A. and Chlanda, P. (2021). Cryo-correlative light and electron microscopy workflow for cryo-focused ion beam milled adherent cells. *Methods in Cell Biology*. Vol. 162, pp. 273-302.

Kopito, R.R. (2000). Aggresomes, inclusion bodies and protein aggregation. *Trends in Cell Biology*, 10(12), pp.524-530.

Lac, A., Le Lam, A. and Heit, B. (2022). Optimizing long-term live cell imaging. In Fluorescent Microscopy (pp. 57-73). New York, NY: Springer US.

Lai, P.Y.A. (2023). Using light and electron microscopy to understand the replication of aphthoviruses (Doctoral dissertation, University of Oxford).

Lawrence, P., Pacheco, J.M., Uddowla, S., Hollister, J., Kotecha, A., Fry, E. and Rieder, E. (2013). Foot-and-mouth disease virus (FMDV) with a stable FLAG epitope in the VP1 GH loop as a new tool for studying FMDV pathogenesis. *Virology*, 436(1), pp.150-161.

Ledesma, J.R., Papanicolas, I., Stoto, M.A., Chrysanthopoulou, S.A., Isaac, C.R., Lurie, M.N. and Nuzzo, J.B. (2024). Pandemic preparedness improves national-level SARS-CoV-2 infection and mortality data completeness: a cross-country ecologic analysis. *Population Health Metrics*, 22(1), p.12.

Lee, M., Vetter, J. and Eichwald, C. (2025). The Influence of the Cytoskeleton on the Development and Behavior of Viral Factories in Mammalian Orthoreovirus. *Virology*, p.110423.

Li, J., Han, L., Hao, Y., Yuan, Y., Wang, M., Xin, X., Wang, H., Yu, F., Zheng, C. and Shen, C. (2020). Comparative transcriptome analysis reveals different host cell responses to acute and persistent foot-and-mouth disease virus infection. *Virologica Sinica*, 35, pp.52-63.

Li, P., Banjade, S., Cheng, H.C., Kim, S., Chen, B., Guo, L., Llaguno, M., Hollingsworth, J.V., King, D.S., Banani, S.F. and Russo, P.S. (2012). Phase transitions in the assembly of multivalent signalling proteins. *Nature*, 483(7389), pp.336-340.

Li, Y., Gu, J., Liu, C. and Li, D. (2022). A High-Throughput Method to Profile Protein Liquid-Liquid Phase Separation. In Phase-Separated Biomolecular Condensates: Methods and Protocols (pp. 261-268). New York, NY: Springer US.

Liang, Y., Zhang, X., Wu, B., Wang, S., Kang, L., Deng, Y., Xie, L. and Li, Z. (2023). Actomyosin-driven motility and coalescence of phase-separated viral inclusion bodies are required for efficient replication of a plant rhabdovirus. *New Phytologist*, 240(5), pp.1990-2006.

Lifland, A.W., Jung, J., Alonas, E., Zurla, C., Crowe Jr, J.E. and Santangelo, P.J. (2012). Human respiratory syncytial virus nucleoprotein and inclusion bodies antagonize the innate immune response mediated by MDA5 and MAVS. *Journal of Virology*, 86(15), pp.8245-8258.

Linnik, O., Liesche, J., Tilsner, J. and Oparka, K.J. (2013). Unraveling the structure of viral replication complexes at super-resolution. *Frontiers in Plant Science*, 4, p.6.

Logan, D., Abu-Ghazaleh, R., Blakemore, W., Curry, S., Jackson, T., King, A., Lea, S., Lewis, R., Newman, J., Parry, N. and Rowlands, D. (1993). Structure of a major immunogenic site on foot-and-mouth disease virus. *Nature*, 362(6420), pp.566-568.

Lv, B., Yuan, Y., Yang, Z., Wang, X., Hu, J., Sun, Y., Du, H., Liu, X., Duan, H., Ding, R. and Pan, Z. (2024). Stearoyl coenzyme A desaturase 1 (SCD1) regulates foot-and-mouth disease virus replication by modulating host cell lipid metabolism and viral protein 2C-mediated replication complex formation. *Journal of Virology*, 98(10), pp.e00902-24.

Lyu, C.A., Shen, Y. and Zhang, P. (2024). Zooming in and out: Exploring RNA Viral Infections with Multiscale Microscopic Methods. *Viruses*, 16(9), p.1504.

Ma, X., Luo, Z., Song, R., Nian, X., Choudhury, S.M., Ru, Y., Yang, F., Zhang, Y., Zeng, Z., Cao, W. and Pei, J. (2023). The Foot-and-Mouth Disease Virus Lb Protease Cleaves Intracellular Transcription Factors STAT1 and STAT2 to Antagonize IFN-β-Induced Signalling. *The Journal of Immunology*, 210(3), pp.283-296.

Maier, H.J. and Britton, P. (2012). Involvement of autophagy in coronavirus replication. *Viruses*, 4(12), pp.3440-3451.

Maier, H.J., Hawes, P.C., Cottam, E.M., Mantell, J., Verkade, P., Monaghan, P., Wileman, T. and Britton, P. (2013). Infectious bronchitis virus generates spherules from zippered endoplasmic reticulum membranes. *American Society of Microbiology*, 4(5), pp.10-1128.

Maier, H.J., Neuman, B.W., Bickerton, E., Keep, S.M., Alrashedi, H., Hall, R. and Britton, P. (2016). Extensive coronavirus-induced membrane rearrangements are not a determinant of pathogenicity. *Scientific Reports*, 6(1), p.27126.

Malik, N., Kotecha, A., Gold, S., Asfor, A., Ren, J., Huiskonen, J.T., Tuthill, T.J., Fry, E.E. and Stuart, D.I. (2017). Structures of foot and mouth disease virus pentamers: Insight into capsid dissociation and unexpected pentamer reassociation. *PLoS Pathogens*, 13(9), p.e1006607.

Mann, J.R., Gleixner, A.M., Mauna, J.C., Gomes, E., DeChellis-Marks, M.R., Needham, P.G., Copley, K.E., Hurtle, B., Portz, B., Pyles, N.J. and Guo, L. (2019). RNA binding antagonizes neurotoxic phase transitions of TDP-43. *Neuron*, 102(2), pp.321-338.

Martínez, I. and Melero, J.A. (2000). Binding of human respiratory syncytial virus to cells: implication of sulfated cell surface proteoglycans. *Journal of General Virology*, 81(11), pp.2715-2722.

Mateju, D., Franzmann, T.M., Patel, A., Kopach, A., Boczek, E.E., Maharana, S., Lee, H.O., Carra, S., Hyman, A.A. and Alberti, S. (2017). An aberrant phase transition of stress granules triggered by misfolded protein and prevented by chaperone function. *The EMBO Journal*, 36(12), pp.1669-1687.

Mazarakos, K., Qin, S. and Zhou, H.X. (2022). Calculating binodals and interfacial tension of phase-separated condensates from molecular simulations with finite-size corrections. In Phase-Separated Biomolecular Condensates: Methods and Protocols (pp. 1-35). New York, NY: Springer US.

McMurry, J. (1986). *Fundamentals of Organic Chemistry*. 2nd ed. Belmont, CA: Brooks/Cole Publishing Company. pp.301.

Mendonça, L., Howe, A., Gilchrist, J.B., Sheng, Y., Sun, D., Knight, M.L., Zanetti-Domingues, L.C., Bateman, B., Krebs, A.S., Chen, L. and Radecke, J. (2021). Correlative multi-scale cryo-imaging unveils SARS-CoV-2 assembly and egress. *Nature Communications*, 12(1), p.4629.

Midgley, R., Moffat, K., Berryman, S., Hawes, P., Simpson, J., Fullen, D., Stephens, D.J., Burman, A. and Jackson, T. (2013). A role for endoplasmic reticulum exit sites in foot-and-mouth disease virus infection. *Journal of General Virology,* 94(12), pp.2636-2646.

Molliex, A., Temirov, J., Lee, J., Coughlin, M., Kanagaraj, A.P., Kim, H.J., Mittag, T. and Taylor, J.P. (2015). Phase separation by low complexity domains promotes stress granule assembly and drives pathological fibrillization. *Cell*, 163(1), pp.123-133.

Monaghan, P., Cook, H., Jackson, T., Ryan, M. and Wileman, T. (2004). The ultrastructure of the developing replication site in foot-and-mouth disease virus-infected BHK-38 cells. *Journal of General Virology*, 85(4), pp.933-946.

Müller-Reichert, T., Mancuso, J., Lich, B. and McDonald, K. (2010). Three-dimensional reconstruction methods for Caenorhabditis elegans ultrastructure. *Methods in Cell Biology,* Vol. 96, pp. 331-361.

Nagy, P.D., Strating, J.R. and van Kuppeveld, F.J. (2016). Building viral replication organelles: close encounters of the membrane types. *PLoS Pathogens*, 12(10), p.e1005912.

Nair, H., Nokes, D.J., Gessner, B.D., Dherani, M., Madhi, S.A., Singleton, R.J., O'Brien, K.L., Roca, A., Wright, P.F., Bruce, N. and Chandran, A. (2010). Global burden of acute lower respiratory infections due to respiratory syncytial virus in young children: a systematic review and meta-analysis. *The Lancet*, 375(9725), pp.1545-1555.

Najjar, F., Castillo, S.R., Moncman, C.L., Wu, C.Y., Isla, E., Velez Ortega, A.C., Frolenkov, G.I., Cifuentes-Munoz, N. and Dutch, R.E. (2023). Imaging analysis reveals budding of filamentous human metapneumovirus virions and direct transfer of inclusion bodies through intercellular extensions. *American Society for Microbiology*, 14(5), pp.e01589-23.

Nchoutmboube, J.A., Viktorova, E.G., Scott, A.J., Ford, L.A., Pei, Z., Watkins, P.A., Ernst, R.K. and Belov, G.A. (2013). Increased long chain acyl-Coa synthetase activity and fatty acid import is linked to membrane synthesis for development of picornavirus replication organelles. *PLoS Pathogens*, 9(6), p.e1003401.

Nikolic, J., Civas, A., Lama, Z., Lagaudrière-Gesbert, C. and Blondel, D. (2016). Rabies virus infection induces the formation of stress granules closely connected to the viral factories. *PLoS Pathogens*, 12(10), p.e1005942.

Nikolic, J., Le Bars, R., Lama, Z., Scrima, N., Lagaudrière-Gesbert, C., Gaudin, Y. and Blondel, D. (2017). Negri bodies are viral factories with properties of liquid organelles. *Nature Communications*, 8(1), p.58.

O'Donnell, V.K., Pacheco, J.M., Henry, T.M. and Mason, P.W. (2001). Subcellular distribution of the foot-and-mouth disease virus 3A protein in cells infected with viruses encoding wild-type and bovine-attenuated forms of 3A. *Virology*, 287(1), pp.151-162.

Oikonomou, C.M. and Jensen, G.J. (2017). The development of cryo-EM and how it has advanced microbiology. *Nature Microbiology*, 2(12), pp.1577-1579.

Panjwani, A., Strauss, M., Gold, S., Wenham, H., Jackson, T., Chou, J.J., Rowlands, D.J., Stonehouse, N.J., Hogle, J.M. and Tuthill, T.J. (2014). Capsid protein VP4 of human rhinovirus induces membrane permeability by the formation of a size-selective multimeric pore. *PLoS Pathogens*, 10(8), p.e1004294.

Patel, A., Malinovska, L., Saha, S., Wang, J., Alberti, S., Krishnan, Y. and Hyman, A.A. (2017). ATP as a biological hydrotrope. *Science*, 356(6339), pp.753-756.

Paton, D.J., Sumption, K.J. and Charleston, B. (2009). Options for control of foot-and-mouth disease: knowledge, capability and policy. *Philosophical Transactions of the Royal Society B: Biological Sciences*, 364(1530), pp.2657-2667.

Pelletier, J. and Sonenberg, N. (1988). Internal initiation of translation of eukaryotic mRNA directed by a sequence derived from poliovirus RNA. *Nature*, 334(6180), pp.320-325.

Pierce, D.M., Hayward, C., Rowlands, D.J., Stonehouse, N.J. and Herod, M.R. (2023). Insights into polyprotein processing and RNA-protein interactions in foot-and-mouth disease virus genome replication. *Journal of Virology*, 97(5), pp.e00171-23.

Pierce, D.M., Hayward, C., Rowlands, D.J., Stonehouse, N.J. and Herod, M.R. (2023). Insights into polyprotein processing and RNA-protein interactions in foot-and-mouth disease virus genome replication. *Journal of Virology*, 97(5), pp.e00171-23.

Pilbeam, C., Edwards, G., Tonkin-Crine, S., Raymond, M., Van Hecke, O. and Gobat, N. (2022). Primary care preparedness for the SARS-CoV-2 pandemic: a survey of NHS GPs. *Family Practice*, 39(3), pp.332-339.

Quan, M.D., Liao, S.C.J., Ferreon, J.C. and Ferreon, A.C.M. (2022). Fluorescence lifetime imaging microscopy of biomolecular condensates. In Phase-Separated Biomolecular Condensates: Methods and Protocols (pp. 135-148). New York, NY: Springer US.

Rai, A.K., Chen, J.X., Selbach, M. and Pelkmans, L. (2018). Kinase-controlled phase transition of membraneless organelles in mitosis. *Nature*, 559(7713), pp.211-216.

Rhee, H.W., Zou, P., Udeshi, N.D., Martell, J.D., Mootha, V.K., Carr, S.A. and Ting, A.Y. (2013). Proteomic mapping of mitochondria in living cells via spatially restricted enzymatic tagging. *Science*, 339(6125), pp.1328-1331.

Ricciardi, S., Guarino, A.M., Giaquinto, L., Polishchuk, E.V., Santoro, M., Di Tullio, G., Wilson, C., Panariello, F., Soares, V.C., Dias, S.S. and Santos, J.C. (2022). The role of NSP6 in the biogenesis of the SARS-CoV-2 replication organelle. *Nature*, 606(7915), pp.761-768.

Rincheval, V., Lelek, M., Gault, E., Bouillier, C., Sitterlin, D., Blouquit-Laye, S., Galloux, M., Zimmer, C., Eleouet, J.F. and Rameix-Welti, M.A. (2017). Functional organization of cytoplasmic inclusion bodies in cells infected by respiratory syncytial virus. Nature Communications, 8(1), p.563.

Risso-Ballester, J., Galloux, M., Cao, J., Le Goffic, R., Hontonnou, F., Jobart-Malfait, A., Desquesnes, A., Sake, S.M., Haid, S., Du, M. and Zhang, X. (2021). A

condensate-hardening drug blocks RSV replication in vivo. *Nature*, 595(7868), pp.596-599.

Rossi, T.M., Moore, A., O'Sullivan, T.L. and Greer, A.L. (2019). Equine rhinitis a virus infection at a standardbred training facility: incidence, clinical signs, and risk factors for clinical disease. *Frontiers in Veterinary Science*, 6, p.71.

Rothan, H.A. and Kumar, M. (2019). Role of endoplasmic reticulum-associated proteins in flavivirus replication and assembly complexes. *Pathogens*, 8(3), p.148.

Roux, K.J., Kim, D.I., Raida, M. and Burke, B. (2012). A promiscuous biotin ligase fusion protein identifies proximal and interacting proteins in mammalian cells. *Journal of Cell Biology*, 196(6), pp.801-810.

Sachse, M., de Castro, I.F., Tenorio, R. and Risco, C. (2019). The viral replication organelles within cells studied by electron microscopy. *In Advances in Virus Research* (Vol. 105, pp. 1-33).

Santangelo, P.J., Lifland, A.W., Curt, P., Sasaki, Y., Bassell, G.J., Lindquist, M.E. and Crowe Jr, J.E. (2009). Single molecule-sensitive probes for imaging RNA in live cells. *Nature Methods*, 6(5), pp.347-349.

Sanz-Parra, A., Jimenez-Clavero, M.A., Garcıa-Briones, M.M., Blanco, E., Sobrino, F. and Ley, V. (1999). Recombinant viruses expressing the foot-and-mouth disease virus capsid precursor polypeptide (P1) induce cellular but not humoral antiviral immunity and partial protection in pigs. *Virology*, 259(1), pp.129-134.

Sarkar, S., Biligiri, K.K., Vats, N., Rampalli, S., Ganguly, S., Kumar, N., Sarkar, D.P., Ganguly, N.K. and Sharma, N.R. (2025). Participation of host cell proteins in inclusion bodies of non-segmented RNA virus infected cells: a molecular insight. *Virology Journal*, 22(1), p.282.

Schaffer, M., Engel, B.D., Laugks, T., Mahamid, J., Plitzko, J.M. and Baumeister, W. (2015). Cryo-focused ion beam sample preparation for imaging vitreous cells by cryo-electron tomography. *Bio-Protocol*, 5(17), pp.e1575-e1575.

Schiøtz, O.H., Kaiser, C.J., Klumpe, S., Morado, D.R., Poege, M., Schneider, J., Beck, F., Klebl, D.P., Thompson, C. and Plitzko, J.M. (2024). Serial Lift-Out: sampling the molecular anatomy of whole organisms. *Nature Methods*, 21(9), pp.1684-1692.

Schlender J, Bossert B, Buchholz U, Conzelmann KK. (2000). Bovine respiratory syncytial virus nonstructural proteins NS1 and NS2 cooperatively antagonize

alpha/beta interferon-induced antiviral response. *Journal of Virology*, 74: 8234-8242.

Shah, P.N., Gilchrist, J.B., Forsberg, B.O., Burt, A., Howe, A., Mosalaganti, S., Wan, W., Radecke, J., Chaban, Y., Sutton, G. and Stuart, D.I. (2023). Characterization of the rotavirus assembly pathway in situ using cryoelectron tomography. *Cell Host & Microbe*, 31(4), pp.604-615.

Shah, P.N.M., Sanchez-Garcia, R. and Stuart, D.I. (2025). TomoCPT: A centroid prediction tool for particle localisation in cryo-electron tomograms. *Acta Crystallographica Section D: Structural Biology*. (81), pp.63-76.

Shah, P.N., Stanifer, M.L., Höhn, K., Engel, U., Haselmann, U., Bartenschlager, R., Kräusslich, H.G., Krijnse-Locker, J. and Boulant, S. (2017). Genome packaging of reovirus is mediated by the scaffolding property of the microtubule network. *Cellular Microbiology*, 19(12), p.e12765.

Shakeel, S., Westerhuis, B.M., Domanska, A., Koning, R.I., Matadeen, R., Koster, A.J., Bakker, A.Q., Beaumont, T., Wolthers, K.C. and Butcher, S.J. (2016). Multiple capsid-stabilizing interactions revealed in a high-resolution structure of an emerging picornavirus causing neonatal sepsis. *Nature Communications*, 7(1), p.11387.

Sheng, Y., Morris, K., Radecke, J. and Zhang, P. (2022). Cryo-electron tomography remote data collection and subtomogram averaging. *Journal of Visualized Experiments*, (185).

Sherry, L., Bahar, M.W., Porta, C., Fox, H., Grehan, K., Nasta, V., Duyvesteyn, H.M., de Colibus, L., Marsian, J., Murdoch, I. and Ponndorf, D. (2024). Risk-free polio vaccine: Recombinant expression systems for production of stabilised virus-like particles. *bioRxiv*, pp.2024-05.

Shi, T., Denouel, A., Tietjen, A.K., Campbell, I., Moran, E., Li, X., Campbell, H., Demont, C., Nyawanda, B.O., Chu, H.Y. and Stoszek, S.K. (2020). Global disease burden estimates of respiratory syncytial virus-associated acute respiratory infection in older adults in 2015: a systematic review and meta-analysis. *The Journal of Infectious Diseases*, 222(Supplement 7), pp.S577-S583.

Shi, T., McAllister, D.A., O'Brien, K.L., Simoes, E.A., Madhi, S.A., Gessner, B.D., Polack, F.P., Balsells, E., Acacio, S., Aguayo, C. and Alassani, I. (2017). Global, regional, and national disease burden estimates of acute lower respiratory infections due to respiratory syncytial virus in young children in 2015: a systematic review and modelling study. *The Lancet*, 390(10098), pp.946-958.

Shimmon, G., Kotecha, A., Ren, J., Asfor, A.S., Newman, J., Berryman, S., Cottam, E.M., Gold, S., Tuthill, T.J., King, D.P. and Brocchi, E. (2018). Generation and characterisation of recombinant FMDV antibodies: Applications for advancing diagnostic and laboratory assays. *Plos One*, 13(8), p.e0201853.

Shimmon, G., Wood, B.A., Morris, A., Mioulet, V., Grazioli, S., Brocchi, E., Berryman, S., Tuthill, T., King, D.P., Burman, A. and Jackson, T. (2016). Truncated bovine integrin alpha-v/beta-6 as a universal capture ligand for fmd diagnosis. *PloS One*, 11(8), p.e0160696.

Shin, Y. and Brangwynne, C.P. (2017). Liquid phase condensation in cell physiology and disease. *Science*, 357(6357), p.eaaf4382.

Shin, Y., Chang, Y.C., Lee, D.S., Berry, J., Sanders, D.W., Ronceray, P., Wingreen, N.S., Haataja, M. and Brangwynne, C.P. (2018). Liquid nuclear condensates mechanically sense and restructure the genome. *Cell*, 175(6), pp.1481-1491.

Sibert, B.S., Kim, J.Y., Yang, J.E. and Wright, E.R. (2021). Micropatterning transmission electron microscopy grids to direct cell positioning within whole-cell cryo-electron tomography workflows. *Journal of Visualized Experiments*, (175), pp.10-3791.

Snead, W.T. and Gladfelter, A.S. (2019). The control centers of biomolecular phase separation: how membrane surfaces, PTMs, and active processes regulate condensation. *Molecular Cell*, 76(2), pp.295-305.

Snijder, E.J., Limpens, R.W., de Wilde, A.H., de Jong, A.W., Zevenhoven-Dobbe, J.C., Maier, H.J., Faas, F.F., Koster, A.J. and Bárcena, M. (2020). A unifying structural and functional model of the coronavirus replication organelle: Tracking down RNA synthesis. *PLoS Biology*, 18(6), p.e3000715.

Spink, M.C., Darrow, M.C., Fisher, H., Burt, A., Marshall, K., Luengo, I., Harkiolaki, M. and Duke, L. (2018). Correlation of cryo soft X-ray tomography with cryo fluorescence microscopy to characterise cellular organelles at beamline B24, Diamond Light Source. Microscopy and Microanalysis, 24(S2), pp.374-375.

Stancheva, V.G. and Sanyal, S. (2024). Positive-strand RNA virus replication organelles at a glance. *Journal of Cell Science*, 137(17).

Stasiak, K., Dunowska, M. and Rola, J. (2024). Prevalence and sequence analysis of equine rhinitis viruses among horses in Poland. *Viruses*, 16(8), p.1204.

Stockley, P.G., Twarock, R., Bakker, S.E., Barker, A.M., Borodavka, A., Dykeman, E., Ford, R.J., Pearson, A.R., Phillips, S.E., Ranson, N.A. and Tuma, R. (2013). Packaging signals in single-stranded RNA viruses: nature's alternative to a

purely electrostatic assembly mechanism. *Journal of Biological Physics*, 39(2), pp.277-287.

Strale, P.O., Azioune, A., Bugnicourt, G., Lecomte, Y., Chahid, M. and Studer, V., (2016). Multiprotein printing by light-induced molecular adsorption. *Advanced Materials*, 28(10), pp.2024-2029.

Sun, G., Cui, Q., Garcia Jr, G., Wang, C., Zhang, M., Arumugaswami, V., Riggs, A.D. and Shi, Y. (2021). Comparative transcriptomic analysis of SARS-CoV-2 infected cell model systems reveals differential innate immune responses. *Scientific Reports*, 11(1), p.17146.

Sun, P., Zhang, S., Qin, X., Chang, X., Cui, X., Li, H., Zhang, S., Gao, H., Wang, P., Zhang, Z. and Luo, J. (2018). Foot-and-mouth disease virus capsid protein VP2 activates the cellular EIF2S1-ATF4 pathway and induces autophagy via HSPB1. *Autophagy*, 14(2), pp.336-346.

Sutton, G., Sun, D., Fu, X., Kotecha, A., Hecksel, C.W., Clare, D.K., Zhang, P., Stuart, D.I. and Boyce, M. (2020). Assembly intermediates of orthoreovirus captured in the cell. *Nature Communications*, 11(1), p.4445.

Talic, S., Shah, S., Wild, H., Gasevic, D., Maharaj, A., Ademi, Z., Li, X., Xu, W., Mesa-Eguiagaray, I., Rostron, J. and Theodoratou, E. (2021). Effectiveness of public health measures in reducing the incidence of covid-19, SARS-CoV-2 transmission, and covid-19 mortality: systematic review and meta-analysis. *BMJ*, 375.

Tegunov, D. and Cramer, P. (2019). Real-time cryo-electron microscopy data preprocessing with Warp. *Nature Methods*, 16(11), pp.1146-1152.

Tegunov, D., Xue, L., Dienemann, C., Cramer, P. and Mahamid, J. (2021). Multi-particle cryo-EM refinement with M visualizes ribosome-antibiotic complex at 3.5 Å in cells. *Nature Methods*, 18(2), pp.186-193.

ThermoScientific. (2021) Instrumentation and Resources for the Preparation of Cryo-EM Samples. (online). Available at: https://assets.thermofisher.com/TFS-Assets/MSD/Datasheets/instruments-resources-cryo-em-sample-prep-ds0367.pdf

ThermoScientific. (2023) Talos Arctica & Glacios Training Documentation Packet. (online). Available at: https://sites.bu.edu/cryoem/files/2024/09/ThermoFisher_Talos_Arctica__Glacios_Training_Packet.pdf

ThermoScientific. (2024a) Krios, Talos Arctica, Glacios and Tundra Cryo-TEMs. (online). Available at: https://assets.thermofisher.com/TFS-Assets/MSD/Datasheets/krios-talos-arctica-glacios-tundra-crip-tems-ds0096-en.pdf

ThermoScientific. (2024b) Glacios 2 Cryo-TEM with Smart EPU Software, E-CFEG, and Falcon 4i Direct Electron Detector. (online). Available at: https://assets.thermofisher.com/TFS-Assets/MSD/Datasheets/glacios2-cryo-tem-smart-epu-falcon4i-direct-electron-ds0491.pdf

ThermoScientific. (2024c) Tomography 5 and Tomo Live Software User-friendly batch acquisition for and on-the-fly reconstruction for cryo-electron tomography. (online). Available at: https://assets.thermofisher.com/TFS-Assets/MSD/Datasheets/tomography-5-software-ds0362.pdf

Thomas, C.I., Urban, N.T., Sun, Y., Colgan, L.A., Tu, X., Yasuda, R. and Kamasawa, N. (2021). Cryo-Confocal Imaging for CLEM Mapping in Brain Tissues. *Microscopy Today*, 29(5), pp.34-39.

Tillu, V.A., Redpath, G.M., Rae, J., Ruan, J., Yao, Y., Cagigas, M.L., Whan, R., Hardeman, E.C., Gunning, P.W., Ananthanarayanan, V. and Parton, R.G. (2024). Precision in situ cryogenic correlative light and electron microscopy of optogenetically positioned organelles. *Journal of Cell Science*, 137(20).

Toro-Nahuelpan, M., Zagoriy, I., Senger, F., Blanchoin, L., Théry, M. and Mahamid, J. (2020). Tailoring cryo-electron microscopy grids by photo-micropatterning for in-cell structural studies. *Nature Methods*, 17(1), pp.50-54.

Tulloch, F., Pathania, U., Luke, G.A., Nicholson, J., Stonehouse, N.J., Rowlands, D.J., Jackson, T., Tuthill, T., Haas, J., Lamond, A.I. and Ryan, M.D. (2014). FMDV replicons encoding green fluorescent protein are replication competent. *Journal of Virological Methods*, 209, pp.35-40.

Turoňová, B., Sikora, M., Schürmann, C., Hagen, W.J., Welsch, S., Blanc, F.E., von Bülow, S., Gecht, M., Bagola, K., Hörner, C. and van Zandbergen, G. (2020). In situ structural analysis of SARS-CoV-2 spike reveals flexibility mediated by three hinges. *Science*, 370(6513), pp.203-208.

Tuthill, T.J., Bubeck, D., Rowlands, D.J. and Hogle, J.M. (2006). Characterisation of early steps in the poliovirus infection process: receptor-decorated liposomes induce conversion of the virus to membrane-anchored entry-intermediate particles. *Journal of Virology*, 80(1), pp.172-180.

Tuthill, T.J., Groppelli, E., Hogle, J.M. and Rowlands, D.J. (2010). *Picornaviruses*. Cell Entry by Non-Enveloped Viruses. Springer. pp.43-89.

Tuthill, T.J., Harlos, K., Walter, T.S., Knowles, N.J., Groppelli, E., Rowlands, D.J., Stuart, D.I. and Fry, E.E. (2009). Equine rhinitis A virus and its low pH empty particle: clues towards an aphthovirus entry mechanism?. *PLoS Pathogens*, 5(10), p.e1000620.

UKBRCN. (2025) The Specified Animal Pathogens Order 2008 (SAPO). (online). Available at: https://www.ukbrcn.org/guidelines/the-specified-animal-pathogens-order-2008/

Vacek, E., Schmidt, O., Chen, S., Jin, Q. and Jacobsen, C. (2018). Correlative cryo confocal light microscopy (C3LM) and x-ray fluorescence. *Microscopy and Microanalysis,* 24(S2), pp.150-151.

van Heel, M., Harauz, G., Orlova, E.V., Schmidt, R. and Schatz, M. (1996). A new generation of the IMAGIC image processing system. *Journal of Structural Biology*, 116(1), pp.17-24.

Vetter, J., Lee, M. and Eichwald, C. (2024). The Role of the Host Cytoskeleton in the Formation and Dynamics of Rotavirus Viroplasms. *Viruses*, 16(5), p.668.

Vijayakrishnan, S. (2023). In Situ Imaging of Virus-Infected Cells by Cryo-Electron Tomography: An Overview. *Virus Infected Cells*, pp.3-36.

Wang, H., Xin, X., Zheng, C. and Shen, C. (2020). Single-cell analysis of foot-and-mouth disease virus. *Frontiers in Microbiology*, 11, p.361.

Wang, S., Dai, T., Qin, Z., Pan, T., Chu, F., Lou, L., Zhang, L., Yang, B., Huang, H., Lu, H. and Zhou, F. (2021). Targeting liquid-liquid phase separation of SARS-CoV-2 nucleocapsid protein promotes innate antiviral immunity by elevating MAVS activity. *Nature Cell Biology*, 23(7), pp.718-732.

Wang, Y., Duan, Y., Han, C., Yao, S., Qi, X., Gao, Y., Maier, H.J., Britton, P., Chen, L., Zhang, L. and Gao, L. (2017). Infectious bursal disease virus subverts autophagic vacuoles to promote viral maturation and release. *Journal of Virology*, 91(5), pp.10-1128.

Werid, G.M., Wubshet, A.K., Araya, T.T., Miller, D., Hemmatzadeh, F., Reichel, M.P. and Petrovski, K. (2024). Detection of Bovine Respiratory Syncytial Virus in Cattle: A Systematic Review and Meta-Analysis. *Ruminants*, 4(4), pp.491-514.

Wignall-Fleming, E.B., Carlos, T.S. and Randall, R.E. (2024). Liquid-liquid phase inclusion bodies in acute and persistent parainfluenaza virus type 5 infections. *Journal of General Virology*, 105(9), p.002021.

Wippich, F., Bodenmiller, B., Trajkovska, M.G., Wanka, S., Aebersold, R. and Pelkmans, L. (2013). Dual specificity kinase DYRK3 couples stress granule condensation/dissolution to mTORC1 signaling. *Cell*, 152(4), pp.791-805.

WHOA. (2025). Technical Disease Card: Foot and mouth disease. (online). Available at: https://www.woah.org/en/document/technical-disease-card-fmd/

World Health Organization. (2024). Guidelines on the quality, safety and efficacy of respiratory syncytial virus vaccines. [online]. Available at: https://www.who.int/docs/default-source/biologicals/ecbs/rsv-guidelines-post-ecbs.pdf

World Organization for Animal Health. (2021). *Foot-and-Mouth Disease Virus.* [Online]. Available at: https://www.woah.org/app/uploads/2021/09/foot-and-mouth-disease-1.pdf

Wu, J.E., Zhang, Z., Teng, Z., Abdullah, S.W., Sun, S. and Guo, H. (2021). Sec62 regulates endoplasmic reticulum stress and autophagy balance to affect foot-and-mouth disease virus replication. *Frontiers in Cellular and Infection Microbiology*, 11, p.707107.

Wu, X., Qi, X., Qu, B., Zhang, Z., Liang, M., Li, C., Cardona, C.J., Li, D. and Xing, Z. (2014). Evasion of antiviral immunity through sequestering of TBK1/IKKε/IRF3 into viral inclusion bodies. *Journal of Virology*, 88(6), pp.3067-3076.

Wu, Y., Zhang, Z., Li, Y. and Li, Y. (2022). The regulation of integrated stress response signaling pathway on viral infection and viral antagonism. *Frontiers in Microbiology*, 12, p.814635.

Xue, Q., Liu, H., Zeng, Q., Zheng, H., Xue, Q. and Cai, X. (2019). The DEAD-Box RNA helicase DDX1 interacts with the viral protein 3D and inhibits foot-and-mouth disease virus replication. *Virologica Sinica*, 34, pp.610-617.

Yang, J.E., Rossignol, E.D., Chang, D., Zaia, J., Forrester, I., Raja, K., Winbigler, H., Nicastro, D., Jackson, W.T. and Bullitt, E. (2020). Complexity and ultrastructure of infectious extracellular vesicles from cells infected by non-enveloped virus. *Scientific Reports*, 10(1), p.7939.

Yang, J.E., Sibert, B., Larson, M. and Wright, E.R. (2024). From Crystals to Cells: Freezing Challenging Biological Targets With The VitroJet. *Microscopy and Microanalysis*, 30(1).

Yang, P., Yuan, Y., Sun, Y., Lv, B., Du, H., Zhou, Z., Yang, Z., Liu, X., Duan, H. and Shen, C. (2023). The host protein CAD regulates the replication of FMDV through the function of pyrimidines' DE Novo synthesis. *Journal of Virology*, 97(5), pp.e00369-23.

Yang, W., Li, D., Ru, Y., Bai, J., Ren, J., Zhang, J., Li, L., Liu, X. and Zheng, H. (2020). Foot-and-mouth disease virus 3A protein causes upregulation of autophagy-related protein LRRC25 to inhibit the G3BP1-mediated RIG-like helicase-signaling pathway. *Journal of Virology*, 94(8), pp.10-1128.

Ye, X., Pan, T., Wang, D., Fang, L., Ma, J., Zhu, X., Shi, Y., Zhang, K., Zheng, H., Chen, H. and Li, K. (2018). Foot-and-mouth disease virus counteracts on internal ribosome entry site suppression by G3BP1 and inhibits G3BP1-mediated stress granule assembly via post-translational mechanisms. *Frontiers in Immunology*, 9, p.1142.

Zhang, C., Yang, F., Wojdyla, J.A., Qin, B., Zhang, W., Zheng, M., Cao, W., Wang, M., Gao, X., Zheng, H. and Cui, S. (2022). An anti-picornaviral strategy based on the crystal structure of foot-and-mouth disease virus 2C protein. *Cell Reports*, 40(1).

Zhang, Q., Ye, H., Liu, C., Zhou, H., He, M., Liang, X., Zhou, Y., Wang, K., Qin, Y., Li, Z. and Chen, M. (2024). PABP-driven secondary condensed phase within RSV inclusion bodies activates viral mRNAs for ribosomal recruitment. *Virologica Sinica*, 39(2), pp.235-250.

Zhang, X., Sridharan, S., Zagoriy, I., Oegema, C.E., Ching, C., Pflaesterer, T., Fung, H.K., Becher, I., Poser, I., Müller, C.W. and Hyman, A.A. (2023). Molecular mechanisms of stress-induced reactivation in mumps virus condensates. *Cell*, 186(9), pp.1877-1894.

Zheng, S., Wolff, G., Greenan, G., Chen, Z., Faas, F.G., Bárcena, M., Koster, A.J., Cheng, Y. and Agard, D.A. (2022). AreTomo: An integrated software package for automated marker-free, motion-corrected cryo-electron tomographic alignment and reconstruction. *Journal of Structural Biology*: 6, p.100068.

Zhou, Q. and Lok, S.M. (2024). Visualizing the virus world inside the cell by cryo-electron tomography. *Journal of Virology*, pp.e01085-23.

Zhou, Y., Sotcheff, S.L. and Routh, A.L. (2022). Next-generation sequencing: A new avenue to understand viral RNA-protein interactions. *Journal of Biological Chemistry*, 298(5), p.101924.

Zhou, Y., Su, J.M., Samuel, C.E. and Ma, D. (2019). Measles virus forms inclusion bodies with properties of liquid organelles. *Journal of Virology*, 93(21), pp.10-1128.